Hélio Emmendoerfer Junior

A LEVEL SET APPROACH FOR TOPOLOGY OPTIMIZATION WITH LOCAL STRESS CONSTRAINTS

UMA ABORDAGEM DE CURVAS DE NÍVEL PARA OTIMIZAÇÃO TOPOLÓGICA COM RESTRIÇÕES DE TENSÃO LOCAL

Tese submetida ao
Programa de Pós-Graduação em
Engenharia Mecânica da Universidade
Federal de Santa Catarina para a
obtenção do Grau de
Doutor em Engenharia Mecânica.

Orientador:
Prof. Eduardo Alberto Fancello, D. Sc.

Florianópolis

2015

Ficha de identificação da obra elaborada pelo autor,
através do Programa de Geração Automática da Biblioteca Universitária da UFSC.

Emmendoerfer Junior, Hélio
A level set approach for topology optimization with local stress constraints = Uma abordagem de curvas de nível para otimização topológica com restrições de tensão local / Hélio Emmendoerfer Junior ; orientador, Eduardo Alberto Fancello - Florianópolis, SC, 2015.
167 p.

Tese (doutorado) - Universidade Federal de Santa Catarina, Centro Tecnológico. Programa de Pós-Graduação em Engenharia Mecânica.

Inclui referências

1. Engenharia Mecânica. 2. Otimização topológica estrutural. 3. Restrição de tensão. 4. Curvas de nível. 5. Lagrangiano aumentado. I. Fancello, Eduardo Alberto. II. Universidade Federal de Santa Catarina. Programa de Pós Graduação em Engenharia Mecânica. III. Título.

Hélio Emmendoerfer Junior

UMA ABORDAGEM DE CURVAS DE NÍVEL PARA OTIMIZAÇÃO TOPOLÓGICA COM RESTRIÇÕES DE TENSÃO LOCAL

Esta Tese foi julgada adequada para obtenção do Título de Doutor em Engenharia Mecânica, Área de concentração Análise e Projeto Mecânico, e aprovada em sua forma final pelo Programa de Pós-Graduação em Engenharia Mecânica da Universidade Federal de Santa Catarina.

Florianópolis, 02 de dezembro de 2015.

Albertazzi

Prof. Armando Albertazzi Gonçalves Jr., Dr. Eng.
Coordenador do Curso

Banca Examinadora:

Prof. Eduardo Alberto Fancello, D. Sc.
Orientador
Universidade Federal de Santa Catarina

Prof. Emílio Carlos Nelli Silva, Ph.D.
Relator
Universidade de São Paulo

Prof. Renato Pavanello, Dr.
Universidade Estadual de Campinas

Prof. Eduardo Lenz Cardoso, Dr.
Universidade do Estado de Santa Catarina

p/ Prof. Otávio Augusto Alves da Silveira, Dr.
Universidade Federal de Santa Catarina

Prof. Clovis Sperb de Barcellos, Ph.D.
Universidade Federal de Santa Catarina

Este trabalho é dedicado
aos meus queridos pais.

AGRADECIMENTOS

Ao Prof. Eduardo Fancello, pela paciência ao transmitir os ensinamentos e dedicação dispensada na orientação deste trabalho, além de sua amizade.

Aos professores Emílio Carlos Nelli Silva, Renato Pavanello, Eduardo Lenz Cardoso, Clovis Sperb de Barcellos e Otávio Augusto Alves da Silveira por aceitarem compor a banca examinadora e por suas valiosas contribuições na revisão do texto.

Ao Programa de Pós-graduação em Engenharia Mecânica (PosMec) e ao laboratório GRANTE pela infraestrutura disponível. Sem citar nomes, gostaria de agradecer a todos os colegas do laboratório pela amizade e conhecimentos compartilhados.

Ao Prof. Glaucio Paulino, pela oportunidade de realizar o intercâmbio durante um ano (outubro/2014 até setembro/2015) na *University of Illinois at Urbana-Champaign*, nos Estados Unidos, através do Programa de Doutorado Sanduíche no Exterior - PDSE/CAPES.

Ao CNPq pelo apoio financeiro concedido por meio de concessão de bolsa de estudo. À CAPES pelos auxílios financeiros que permitiram realizar o doutorado sanduíche.

Finalmente, agradeço aos meus pais Hélio e Mafalda, pelos incentivos durante toda a minha vida. À Andressa, pelo apoio e compreensão que foram indispensáveis para a conclusão desta etapa da vida. Enfim, a toda minha família pelo carinho.

RESUMO

Este trabalho tem como foco o problema de otimização topológica para minimização de massa com restrições locais sobre o campo de tensões de von Mises. Usando conceitos de curvas de nível (ou *level sets*) para o controle do domínio, desenvolve-se um procedimento de restrição responsável por uma contínua ativação/desativação de um número finito de restrições de tensão local durante a sequência de otimização. As restrições são convenientemente distribuídas sobre o domínio e impostas ao problema através de uma abordagem Lagrangiano aumentado. O principal objetivo da presente tese é criar um algoritmo capaz de identificar as regiões com concentração de tensões e conduzir a topologia para um mínimo local viável. A evolução das curvas de nível utiliza informações da análise de sensibilidade para atualizar a topologia da estrutura. Em um primeiro momento, tendo como finalidade testar a restrição de tensão proposta, emprega-se a clássica equação de Hamilton-Jacobi para a atualização das curvas de nível, uma técnica bastante usada na literatura. Em seguida, uma equação de reação-difusão é usada para orientar, também via evolução das curvas de nível, a sequência de otimização do projeto. Esta última equação de evolução possui duas vantagens. A primeira é a possibilidade de nuclear furos durante o processo de otimização, uma importante característica para um verdadeiro método de otimização topológica. A outra vantagem consiste na eliminação da etapa de reinicialização da função, necessária em evoluções de Hamilton-Jacobi, obtendo melhorias significantes em termos de convergência. Para a solução numérica da equação de reação-difusão, utilizam-se malhas regulares com os tradicionais elementos finitos quadrilaterais e malhas poligonais não-estruturadas, obtidas a partir de tesselações de Voronoi. Vários exemplos em duas dimensões com resultados numéricos bem sucedidos comprovam o bom comportamento da metodologia proposta para detectar concentrações de tensões e propor um projeto viável.

Palavras-chave: otimização topológica, curvas de nível, restrição de tensão local, Lagrangiano aumentado, equação de reação-difusão, elementos finitos poligonais.

RESUMO EXPANDIDO

INTRODUÇÃO

Os últimos 20 anos caracterizam-se por uma notável popularização das ferramentas de simulação numérica, incluindo análise multifísica, projeto de produtos e integração de ferramentas como pacotes de otimização. Na área de projeto mecânico e estrutural, muitas áreas de aplicação da engenharia como civil, naval, aeroespacial, automotiva, bioengenharia e outras, vêm lucrando com os grandes benefícios oferecidos pelo uso dessas ferramentas disponíveis em códigos comerciais. Os clássicos algoritmos de programação matemática, ou, mais recentemente, os algoritmos baseados em heurísticas, são empregados como uma alternativa para encontrar minimizadores locais e globais em problemas de otimização.

Devido às convenientes propriedades matemáticas, a minimização da energia de deformação (*compliance*) vem sendo o problema mais utilizado em otimização topológica estrutural, e está disponível atualmente em códigos comerciais de elementos finitos como uma ferramenta numérica. No entanto, um problema aparentemente mais simples, aquele que visa obter um projeto mais leve e que satisfaça critérios de falha mecânica, ainda não está implementado nestes códigos. Este fato deve-se às dificuldades matemáticas e numéricas envolvidas no problema, constituindo um assunto classificado como fronteira do conhecimento na aplicação dos métodos de otimização. O problema tem atraído a atenção de pesquisadores nos últimos 10 anos devido à sua grande aplicação na indústria, mas poucos trabalhos obtiveram resultados conclusivos.

OBJETIVOS

Este trabalho tem como propósito contribuir na consolidação de estratégias eficientes para tratar problemas considerando a falha do material. Em particular, deseja-se propor uma abordagem para resolver o problema de otimização topológica para minimizar a massa de uma estrutura com restrições sobre as tensões locais. As seguintes observações motivam esta proposição: a) os bons resultados obtidos em [1] usando uma abordagem Lagrangiano aumentado para o tratamento das restrições de tensão; e b) a possibilidade de atenuar a dificuldade matemática/numérica conhecida como *singularidade de tensões*, quando o domínio é representado implicitamente por uma função de curvas de nível, o que permite uma nítida separação entre regiões com e sem material no domínio. Dentro deste contexto, o principal

objetivo desta tese é criar um algoritmo de otimização topológica capaz de identificar regiões com concentração de tensão (indesejáveis na concepção de projetos) e conduzir a topologia para um mínimo local viável.

METODOLOGIA

Para o controle geométrico do domínio, utiliza-se uma abordagem de curvas de nível que consiste em representar o domínio implicitamente através de uma função. Desta forma, formula-se o problema de otimização topológica de minimização de massa sujeito a restrições (locais) sobre o campo de tensões de von Mises, escrito em termos da função de nível.

A definição da restrição de tensão é proposta fazendo uso da clara representação da fronteira do corpo, que representa uma vantagem das abordagens de curvas de nível. As restrições de tensão são localmente impostas ao problema através de um número finito de pontos de amostra, uniformemente distribuídos ao longo do domínio. Tais restrições são incluídas na função objetivo usando uma técnica de programação matemática Lagrangiano aumentado. Esta técnica é capaz de selecionar automaticamente as restrições de tensão (ativas) no domínio.

Uma análise de sensibilidade analítica da função objetivo penalizada fornece um campo de velocidades que é utilizado nos procedimentos de atualização da topologia definida pela curva de nível (neste trabalho, define-se a curva de nível zero para representar a fronteira). Esta velocidade é usada nas equações de evolução das curvas de nível que, consequentemente, movimenta a fronteira na direção do decréscimo da função objetivo Lagrangiano aumentado. Devido à importância deste campo de velocidades por ser o responsável pelas mudanças topológicas viáveis, propõe-se uma sequência de procedimentos para a regularização e tratamento deste campo, obtendo melhorias significativas à sequência minimizante.

Este trabalho utiliza duas equações de evolução para modificar a topologia. A primeira é a clássica equação de Hamilton-Jacobi, amplamente usada na literatura, que consiste num procedimento convencional para a atualização da fronteira. Apesar dos bons resultados obtidos, o uso desta equação possui algumas desvantagens como a necessidade de reinicialização da função de nível como uma função distância com sinal, e a impossibilidade de gerar novos furos durante o processo de otimização. Por esta razão, evoluções de Hamilton-Jacobi são referidas, por alguns autores, como técnicas de otimização de forma, e não topológica.

A outra equação usada para a propagação da fronteira é uma equação de reação-difusão. Duas consequências importantes são observadas ao usar

esta equação: 1) eliminação do processo de reinicialização conferindo estabilidade à sequência minimizante; e 2) possibilidade de nuclear novos furos, permitindo que a sequência de otimização possa iniciar com diferentes configurações do domínio, até mesmo sem furos.

Quanto à discretização, a formulação proposta tanto usando a equação de Hamilton-Jacobi quanto a equação de reação-difusão, foi implementada usando malhas estruturadas de elementos finitos quadrilaterais. A fim de estender a abordagem para aplicações práticas de engenharia, a formulação usando a equação de reação-difusão também foi discretizada usando malhas poligonais não estruturadas, construídas a partir de tesselações de Voronoi.

RESULTADOS OBTIDOS

Basicamente, os resultados numéricos foram apresentados em três partes (capítulos). Cada capítulo apresenta resultados com alguma particularidade em relação à equação de evolução e/ou discretização: 1) usando a equação de Hamilton-Jacobi (apenas com malhas cartesianas); 2) utilizando a equação de reação-difusão com elementos quadrilaterais; e 3) usando a equação de reação-difusão com elementos poligonais.

A metodologia foi testada para vários tipos de exemplos em duas dimensões apresentando resultados numéricos bem sucedidos, o que comprova a robustez do método proposto. Os resultados mostraram que o algoritmo de otimização foi capaz de identificar as concentrações de tensões e conduzir o projeto para um mínimo local viável.

De modo particular, no que diz respeito ao exemplo clássico de problemas de otimização topológica com restrição de tensão conhecido como estrutura em formato “L”, as topologias finais removeram a indesejável quina (ou canto vivo) inicialmente presente, distribuindo as tensões ao longo de um raio bem-definido.

ABSTRACT

This work focuses on topology optimization for mass minimization with local constraints on the von Mises stress field. Within a level-set context to control the domain, it is developed a constraint procedure that accounts for a continuous activation/deactivation of a finite number of local stress constraints during the optimization sequence. Such constraints are conveniently distributed over the domain and imposed to the problem through an augmented Lagrangian approach. The main objective is to create an efficient algorithm capable of identifying stress concentration regions and drive the topology to a feasible local minimum. The level set evolution makes use of information of the sensitivity analysis to update the structural topology. Initially, being the main goal testing the proposed stress constraint, the level set updating is accomplished by the classical Hamilton-Jacobi equation, widely employed in the literature. Next, a reaction-diffusion equation is used to guide, also via evolution of a level set, the design optimization sequence. The advantages of the latter evolution equation are twofold. Firstly, it allows the creation of new holes during the optimization process, a significant feature for a true topological optimization method. Secondly, reinitialization steps usually found in Hamilton-Jacobi based evolution are eliminated with a significant improvement in convergence. The numerical solution of the reaction-diffusion equation is performed by using regular meshes with standard quads and unstructured polygonal meshes obtained from Voronoi tessellations. A set of benchmark examples in two dimensions achieving successful numerical results assesses the good behavior of the proposed methodology to detect stress concentrations and propose a feasible design.

Keywords: topology optimization, level sets, local stress constraint, augmented Lagrangian, reaction-diffusion equation, polygonal finite elements.

LIST OF FIGURES

1.1 Different categories of structural optimization. 34
3.1 Geometric definitions of a domain composed of solid and voids. 42
3.2 Representation of the indicator function $I_r(\mathbf{x})$ and Heaviside function $H(\phi)$ at a sample point $\mathbf{x}_r$ with neighborhood Ω_r. . . . 47
3.3 Sample point $\mathbf{x}_r$ and its neighborhood Ω_r being intercepted by the border $\partial\Omega$. In this case, $\mathbf{x}_r \notin \Omega$, but the stress constraint may become active because $\Omega \cap \Omega_r \neq \emptyset$, that is, $H_r(\phi) \neq 0$. . . 47
3.4 Function $\Psi(H_r(\phi))$ for different values of q. 48
4.1 Flowchart of the optimization algorithm for obtaining a local optimal design. 60
4.2 Example of a sample point $\mathbf{x}_r$ (coinciding with a node of the finite element mesh) and its neighborhood Ω_r. 62
4.3 Beam problem. 64
4.4 Beam problem: initial level set domain. 65
4.5 Beam problem: optimal structure with mass ratio=0.4628. . . . 65
4.6 Beam problem: stress constraint distribution ($\max_D(g_r) = 6.2 \times 10^{-3}$). 66
4.7 Beam problem: distribution of the Lagrange multipliers at each node in the last iteration. 66
4.8 Beam problem: convergence of the objective function and mass ratio. 67
4.9 Beam problem: convergence of the penalty terms of the objective function. 67
4.10 L-problem: model. 68
4.11 L-problem: initial level set domain for Figure 4.12 to 4.15. . . . 69
4.12 L-problem: (a) optimal structure; (b) stress constraint distribution for $q = 0.25$; and (c) level set surface of the optimal structure. The mass ratio is 0.5437 and $\max_D(g_r) = 3.5 \times 10^{-3}$. 70
4.13 L-problem: (a) optimal structure; (b) stress constraint distribution for $q = 0.5$; and (c) level set surface of the optimal structure. The mass ratio is 0.5099 and $\max_D(g_r) = 2.3 \times 10^{-3}$. 71
4.14 L-problem: (a) optimal structure; (b) stress constraint distribution for $q = 0.75$; and (c) level set surface of the optimal structure. The mass ratio is 0.4802 and $\max_D(g_r) = 5.1 \times 10^{-3}$. 72

4.15 L-problem: (a) optimal structure; (b) stress constraint distribution for $q = 1$; and (c) level set surface of the optimal structure. The mass ratio is 0.4598 and $\max_D(g_r) = 2.1 \times 10^{-3}$. 73
4.16 L-problem: convergence of the objective function and mass ratio for $q = 0.5$. 74
4.17 L-problem: convergence of the penalty terms of the objective function for $q = 0.5$. 74
4.18 L-problem: distribution of the Lagrange multipliers at each node in the last iteration for the case where $q = 0.5$. 75
4.19 L-problem: (a) initial level set domain; (b) obtained design for $q = 0.5$; and (c) stress constraint distribution with $\max_D(g_r) = 5.6 \times 10^{-3}$. The mass ratio is 0.5066. 76
4.20 L-problem: (a) initial level set domain; (b) obtained design for $q = 0.5$; and (c) stress constraint distribution with $\max_D(g_r) = 1.7 \times 10^{-3}$. The mass ratio is 0.5630. 77
4.21 L-problem: results for different meshes and $q = 0.5$; (a) initial level set domain; (b) final design for coarse mesh (mass ratio = 0.4791); (c) stress constraints distribution for coarse mesh ($\max_D(g_r) = 3.2 \times 10^{-3}$); (d) final design for refined mesh (mass ratio = 0.4623); and (e) stress constraints distribution for refined mesh ($\max_D(g_r) = 4.0 \times 10^{-3}$). 78
4.22 Crack problem: model and stress constraint distribution with high stress concentration at the fracture tip ($\max_D(g_r) = 0.4628$). 79
4.23 Crack problem: (a) initial level set domain and (b) optimal structure for $q = 0.5$. The mass ratio is 0.2945. 80
4.24 Crack problem: stress constraint distribution for $q = 0.5$ ($\max_D(g_r) = -5.04 \times 10^{-2}$). 81
4.25 Convergence of the objective function and mass ratio for the crack problem ($q = 0.5$). 81
4.26 Convergence of the penalty terms of the objective function for the crack problem ($q = 0.5$). 82
5.1 L-problem: (a) initial level set domain; Intermediate results at: (b) iteration 5; (c) iteration 10; (d) iteration 20; (e) iteration 50; (f) iteration 100; (g) iteration 150; (h) iteration 600; and (i) iteration 1000. 93
5.2 L-problem: (a) final design at iteration 1200; and (b) stress constraint distribution with $\max_D(g_r) = 6.1 \times 10^{-3}$. The mass ratio is 0.4643. 94

5.3 L-problem: level set function of the final design. 94
5.4 L-problem: convergence history for the mass ratio, the compliance and the regularization term. 95
5.5 L-problem: (a) initial level set domain; Intermediate results at: (b) iteration 40; (c) iteration 80; (d) iteration 110; (e) iteration 120; (f) iteration 140; (g) iteration 200; (h) iteration 600; and (i) iteration 1000. 96
5.6 L-problem: (a) final design at iteration 1200; (b) stress constraint distribution with $\max_D(g_r) = 6.8 \times 10^{-5}$; (c) convergence history for the mass ratio (final mass ratio is 0.5066); (d) compliance convergence (final compliance value is 205.78); and (e) regularization term. 97
5.7 L-problem: convergence history for the penalty terms and the objective function. For the objective function, it is shown the convergence for each iteration and for each update of the Lagrange multipliers (external loop). 97
5.8 L-problem: (a) initial level set domain; (b) obtained design for $\tau = 5 \times 10^{-5}$; (c) stress constraint distribution of **b**; (d) obtained design for $\tau = 1 \times 10^{-5}$; (e) stress constraint distribution of **d**; (f) obtained design for $\tau = 7 \times 10^{-6}$; and (g) stress constraint distribution of **f**. 98
5.9 Cantilever beam problem: model. 100
5.10 Cantilever beam problem: (a) initial level set domain; Intermediate results at: (b) iteration 40; (c) iteration 45; (d) iteration 50; (e) iteration 55; (f) iteration 60; (g) iteration 150; (h) iteration 300; and (i) iteration 400. 100
5.11 Cantilever beam problem: (a) final design at iteration 600; and (b) stress constraint distribution with $\max_D(g_r) = -1.8 \times 10^{-2}$. The mass ratio is 0.3107 and the compliance value is 118.35. 101
5.12 Cantilever beam problem: (a) initial level set domain; (b) final design for $p = 1.001$; (c) stress constraint distribution for $p = 1.001$; (d) final design for $p = 1.5$; (e) stress constraint distribution for $p = 1.5$; (f) final design for $p = 3$; and (g) stress constraint distribution for $p = 3$. 102
5.13 Cantilever beam problem: convergence history for the mass ratio and objective function, the compliance $W(\phi)$ and the regularization term for the final design shown in Figure 5.12(f), where $p = 3$. 103

5.14 Cantilever beam problem: (a) final design for the compliance problem; and (b) stress constraint distribution with $\max_D(g_r) = 0.9$. The mass constraint was set to 40% of the total mass. The compliance $W(\phi)$ of the final design is 76.8. The initial configuration has the material domain filled with material. 104
5.15 Crack problem (model 1): results for different meshes; (a) initial level set domain; (b) final design for 100×50 mesh; (c) stress constraints distribution for 100×50 mesh; (d) final design for 180×90 mesh; and (e) stress constraints distribution for 180×90 mesh. 105
5.16 Crack problem: model 2. 106
5.17 Crack problem (model 2): (a) initial configuration; (b) final design (mass ratio is 0.34 and compliance is 59.73); (c) stress constraint distribution with $\max_D(g_r) = -6.6 \times 10^{-4}$; (d) initial configuration; (e) final design (mass ratio is 0.33 and compliance is 57.16); and (f) stress constraint distribution with $\max_D(g_r) = -3.14 \times 10^{-4}$. 107
5.18 Crack problem (model 2): (a) 3D level set function for Fig. 5.17b; and (b) 3D level set function for Fig. 5.17e. 107
5.19 Crack problem (model 2): convergence history for the mass ratio and objective function, the compliance and the regularization term for the final configuration shown in Figure 5.17(e). 108
6.1 (a) Illustration of the triangular areas used to define w_i in expression (6.2). (b) Triangulation of the reference regular polygon and integration points defined on each triangle 113
6.2 Representation of the level set function ϕ in a polygonal element, where the dark region represents the material in the element. The value of ϕ on the centroid is the average of the ϕ values at the nodes. 114
6.3 Example of sample points $\mathbf{x}_r$ (coinciding with the nodes of the polygonal finite element mesh) and its neighborhoods Ω_r defined from centroids of the elements (blue lines). The black lines correspond to the polygonal mesh. 115
6.4 Illustration of the CVT-based finite volume scheme. The parameter S_i represents the distance between the centroids of the common elements to the nodes r and r_i, and H_i denotes the distance between the nodes r and r_i. 116

6.5 The strain field is calculated at the integration points. The strain at a node $\boldsymbol{\varepsilon}(i)$ is assumed as the average of the strains $\boldsymbol{\varepsilon}_{ip}$ closer the node. 119
6.6 Wrench problem: model. 120
6.7 Wrench problem: Initial level set topology with 10,000 polygonal element mesh. 121
6.8 Wrench problem: (a) Final design using FE scheme; and (b) stress constraint distribution. 121
6.9 Wrench problem: (a) Final design using FV scheme; and (b) stress constraint distribution. 122
6.10 Wrench problem: Objective function and mass ratio along the 320 iterations for (a) FE scheme and (b) FV scheme. 123
6.11 Wrench problem: (a) final design for the compliance problem; and (b) stress constraint distribution with $\max_D(g_r) = 5.75$. The mass constraint was set to 40% of the total mass. The compliance $W(\phi)$ of the final design is 111.66. 124
6.12 L-problem: (a) Initial level set topology; (b) Final design using FE scheme; (c) stress constraint distribution; (d) Final design using FV scheme; (e) stress constraint distribution. . . . 125
6.13 L-problem: (a) initial level set domain; Intermediate results at iterations: (b) 40; (c) 60; (d) 80; (e) 200; and (f) 400. 127
6.14 L-problem: (a) final design at iteration 800; (b) stress constraint distribution with $\max_D(g_r) = 5.3 \times 10^{-3}$; (c) convergence history of the mass ratio (final mass ratio is 0.6277); (d) convergence of the stress penalization terms (linear and quadratic); and (e) convergence of the compliance term (final value is 197.43). 128
6.15 L-problem: model 2. 129
6.16 L-problem: (a) random initial level set domain; Intermediate results at iterations: (b) 40; (c) 160; (d) 200; (e) 260; and (f) 360. 130
6.17 L-problem: (a) final design at iteration 600; (b) zoom near the reentrant corner; (c) stress constraint distribution with $\max_D(g_r) = 8.99 \times 10^{-4}$; and (d) convergence history of the mass ratio (final mass ratio is 0.4782) and objective function. . 131
6.18 Crack problem: (a) Initial level set topology; (b) Final design using FE scheme; (c) stress constraint distribution; (d) Final design using FV scheme; (e) stress constraint distribution. . . . 132

6.19 Crack problem: (a) Initial level set domain; (b) final design using FV scheme; (c) stress constraint distribution; (d) convergence history of the objective function; and (e) behavior of the regularization term. 133
6.20 Crack problem: Models with loading applied in a hole. 135
6.21 Crack problem: (a) Initial level set topology; (b) Final design to the loading applied at position 1; (c) stress constraint distribution of b; (d) Initial level set topology; (e) Final design to the loading applied at position 2; and (f) stress constraint distribution of e. 136
6.22 Cantilever modified: model. 136
6.23 Cantilever modified: Stress constraint distribution of the model with $\max_D(g_r) = 1.04$. 137
6.24 Cantilever modified: (a) initial level set domain; Intermediate results at iterations: (b) 10; (c) 40; (d) 70; (e) 200; and (f) 400. 137
6.25 Cantilever modified: (a) Final design from the initial configuration of Fig. 6.24a; and (b) stress constraint distribution with $\max_D(g_r) = -2.8 \times 10^{-3}$ 138
6.26 Cantilever modified: (a) random initial level set domain; (b) final design; and (c) stress constraint distribution with $\max_D(g_r) = -7 \times 10^{-3}$ 140
6.27 Cantilever modified: Objective function and mass ratio for different initial configurations. 141
6.28 Cantilever modified: (a) Final design for the compliance problem; and (b) stress constraint distribution with $\max_D(g_r) = 1.96$. 141
6.29 Cantilever modified: Considering the initial level set domain the design obtained for the compliance problem (Fig. 6.28a), (a) shows the final design after 400 iterations for the stress-constrained problem; and (b) stress constraint distribution with $\max_D(g_r) = 9.19 \times 10^{-4}$ 142

LIST OF TABLES

5.1 L-problem: Summary of results for the obtained final designs 99
5.2 Cantilever beam problem: summary of the results shown in Figure 5.12. 101
5.3 Crack problem (model 1): parameters of the results shown in Figure 5.15. 104
6.1 Wrench problem: Summary of results to the final designs using FE and FV schemes. 122
6.2 L-problem: Summary of results to the final designs of Fig. 6.12 using FE and FV schemes. 123
6.3 Crack problem: Summary of results to the final design of Fig. 6.18 and 6.19. 134
6.4 Crack problem: Summary of results to the final designs of Fig. 6.21 for the hole in the positions 1 and 2. 134
6.5 Cantilever modified: Summary of results of the final topologies shown in Fig. 6.25 (from an initial configuration with holes), Fig. 6.26 (from a random initial domain), Fig. 6.28a (obtained design to the minimum compliance problem) and Fig. 6.29a (initial configuration is Fig. 6.28a). 139

SYMBOLS

Ω	Admissible design for the optimization problem
$\mathscr{B}$	Linear elastic isotropic body
$\partial\Omega$	Boundary of Ω
Γ_D	Portion of $\partial\Omega$ with Dirichlet boundary conditions
Γ_H	Portion of $\partial\Omega$ with homogeneous Neumann boundary conditions
$\boldsymbol{\tau}$	surface loads
Γ_N	Portion of $\partial\Omega$ with Neumann boundary conditions
D	Fixed background domain consisting of all admissible shapes Ω
$\mathbf{u}$	Admissible displacement field satisfying equilibrium
U	Set of kinematically admissible displacements
V	Set of kinematically admissible variations
$a(\cdot,\cdot)$	Bilinear operator representing the virtual work of internal forces
$l(\cdot)$	Linear operator representing the virtual work of external surface forces
$\boldsymbol{\varepsilon}$	Linearized strain field
∇^s	Symmetric gradient operator
$\mathbf{C}$	Elasticity tensor
ρ	Material density
g	Stress constraint
μ	Weight factor to the compliance term
ϕ	Level set function
$\mathbf{x}$	Location of a point
$H(\phi)$	Heaviside function
ρ_1	Density for phase 1 (solid material)
ρ_2	Density for phase 2 (weak material)
$\mathbf{C}_1$	Elasticity tensor for phase 1 (solid material)
$\mathbf{C}_2$	Elasticity tensor for phase 2 (weak material)
p	Penalization exponent
Nel	Number of elements in the finite element mesh
e	Element of the finite element mesh
D_e	Domain of element
$\mathbf{C}^e(\phi)$	Elasticity tensor of element e
$a^e(\phi)$	Area fraction of material within the element
r	Sample point
$\mathbf{x}_r$	Location of sample point r
N_r	Number of sample points
$\boldsymbol{\varepsilon}_r$	Strain tensor evaluated at a sample point

$\boldsymbol{\sigma}_r$	Stress tensor evaluated at a sample point
σ_r^{vM}	von Mises stress evaluated at a sample point
σ_{adm}	Yield stress
$\mathbf{s}_r$	Deviatoric stress tensor evaluated at a sample point
$H_r(\phi)$	Function computing the volumetric (area) fraction of material 1 contained in a neighborhood Ω_r
Ω_r	Neighborhood of a sample point
a_r	Physics volume (area) of the neighborhood Ω_r
$I_r(\mathbf{x})$	Indicator function
g_r	Stress constraint defined at a sample point
q	Exponent of function Ψ
Ψ	Function defined as equal to $H_r(\phi)^q$
k	k-th iteration of the external loop
α_r	Lagrange multiplier of stress constraints
c	Penalization factor
h_r	Function of the r-th stress constraint
ε	Small tolerance
β	Factor to update the penalization factor
$J(\phi)$	Objective function
$\pounds$	Lagrangian function
$\boldsymbol{\lambda}$	Lagrange multiplier of state equation, adjoint field
$\delta\phi$	Admissible variation of ϕ
$\delta\mathbf{u}$	Admissible variation of $\mathbf{u}$
$\delta\boldsymbol{\lambda}$	Admissible variation of $\boldsymbol{\lambda}$
$\mathbf{A}_r$	Tensor containing the derivatives of the stress constraints with respect to the stress invariants
$\delta(\phi)$	Dirac delta function
$V(\phi)$	Shape gradient density
$\mathbf{v}$	Velocity vector
t	Pseudo-time
$\mathbf{n}$	Unitary vector normal to the boundary
$\|\nabla\phi\|$	Norm of the gradient of ϕ
v_n	Velocity normal to the boundary
Δt	Time step
T	Time integration
$P(\phi)$	Perimeter penalization term
$\hat{J}(\phi)$	Regularized objective function
γ	Penalization factor for the perimeter regularization
$\hat{V}(\phi)$	Regularized shape gradient density

$V_{\log}(\phi)$	Logarithmic scaling on $\hat{V}(\phi)$
$\bar{V}(\phi)$	Smoothed-regularized velocity
$H^1(D)$	Hilbert space
κ	Smoothing-regularization parameter
$\mathbf{T}_1$	Matrix containing the product of the interpolation function
$\mathbf{T}_2$	Matrix containing the product of the derivatives of the interpolation functions
$\mathbf{N}$	Array of the interpolation function
Δx	Minimum grid size
ϕ^0	Initial level set function
Ω_0	Initial domain defined by ϕ^0
N_{iter}	Number of minimization iterations of the internal loop
j	j-th iteration of the internal loop
v_{nj}	Normal velocity for the j-the iteration
ΔT	Time integration period
ϕ^i	ϕ for the i-th iteration of the level set updating for a given normal velocity v_{nj}
m	Number of level set updatings for a given normal velocity v_{nj}
Δt_{CFL}	Time step satisfying the CFL condition
N_e	Number of elements attached to a node
$\mathbf{B}_e$	Array of shape function derivatives of element e
$\mathbf{U}_e$	Array of nodal displacements of element e
E_1	Young's modulus for phase 1 (solid material)
E_2	Young's modulus for phase 2 (weak material)
ν	Poisson's ratio
$S(\phi)$	Sign function
$J_R(\phi)$	Regularized objective function
τ	Diffusion coefficient
$v(\phi)$	Regularized reaction term (velocity field)
$\mathbf{V}$	Velocity vector of reaction-diffusion equation discretized
$\boldsymbol{\xi}$	Interior point of a reference polygon
w_i	Interpolant of Wachspress shape function for the node i
C^∞	Space of functions with derivatives of all order continuous
ϕ_c	Value of ϕ in the centroid of the polygonal element
N_{node}	Number of nodes of the element
$\mathscr{R}$	Set of nodes in a polygonal mesh
z	Slack variables

CONTENTS

1 INTRODUCTION 33
1.1 MOTIVATION AND OBJECTIVES 33
1.2 THESIS LAYOUT 35
2 LITERATURE REVIEW 37
3 FORMULATION OF THE PROBLEM 41
3.1 INTRODUCTION 41
3.2 BASIC STATEMENT 41
3.3 LEVEL SET-BASED FORMULATION 43
3.4 STATE EQUATIONS 44
3.5 STRESS CONSTRAINT DEFINITION 45
3.6 AUGMENTED LAGRANGIAN-BASED FORMULATION . . . 49
3.7 SENSITIVITY ANALYSIS 50
4 LEVEL SET EVOLUTION VIA HAMILTON-JACOBI EQUATION 55
4.1 INTRODUCTION 55
4.2 OPTIMIZATION BY MOVING THE LEVEL SET 55
4.2.1 Velocity field 56
4.2.2 Level set regularization and treatment on the normal velocity field 56
4.3 DISCRETIZATION AND NUMERICAL IMPLEMENTATION 58
4.3.1 Optimization algorithm 58
4.3.2 Sample points stress evaluation 61
4.4 NUMERICAL RESULTS 62
4.4.1 Beam problem 64
4.4.2 L-problem 68
4.4.3 Crack problem 79
4.5 CONCLUDING REMARKS 79
5 LEVEL SET EVOLUTION VIA REACTION-DIFFUSION EQUATION 85
5.1 INTRODUCTION 85
5.2 OPTIMIZATION BY MOVING THE LEVEL SET 85
5.2.1 Treatment and regularization on the reaction term (velocity field) 88
5.3 DISCRETIZATION AND NUMERICAL IMPLEMENTATION 89
5.3.1 Implicit scheme-based finite element (FE) method 89
5.3.2 Optimization algorithm 90
5.4 NUMERICAL RESULTS 91

5.4.1 L-problem 92
5.4.2 Cantilever beam problem 99
5.4.3 Crack problem 103
5.5 CONCLUDING REMARKS 108
6 A LEVEL SET WITH A POLYGONAL FINITE ELEMENT APPROACH 111
6.1 INTRODUCTION 111
6.2 POLYGONAL FINITE ELEMENTS 111
6.3 NUMERICAL IMPLEMENTATION 113
6.3.1 Sample points and its neighborhoods 114
6.3.2 CVT-based finite volume (FV) method for unstructured meshes 116
6.3.3 Sample points stress evaluation 118
6.4 NUMERICAL RESULTS 118
6.4.1 Wrench problem 120
6.4.2 L-problem 123
6.4.3 Crack problem 126
6.4.4 Cantilever modified 134
6.5 CONCLUDING REMARKS 143
7 CONCLUSIONS 145
7.1 SUMMARY OF CONTRIBUTIONS 145
7.2 OVERALL CONSIDERATIONS 146
7.3 FUTURE WORK 147
Appendix A – Augmented Lagrangian method 157
Appendix B – Derivative of the failure function 161
Appendix C – Derivative of the regularized objective function . . 165
Appendix D – Wachspress shape function gradient 167

1 INTRODUCTION

1.1 MOTIVATION AND OBJECTIVES

The last 20 years has been characterized by a remarkable popularization of numerical simulation, including multiphysics analysis, solid design and integrating tools like optimization packages. In the area of mechanical and structural design, many engineering application areas like civil, naval, aerospace, automotive, bioengineering, among others, have profited from huge benefits offered by the use of these numerical tools available in commercial codes. Classical mathematical programming algorithms, or more recently heuristic based algorithms, are offered as an alternative to finding local and global minimizers.

Focusing the area of structural design optimization, most problems can be set up by the definition of the following subjects:

- Design variables within a design space;
- Performance cost and constraint functions;
- State problem (e.g. equilibrium or balance problem);
- Optimization algorithm.

Also, generally the problem can be written in the following standard form:

$$\min_{\mathbf{l}\in L} \quad f(\mathbf{l})$$

$$\text{subject to:} \begin{cases} h_i(\mathbf{l}) = 0, & i = 1,...,k, \\ g_j(\mathbf{l}) \leq 0, & j = 1,...,r, \end{cases}$$

where $\mathbf{l}$ are the design variables defining a point within the design space L. Scalar function f and vectorial functions h_i and g_j are performance functions evaluating displacement, energy, stress, strain, mass, frequencies, and so on, and representing respectively objective, equality and inequality constraints of the problem.

A general classification of structural optimization problems comprises the following three categories: parametric, shape and topology optimization. Parametric optimization is the case in which design variables are identified

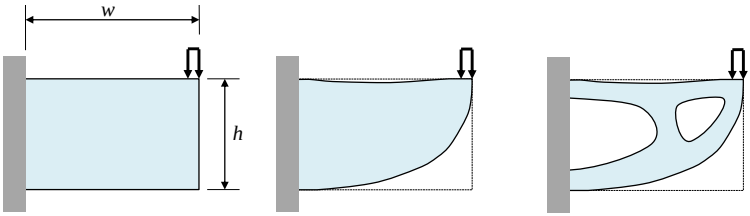

(a) Parametric (b) Shape (c) Topology

Figure 1.1: Different categories of structural optimization.

by material (elasticity modulus, Poisson's ratio, yield stress, etc.) and/or geometric (height, thickness, width, etc.) parameters defined within the problem formulation. In this case, the domain over which the (usually differential or integral) state equations are defined remains constant. Shape optimization, on the other hand, involves the modification of the above mentioned domain by means of boundary control but keeping the same form (isomorphic mappings) of it. Finally, the considered freest approach is that called topology optimization, in which both the shape and the topology of the domain are variable. This last approach can be understood as an optimal determination of the material distribution within a specified background predefined region without making any assumptions about the final design itself. Figure 1.1 shows these three categories. The last category, namely Structural Topology Optimization, is within the subject of the present research.

Strain energy (compliance) minimization has been the most widely used objective function in structural topology optimization due to its particularly convenient mathematical properties. The so-called *compliance problem* is usually implemented and presently available as a common numerical tool in commercial finite element codes. However, an apparently simpler problem that searches for the lightest design that satisfy failure constraints is lacking from these codes for the simple reason of still being a research subject. Due to its mathematical and numerical difficulties this problem has received increasing attention of researchers in the last 10 years, but only a few works have succeeded to obtain convincing results.

Thus, the purpose of the present work is to contribute on the consolidation of efficient strategies to deal with this problem. In particular, to propose an approach to address the topology optimization problem of mass

minimization subject to local stress constraints. This proposition is motivated by the following two-fold observations: a) previous encouraging results obtained with the augmented Lagrangian approach for the stress constraint treatment; and b) the possibility of attenuating the mathematical/numerical difficulty known as stress-singularity when the domain is controlled by a level-set field that allows for a clear separation between material and void regions within the background domain. Within this context, the main objective of this thesis (scientific contribution) is to create an algorithm capable of identifying stress concentration regions and change the topology to a feasible local minimum.

1.2 THESIS LAYOUT

In order to cover the subjects involved in this study, this thesis is organized as follows. A focused literature review about the particular problem of this work is provided in Chapter 2. The remainder of the text begins by setting the basic formulation of the topology optimization problem in Chapter 3. This chapter also states the stress constraint definition, presents the augmented Lagrangian formulation using the level set concepts, and shows the analytical sensitivity analysis of the final Lagrangian function.

The formulated optimization problem was then tested by using two different level set evolution equations. In Chapter 4 the sensitivity analysis of the objective function is related to the velocity field of a Hamilton-Jacobi equation that is used for level set updating. On the other hand, Chapter 5 employs a reaction-diffusion equation to guide the level set evolution. In both chapters the optimization algorithm, operational details, and numerical results are presented.

All numerical results presented in Chapter 4 and 5 were obtained with structured meshes (quadrilateral bilinear elements). Unstructured meshes, on the other side, may provide additional flexibility to define geometry constraints and boundary conditions. Due to this, polygonal finite elements that showed to have good performance in topology optimization problems were tested in Chapter 6. Finally, Chapter 7 presents a summary of contributions and some overall considerations, as well as proposals for future work.

2 LITERATURE REVIEW

Topological optimization of continuous structures has been an area of research of important recognition in the last decades. While most of the literature focuses on the problem of maximum stiffness (compliance problem) due to its own mathematical characteristics, in the last years, attention has regained to the structural problem related to minimizing of mass subject to local stress constraints. However, this problem possesses some difficulties. One being the difficulty introduced by local constraints, that is, stress levels at every material point must be constrained according to failure criteria which characterizes a large number of constraints to the problem. Another is related to the so-called stress singularity phenomenon.

The study in [2] is the first work addressing topology optimization problems with stress constraints in the context of continuum structures using the concept of intermediate artificial material Solid Isotropic Microstructure with Penalization (SIMP). The article emphasizes the difficulty of the treatment of the stress constraint and the singularity phenomenon. After this article several studies have been published on this subject, most of them within the last decade. In [1], local constraints are treated using an Augmented Lagrangian approach combined with SIMP concepts. The approach in [1] was later extended to multiple load cases [3] and contact boundary conditions [4]. The work in [5] also extended the homogenization method to treat problems involving stress but with objective functions corresponding to minimum stress design subject to volume constraint.

A different strategy followed by several works (see, for example, [6, 7]) is to use integral forms of stress constraints based on p-norms or on the Kreisselmeier–Steinhauser (KS) function. Unfortunately, although this choice allows for a decrease of computational costs, the corresponding results are sometimes unable to account for stress concentrations. In an attempt to overcome this difficulty, different studies propose localization strategies in which a finite number of constraints are defined as integrals over subregions within the domain [8, 9, 10, 11, 12, 13, 14]. The work in [15] proposes the use of the superconvergent patch recovery schemes to evaluate the stress field leading to a more reliable evaluation of the global constraint.

Another classical issue associated to stress constraints are the singular optima on the design space, undesirable outcome of topology approaches based on intermediate densities. Two main strategies are seen in the literature to deal with this problem. The first is the so-called ε-relaxed approach of Cheng and Guo [16]. The second, attributed to Bruggi [17, 18] is called qp-

approach. A comparative analysis of different propositions for stress-driven topology designs based on intermediate materials can be found in [9].

Some papers based on stress but considering failure criterion other than von Mises are seen in [19, 20, 21] where materials with different behavior in tension and compression are discussed. Similarly, constraints based on fatigue failure are considered in [22].

Concerning the topology optimization technique itself, formulations using implicit functions for design control have gained popularity. The researchers in [23] are among the first to introduce the level set method in structural topology optimization problems. In [24], the topology optimization problem is formulated using an implicit function controlled by nodal variables. The papers of Allaire et al. [25] and Wang et al. [26] are considered the first ones combining an evolution equation (time integration of Hamilton-Jacobi equations) for the level set with the sensitivity analysis of a cost function for structural topology optimization. However, a well known drawback of this conventional evolution scheme is the inability of creating new holes [27]. Consequently, these approaches are sometimes called not topology but shape optimization techniques. Among different alternatives to overcome this limitation it is worth mentioning the work [28], where hole nucleation steps based on the information of topological gradients are included, [29] using radial basis functions, [30] using evolutionary structural optimization and [31] considering a secondary level set function. Another drawback is the reinitialization of the level set function as a signed distance function, classicaly needed with Hamilton-Jacobi evolution. In order to treat the numerical issues related to the reinitialization procedure, alternative level set-based techniques have been developed for shape and topology optimization [32, 33, 34, 35, 36].

An interesting approach proposed by Yamada and co-workers [37, 38] regularizes the optimization problem by introducing a reaction-diffusion equation for the evolution of the level set. This proposition avoids the undesirable reinitialization procedure and also allows for the generation of new holes. The method was applied for compliance, compliant mechanisms, and eigenfrequency problems. For a survey on the level set method, the reader may refer to [27] and [39], and for a very thorough review regarding the use of different level set techniques for structural topology optimization, see [40] and [41]. It is worth mentioning that all cited works using level set approaches refer to compliance problems.

One of the first studies using the level set method for problems involving stresses is found in Allaire and Jouve [42], where a norm of the stress

over the domain is used as objective function. In [43] is presented an extension of that work to irregular domains and non-uniform meshes using an isoparametric level set method. A different approach is due to [44] dealing with stress concentration minimization of 2D fillets based on the level set description and the extended finite element method (X-FEM). The study in [45] minimizes a global measure of stress where the background mesh is constantly updated to follow the moving boundaries.

Early works using the level set method to deal with minimization of mass and stress constraints (main subject of the present thesis) were presented at conferences, for example, in [46], where the stress constraints are aggregated in a single equivalent global constraint, and in [47], where regularized formulations for stress-related topology optimization are proposed [48]. Subsequent papers on the same problem have been published, as for example, the work in [49] that uses constraint aggregation techniques to deal with the local nature of the stress dividing the domain in sub-domains called group constraints; the article in [50] presents a level set/X-FEM approach to reduce the volume of a structure proposing a single stress constraint (called shape equilibrium constraint function); and the recent paper [51] includes local stress constraints into the optimization problem via Augmented Lagrangian approach while the design is modified by a level set guided by a Hamilton-Jacobi equation. On the other hand, Zhang et al. [52] used the level set method for designing stiff structures with less stress concentrations.

Also related to the formulations based on implicit function description, the phase-field method has been tested for stress constraints problems in [53, 54]. An important different approach is found in works [55, 21] where a simple algorithm based on topological derivative information provide excellent results for the local stress constrained problem. In [56], the authors combined the topological derivative to define the tracking of the level set for stress-constrained problems.

The present work deals with the problem of mass minimization subject to von Mises-based stress constraints imposed locally in a finite number of sample points uniformly distributed along the domain. The formulation is based on the level set approach to control the domain, while the augmented Lagrangian mathematical programming technique is used to account for the stress constraints in a form similar to that proposed in [1]. This technique is able to automatically perform the appropriate selection of the relevant (active) stress constraints among the domain. The main reason behind the choice of a level-set approach to handle the stress constrained problem is the expectation that it may attenuate the mathematical/numerical difficulty known as

singularity-stress (singular optima in the design space [16]) since the level-set field allows for a clear separation between material and void regions within the background domain.

3 FORMULATION OF THE PROBLEM

3.1 INTRODUCTION

In this chapter, the basic formulation of the topology optimization problem of mass minimization subject to local stress constraints is presented. To this aim, an implicit representation of the domain based on a level set approach is used. Stress constraints are included into the objective function on an augmented Lagrangian approach basis, taking advantage of the clear definition of the body boundary provided by the level set approach. An analytical sensitivity analysis of the penalized objective function provides a descent direction that comes in the form of a velocity field used by the level set (topology) updating procedure. It is worth emphasizing that the concepts presented here were already published in [51].

3.2 BASIC STATEMENT

Let Ω be an open domain in $\mathbb{R}^n$ $(n = 2,3)$ occupied by a linear elastic isotropic body $\mathscr{B}$ with a smooth boundary $\partial\Omega$ split in three non-overlapping regions

$$\partial\Omega = \Gamma_D \cup \Gamma_H \cup \Gamma_N. \tag{3.1}$$

Dirichlet boundary conditions are applied in Γ_D, while Γ_H is submitted to homogeneous Neumann conditions. Non-zero surface tractions $\boldsymbol{\tau}$ act on Γ_N. It is assumed that Γ_H may change during the optimization procedure, while Γ_D and Γ_N remain fixed. It is also assumed that all the admissible configurations Ω are defined within a fixed background domain D (Figure 3.1).

The principle of virtual work states that the body $\mathscr{B}$ achieves equilibrium when the displacement field $\mathbf{u} \in U$ satisfies the expression

$$a(\mathbf{u},\mathbf{v}) = l(\mathbf{v}) \quad \forall \mathbf{v} \in V, \tag{3.2}$$

$$a(\mathbf{u},\mathbf{v}) = \int_\Omega \mathbf{C}\boldsymbol{\varepsilon}(\mathbf{u}) \cdot \boldsymbol{\varepsilon}(\mathbf{v})\, d\Omega\ , \tag{3.3}$$

$$l(\mathbf{v}) = \int_{\Gamma_N} \boldsymbol{\tau} \cdot \mathbf{v}\, d\partial\Omega\ , \tag{3.4}$$

where U and V denote the sets of kinematically admissible displacements and admissible variations, respectively. The bilinear operator $a(\cdot,\cdot)$ represents the

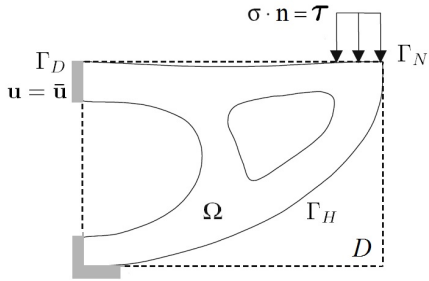

Figure 3.1: Geometric definitions of a domain composed of solid and voids.

virtual work of internal forces, and $l(\cdot)$ is a linear form accounting for the virtual work of external surface forces. $\boldsymbol{\varepsilon}(\mathbf{u}) = \nabla^s \mathbf{u}$ is the linear strain tensor and $\mathbf{C}$ is the isotropic elasticity tensor**.** For simplicity reasons, the problem in which the loading is design dependent is not addressed here (see, for example, [10]), and therefore, no body forces are considered in (3.4). Moreover, since U is a translation of the space V, the problem may be rewritten for simplicity reasons in such a way that $\mathbf{u} \in V$ modifying the term $l(\mathbf{v})$ conveniently.

The problem of minimum mass with local stress (failure) constraints can be stated as:
Problem P_1:

$$\min_{\Omega} \quad m(\mathbf{u}) = \int_{\Omega} \rho \, d\Omega + \mu \int_{\Omega} \frac{1}{2} \mathbf{C}\boldsymbol{\varepsilon}(\mathbf{u}) \cdot \boldsymbol{\varepsilon}(\mathbf{u}) \, d\Omega \, ,$$

$$\text{subject to:} \begin{cases} a_{\Omega}(\mathbf{u}, \mathbf{v}) - l_{\Omega}(\mathbf{v}) = 0, & \forall \mathbf{v} \in V, \\ g(\mathbf{u}) \leq 0, & \forall \mathbf{x} \in \Omega \, , \end{cases} \tag{3.5}$$

where ρ is the material density and $g(\mathbf{u})$ is a stress constraint that must be satisfied everywhere in Ω. The second term of the objective function corresponds to the compliance (strain energy), which $\mu \geq 0$ is a weighting factor. As observed in [48], "the compliance term is introduced into the objective function in order to play the role of excluding the pathological structures with small stiffness from the feasible domain". Moreover, considering the present problem, mass is insensible to the place where the material is removed and the compliance term also provides a preference direction on the sensitivity analysis. The weighting factor μ also plays the role of scaling factor since

unities of energy and mass are different.

Problem P_1, however, is too general for practical optimization purposes, and it will be rewritten in the present work as a moving boundary problem controlled by a level set function.

3.3 LEVEL SET-BASED FORMULATION

The level set approach in topology optimization consists of relating the boundary $\partial\Omega$ with the zero-valued level set of a function $\phi : D \to \mathbb{R}$:

$$\phi(\mathbf{x}) > 0 \quad \forall \mathbf{x} \in \Omega \,, \tag{3.6}$$

$$\phi(\mathbf{x}) = 0 \quad \forall \mathbf{x} \in \partial\Omega \,, \tag{3.7}$$

$$\phi(\mathbf{x}) < 0 \quad \forall \mathbf{x} \in D \backslash (\Omega \cup \partial\Omega). \tag{3.8}$$

Expressions (3.6)-(3.8) define the region in D occupied by Ω, by the boundary $\partial\Omega$, and by the complement $D\backslash(\Omega \cup \partial\Omega)$. Variations of ϕ modify the corresponding level sets and consequently the position of the boundary $\partial\Omega$ [57, 27]. Using the Heaviside function

$$H(\phi(\mathbf{x})) = \begin{cases} 1 \,, \text{ if } \phi(\mathbf{x}) \geq 0, \\ 0 \,, \text{ if } \phi(\mathbf{x}) < 0, \end{cases} \tag{3.9}$$

problem P_1 may be reformulated as an integral over a fixed domain D (also known as background domain) within which subdomain Ω evolves guided by the function ϕ:
Problem P_2:

$$\min_{\phi} \quad m_\phi(\mathbf{u}) = \int_D \left[\rho(\phi) + \frac{\mu}{2} \mathbf{C}(\phi) \boldsymbol{\varepsilon}(\mathbf{u}) \cdot \boldsymbol{\varepsilon}(\mathbf{u}) \right] \, dD,$$

$$\text{subject to:} \begin{cases} a_\phi(\mathbf{u}, \mathbf{v}) = l_\phi(\mathbf{v}), & \forall \mathbf{v} \in V, \\ H(\phi) g(\mathbf{u}) \leq 0, & \forall \mathbf{x} \in D, \end{cases} \tag{3.10}$$

where

$$\rho(\phi) = H(\phi)\rho_1 + (1 - H(\phi))\rho_2, \tag{3.11}$$

$$a_\phi(\mathbf{u}, \mathbf{v}) = \int_D \mathbf{C}(\phi) \boldsymbol{\varepsilon}(\mathbf{u}) \cdot \boldsymbol{\varepsilon}(\mathbf{v}) \, dD, \tag{3.12}$$

$$l_\phi(\mathbf{v}) = \int_{\Gamma_N} \boldsymbol{\tau} \cdot \mathbf{v} \, d\partial\Omega, \tag{3.13}$$

$$\mathbf{C}(\phi) = H(\phi)^p \mathbf{C}_1 + (1 - H(\phi)^p)\mathbf{C}_2. \tag{3.14}$$

Here $p \geq 1$ is a penalization exponent[1]. Equations (3.11) and (3.14) define the fields ρ and $\mathbf{C}$ being dependent of two material phases $(\rho_1, \mathbf{C}_1)$ and $(\rho_2, \mathbf{C}_2)$. It is assumed that the material 1 occupies the domain Ω while the material 2 is occupied by the complement $D \backslash (\Omega \cup \partial\Omega)$. In the present case, the properties of material 2 are assumed to have null values or, by operational reasons during the solution of the equilibrium equations, values significantly lower than those of material 1, that is, $\rho_2 << \rho_1$ and $\|\mathbf{C}_2\| << \|\mathbf{C}_1\|$.

The usage of the Heaviside function within the integral expressions has consequences that are worthy of careful discussion. One of the advantages of this approach is the possibility of using a fixed mesh over which the domain Ω evolves guided by the function ϕ. Within this context, the frontier $\partial\Omega$ does not coincide in general with the elements boundaries, and therefore, many of them are cut by $\partial\Omega$ in two parts belonging to material 1 and 2. A possible way of getting rid of this ambiguous situation is to conform the discretization to the crossing boundary by means of remeshing [45] or, for example, by using discontinuous functions of X-FEM type [44, 50]. These options, however, introduce extra computational effort and will not be followed in the present work. Consequently, two technical questions must be addressed. The first one is related to the computation of integrals $m_\phi(\mathbf{u})$ and $a_\phi(\mathbf{u}, \mathbf{v})$, particularly on those elements cut by $\partial\Omega$. The second one is the definition of the stress constraint in those cut elements. These two questions are the subject of the coming sections.

3.4 STATE EQUATIONS

The finite element counterpart of expression (3.12) involves the integration over all elements, some of which are crossed by the boundary $\partial\Omega$. In these cases, the material property distribution (expression (3.14)) is discon-

[1]The reasons for the inclusion of an exponent p in Eq.(3.14) are twofold: Firstly, despite exponent p has no effect on the exact Heaviside function (3.9), its use on a discretized counterpart of $\mathbf{C}(\phi)$, detailed in next section, will drive to the classical "ersatz" material model for those elements cut by the implicit boundary $\partial\Omega$. Secondly, it plays a formal role in the derivative of $\mathbf{C}(\phi)$ with respect to function ϕ, explained in Section 3.7.

tinuous within the element, and the integration operation must take this fact into account. To address this issue, integrals involving $\mathbf{C}(\phi)$ are approximated by a representative constant value $\mathbf{C}^e(\phi)$ over the element:

$$\begin{aligned} a_\phi(\mathbf{u},\mathbf{v}) &= \sum_{e=1}^{Nel} \int_{D_e} \mathbf{C}(\phi)\boldsymbol{\varepsilon}(\mathbf{u}) \cdot \boldsymbol{\varepsilon}(\mathbf{v})\, dD, \\ &\approx \sum_{e=1}^{Nel} \int_{D_e} \mathbf{C}^e(\phi)\boldsymbol{\varepsilon}(\mathbf{u}) \cdot \boldsymbol{\varepsilon}(\mathbf{v})\, dD, \end{aligned} \tag{3.15}$$

where

$$\mathbf{C}^e(\phi) = a^e(\phi)^p \mathbf{C}_1 + [1 - a^e(\phi)^p]\, \mathbf{C}_2 \ , \qquad a^e(\phi) = \frac{\displaystyle\int_{D_e} H(\phi)\, dD}{\displaystyle\int_{D_e} dD} \tag{3.16}$$

where $a^e(\phi)$ is the area (volume) fraction of element e covered by material 1. It is worth noting that this expression is nothing but the classical "ersatz" material model [25, 26, 58], significant only for elements cut by $\partial\Omega$. However, it must be emphasized that in this case, there is no microstructure involved but an element partially covered by Ω.

3.5 STRESS CONSTRAINT DEFINITION

In the way problem P_2 is presented in (3.10), the stress constraint $g(\mathbf{u})$ must be satisfied almost everywhere in D. Nevertheless, this condition is inevitably transferred sometime during discretization to a finite number of constraints commonly associated to the integration points or nodes of the mesh. Being aware of this fact, it has been chosen here to substitute, at formulation level, the continuum constraint g in (3.5) by a finite number of stress constraints g_r defined at sample points $\mathbf{x}_r \in D$, $r = 1,...,N_r$ (it is expected that the quantity and distribution of sample points is linked with the discretization in the sense that provides a consistent approximation of the continuum case). It must be noted that just those points $\mathbf{x}_r$ belonging to Ω must be effectively considered within the constraint set. Thus, in order to avoid the problems associated to the discontinuous inclusion-exclusion of constraints as long as the boundary of Ω passes over a sample point, a regularization scheme is here proposed. Aiming at this, let $\boldsymbol{\varepsilon}_r(\mathbf{u})$ be the strain evaluated at $\mathbf{x}_r \in D$ and $\boldsymbol{\sigma}_r$

the stress tensor defined by

$$\boldsymbol{\sigma}_r := \mathbf{C}_1 \boldsymbol{\varepsilon}_r(\mathbf{u}). \tag{3.17}$$

The classical von Mises stress criterion can be written as

$$\frac{\sigma_r^{vM}}{\sigma_{adm}} - 1 \leq 0 \ , \quad \sigma_r^{vM} = \sqrt{\frac{3}{2}\mathbf{s}_r \cdot \mathbf{s}_r} \ , \quad \mathbf{s}_r = \mathrm{dev}(\boldsymbol{\sigma}_r), \tag{3.18}$$

where σ_r^{vM} and $\mathbf{s}_r$ are, respectively, the von Mises stress and the tensor of deviatoric stresses evaluated at $\mathbf{x}_r \in D$, and σ_{adm} is the yield stress. Let $H_r(\phi)$ also be a function that computes the volumetric (area) fraction of material 1 contained in a neighborhood Ω_r of $\mathbf{x}(r)$ as follows:

$$H_r(\phi) = \frac{1}{a_r} \int_D I_r(\mathbf{x}) H(\phi) \, dD, \tag{3.19}$$

in which

$$I_r(\mathbf{x}) = \begin{cases} 1 \ , \text{ if } \mathbf{x} \in \Omega_r \ , \\ 0 \ , \text{ if } \mathbf{x} \notin \Omega_r \ , \end{cases} \quad \text{and} \quad a_r = \int_D I_r(\mathbf{x}) \, dD, \tag{3.20}$$

are the indicator function and the physics volume (area) of the neighborhood Ω_r, respectively. Figure 3.2 shows a schematic representation of these functions. In this way, $H_r(\phi)$ varies continuously between 0 and 1 as long as Ω covers Ω_r.

Using the definitions earlier, our purpose is to define a stress constraint g_r that follows the continuous variation of $H_r(\phi)$ during the movement of $\partial\Omega$ in such a way that the stress at $\mathbf{x}_r$ be significant whenever $\Omega \cap \Omega_r \neq \emptyset$. Figure 3.3 shows a sample point $\mathbf{x}_r$ whose corresponding constraint g_r might become active even though this point is outside Ω. A possible expression to accomplish this task is

$$g_r(\mathbf{u}, \phi) = \Psi(H_r(\phi)) \frac{\sigma_r^{vM}}{\sigma_{adm}} - 1 \leq 0, \tag{3.21}$$

with

$$\Psi(H_r(\phi)) = H_r(\phi)^q. \tag{3.22}$$

Function Ψ in (3.21) activates or deactivates the stress constraint depending on the position of the considered sample point. Points localized near the boundary are progressively considered as the area fraction $H_r(\phi)$ goes from

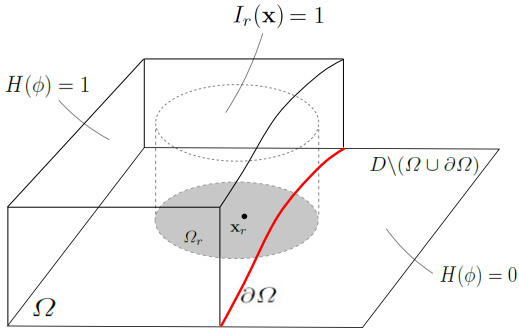

Figure 3.2: Representation of the indicator function $I_r(\mathbf{x})$ and Heaviside function $H(\phi)$ at a sample point $\mathbf{x}_r$ with neighborhood Ω_r.

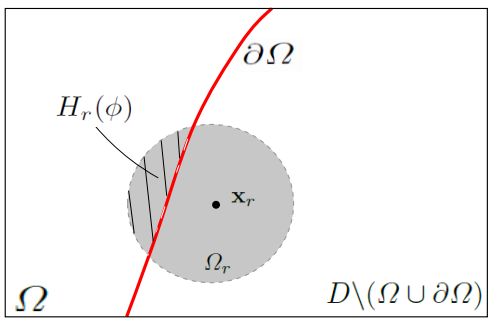

Figure 3.3: Sample point $\mathbf{x}_r$ and its neighborhood Ω_r being intercepted by the border $\partial\Omega$. In this case, $\mathbf{x}_r \notin \Omega$, but the stress constraint may become active because $\Omega \cap \Omega_r \neq \emptyset$, that is, $H_r(\phi) \neq 0$.

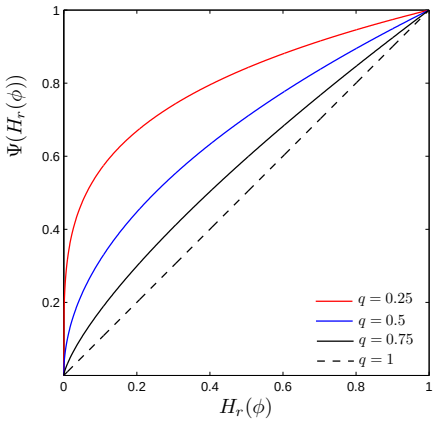

Figure 3.4: Function $\Psi(H_r(\phi))$ for different values of q.

0 to 1. The exponent $q \in (0,1]$ is used to set Ψ a continuum approximation of the 0-1 function. If $q = 1$ a proportionality between stress significance and area fraction $H_r(\phi)$ is recovered. Conversely, if $q \to 0$, the stress of the point is completely considered as soon as a small area fraction of the sample point neighborhood is covered by material 1. Figure 3.4 shows the behavior of $\Psi(H_r(\phi))$ for different values of q. It is clear that (3.22) represents a regularized version of the discontinuous 0-1 function.

It is important to remark that regardless the point $\mathbf{x}_r$ is inside or outside the body, the corresponding stress $\boldsymbol{\sigma}_r$ is always calculated by Equation (3.17) and the stress constraint by Equation (3.21). The variable that turns $\boldsymbol{\sigma}_r$ significant or not is the area fraction $H_r(\phi)$. The use of the function Ψ is conceptually related to the singularity stress phenomenon and therefore to the qp-approach [17] and more indirectly, to the ε-relaxation [16] used in [2]. Nevertheless, it is important to remark once again that, different from these last mentioned works, the present approach involves no intermediate material. Expression (3.21) should then be interpreted as a regularized way to effectively consider the stress of a sample point as long as the boundary Γ_H moves in D.

On the basis of the above considerations, the minimization problem is reformulated as follows:

Problem P_3:

$$\min_{\phi} \quad m_\phi(\mathbf{u}) = \int_D \left[\rho(\phi) + \frac{\mu}{2}\mathbf{C}(\phi)\boldsymbol{\varepsilon}(\mathbf{u})\cdot\boldsymbol{\varepsilon}(\mathbf{u})\right]\, dD,$$

$$\text{subject to:} \begin{cases} a_\phi(\mathbf{u},\mathbf{v}) = l_\phi(\mathbf{v}), & \forall \mathbf{v} \in V, \\ g_r(\mathbf{u},\phi) \leq 0, & r = 1,\ldots,N_r \end{cases} \tag{3.23}$$

where $g_r(\mathbf{u},\phi)$ is given by (3.21) and N_r is the total number of sample points $\mathbf{x}_r$ in D.

3.6 AUGMENTED LAGRANGIAN-BASED FORMULATION

Following the conventional augmented Lagrangian approach [59, 60], the stress constraints of problem P_3 are raised up to the objective function by means of a penalization comprised by a linear and quadratic term. The main idea consists of defining a sequence $\{\alpha_r^k\}$, $k = 1,2,\ldots$ converging to the Lagrange multipliers α_r that satisfy the necessary optimality conditions of P_3. The problem then takes the following new expression:
Problem P_4: for given values of penalization factor $c^k > 0$ and Lagrange multipliers $\alpha_r^k \in \mathbb{R}$, solve the minimization

$$\min_{\phi} \quad J^k(\phi) = \int_D \left[\rho(\phi) + \frac{\mu}{2}\mathbf{C}(\phi)\boldsymbol{\varepsilon}(\mathbf{u})\cdot\boldsymbol{\varepsilon}(\mathbf{u})\right]\, dD$$
$$+ \sum_{r=1}^{N_r} \left\{ \alpha_r^k h_r(\mathbf{u},\phi) + \frac{c^k}{2}\left[h_r(\mathbf{u},\phi)\right]^2 \right\}, \tag{3.24}$$

$$\text{subject to:} \quad a_\phi(\mathbf{u},\mathbf{v}) = l_\phi(\mathbf{v}), \quad \forall \mathbf{v} \in V, \tag{3.25}$$

where $\mathbf{u}$ is the solution of (3.25) and $h_r(\mathbf{u},\phi)$ is a function of the r-th stress constraint given by [59, 60]:

$$h_r(\mathbf{u},\phi) = \max\left\{ g_r(\mathbf{u},\phi)\ ;\ -\frac{\alpha_r^k}{c^k} \right\}. \tag{3.26}$$

For more detail on how to obtain the expression above, see Appendix A. Once the minimum is achieved (or after a conveniently specified number of

iterations), verify the condition:

$$\left|\alpha_r^k \, g_r^k\right| < \varepsilon, \tag{3.27}$$

where ε is a small tolerance. If (3.27) is not satisfied, update the Lagrange multipliers and penalization factor:

$$\begin{aligned} &\alpha_r^{k+1} = \max\left\{\alpha_r^k + c^k g_r^k \; ; \; 0\right\}, \\ &c^{k+1} = \beta c^k, \quad \beta > 1, \quad 0 < c^k < c_{\max}, \quad \forall k \in N. \end{aligned} \tag{3.28}$$

Let $k = k+1$ and restart the process.

3.7 SENSITIVITY ANALYSIS

The total derivative of $J(\phi)$, defined by (3.24), must be calculated considering the satisfaction of the state equation (3.25). It is worth emphasizing that $J(\phi)$ includes already the penalization terms (via augmented Lagrangian) corresponding to stress constraints. To this aim, a Lagrangian function $\pounds$ is defined as follows:

$$\begin{aligned} \pounds(\phi, \mathbf{u}, \boldsymbol{\lambda}) = &\int_D \left[\rho(\phi) + \frac{\mu}{2}\mathbf{C}(\phi)\boldsymbol{\varepsilon}(\mathbf{u}) \cdot \boldsymbol{\varepsilon}(\mathbf{u})\right] \, dD + \sum_{r=1}^{N_r} \left\{\alpha_r h_r(\mathbf{u}, \phi)\right. \\ &\left. + \frac{c}{2}\left[h_r(\mathbf{u}, \phi)\right]^2\right\} + a_\phi(\mathbf{u}, \boldsymbol{\lambda}) - l_\phi(\boldsymbol{\lambda}) \quad \forall \mathbf{u}, \boldsymbol{\lambda} \in V, \end{aligned} \tag{3.29}$$

where $\boldsymbol{\lambda} \in V$ is the Lagrangian multiplier. The total variation of $\pounds$ with respect to $\phi, \mathbf{u}$ and $\boldsymbol{\lambda}$ is

$$\delta\pounds(\phi, \mathbf{u}, \boldsymbol{\lambda}) = \frac{\partial \pounds}{\partial \phi}[\delta\phi] + \frac{\partial \pounds}{\partial \mathbf{u}}[\delta\mathbf{u}] + \frac{\partial \pounds}{\partial \boldsymbol{\lambda}}[\delta\boldsymbol{\lambda}] \, , \tag{3.30}$$

where $\delta\phi$, $\delta\mathbf{u}$ and $\delta\boldsymbol{\lambda}$ are admissible variations of the respective arguments. For a given ϕ, a point is stationary in relation to $(\mathbf{u}, \boldsymbol{\lambda})$ if it satisfies the following conditions:

$$\frac{\partial \pounds}{\partial \boldsymbol{\lambda}}[\delta\boldsymbol{\lambda}] = 0 \quad \text{and} \quad \frac{\partial \pounds}{\partial \mathbf{u}}[\delta\mathbf{u}] = 0 \, . \tag{3.31}$$

The solution of (3.31a) retrieves the state equation. The second condition (3.31b) gives what is commonly known as adjoint equation, whose solution

provides the adjoint field $\boldsymbol{\lambda}$:

$$\int_D \mathbf{C}(\phi)\left[\mu\boldsymbol{\varepsilon}(\mathbf{u})+\boldsymbol{\varepsilon}(\boldsymbol{\lambda})\right]\cdot\boldsymbol{\varepsilon}(\delta\mathbf{u})\,dD = \\ -\sum_{r=1}^{N_r}\left[\alpha_r + ch_r(\mathbf{u},\phi)\right]\frac{\partial h_r(\mathbf{u},\phi)}{\partial \mathbf{u}}\left[\delta\mathbf{u}\right] \quad \forall\delta\mathbf{u}\in V. \tag{3.32}$$

It is shown in detail in Appendix B that the derivative of $h_r(\mathbf{u},\phi)$ takes the form

$$\frac{\partial h_r(\mathbf{u},\phi)}{\partial \mathbf{u}}\left[\delta\mathbf{u}\right] = \mathbf{C}_r\mathbf{A}_r(\mathbf{u},\phi)\cdot\boldsymbol{\varepsilon}_r(\delta\mathbf{u}), \tag{3.33}$$

where $\mathbf{A}_r(\mathbf{u},\phi)$, given by Equation (B.11), is a tensor that contains the derivatives of the stress constraints with respect to the stress invariants. Substituting (3.33) in (3.32),

$$\int_D \mathbf{C}(\phi)\left[\mu\boldsymbol{\varepsilon}(\mathbf{u})+\boldsymbol{\varepsilon}(\boldsymbol{\lambda})\right]\cdot\boldsymbol{\varepsilon}(\delta\mathbf{u})\,dD = \\ -\sum_{r=1}^{N_r}\left[\alpha_r + ch_r(\mathbf{u},\phi)\right]\mathbf{C}_r\mathbf{A}_r(\mathbf{u},\phi)\cdot\boldsymbol{\varepsilon}_r(\delta\mathbf{u}) \quad \forall\delta\mathbf{u}\in V, \tag{3.34}$$

whose solution provides the adjoint field $\boldsymbol{\lambda}$.

Finally, the partial derivative of $\pounds(\phi,\mathbf{u},\boldsymbol{\lambda})$ with respect to ϕ is

$$\frac{\partial \pounds}{\partial \phi}[\delta\phi] = \\ \int_D \left\{(\rho_1-\rho_2)+p(\mathbf{C}_1-\mathbf{C}_2)H(\phi)^{p-1}\left[\frac{\mu}{2}\boldsymbol{\varepsilon}(\mathbf{u})+\boldsymbol{\varepsilon}(\boldsymbol{\lambda})\right]\cdot\boldsymbol{\varepsilon}(\mathbf{u})\right\}\frac{\partial H(\phi)}{\partial\phi}\left[\delta\phi\right]\,dD \\ +\sum_{r=1}^{N_r}\left\{\left[\alpha_r+ch_r(\mathbf{u},\phi)\right]\frac{\partial h_r(\mathbf{u},\phi)}{\partial\phi}[\delta\phi]\right\} \quad \forall\mathbf{u},\boldsymbol{\lambda}\in V. \tag{3.35}$$

Since $h_r(\mathbf{u},\phi)=\max\left\{g_r(\mathbf{u},\phi);-\frac{\alpha_r}{c}\right\}$, two possible expressions are achievable for its derivative:
(1) If $h_r(\mathbf{u},\phi)=g_r(\mathbf{u},\phi)$, then

$$\frac{\partial h_r(\mathbf{u},\phi)}{\partial\phi}\left[\delta\phi\right] = \frac{\sigma_r^{vM}}{\sigma_{adm}}\frac{\partial\Psi(H_r(\phi))}{\partial H_r(\phi)}\frac{\partial H_r(\phi)}{\partial\phi}\left[\delta\phi\right], \tag{3.36}$$

$$\frac{\partial H_r(\phi)}{\partial \phi}[\delta\phi] = \frac{1}{a_r}\int_D I_r(\mathbf{x})\frac{\partial H(\phi)}{\partial \phi}[\delta\phi]\,dD, \tag{3.37}$$

and thus,

$$\frac{\partial h_r(\mathbf{u},\phi)}{\partial \phi}[\delta\phi] = \int_D \frac{I_r(\mathbf{x})}{a_r}\frac{\sigma_r^{vM}}{\sigma_{adm}}\frac{\partial \Psi(H_r(\phi))}{\partial H_r(\phi)}\frac{\partial H(\phi)}{\partial \phi}[\delta\phi]\,dD. \tag{3.38}$$

(2) If $h_r(\mathbf{u},\phi) = -\dfrac{\alpha_r}{c}$, then

$$\frac{\partial h_r(\mathbf{u},\phi)}{\partial \phi}[\delta\phi] = 0. \tag{3.39}$$

Let us call upon the identity[2]

$$\frac{\partial H(\phi)}{\partial \phi}[\delta\phi] = \delta(\phi)\delta\phi,$$

where $\delta(\phi)$ is the Dirac function.

To end this issue, let us assume that the set $(\phi,\mathbf{u},\boldsymbol{\lambda})$ satisfies the equations in (3.31), that is, state and adjoint equations. In this case, the total variation of the Lagrangian function $\delta\pounds$ reduces to its partial derivative with respect to ϕ (see Eq. 3.30). Moreover, it is easy to see by simple substitution, that this partial derivative corresponds to the required total derivative $dJ(\phi)/d\phi$ (see e.g. [25]) given in the distributional form as:

$$\delta\pounds(\phi,\mathbf{u},\boldsymbol{\lambda}) = \frac{\partial \pounds}{\partial \phi}[\delta\phi] = \frac{dJ(\phi)}{d\phi}[\delta\phi] = \left(\frac{dJ(\phi)}{d\phi},\delta\phi\right) = \int_D V(\phi)\delta(\phi)\delta\phi\,dD. \tag{3.40}$$

Since $\delta\phi$ is any test function, it is possible to state formally that the derivative of the objective function is given by

$$\frac{dJ(\phi)}{d\phi} = V(\phi)\delta(\phi), \tag{3.41}$$

[2]Verify the distinction in notation between the variation $\delta\phi$ and the Dirac function $\delta(\phi)$.

where

$$V(\phi) = \begin{cases} (\rho_1 - \rho_2) + p(\mathbf{C}_1 - \mathbf{C}_2)H(\phi)^{p-1}\left(\dfrac{\mu}{2}\boldsymbol{\varepsilon}(\mathbf{u}) + \boldsymbol{\varepsilon}(\boldsymbol{\lambda})\right)\cdot\boldsymbol{\varepsilon}(\mathbf{u}) \\ \qquad + \displaystyle\sum_{r=1}^{N_r}\left\{[\alpha_r + c g_r(\mathbf{u},\phi)]\,\dfrac{I_r(\mathbf{x})}{a_r}\,\dfrac{\sigma_r^{vM}}{\sigma_{adm}}\,\dfrac{\partial\Psi(H_r(\phi))}{\partial H_r(\phi)}\right\}, \\ \qquad\qquad \text{if } g_r(\mathbf{u},\phi) \geq -\dfrac{\alpha_r}{c}, \\ \\ (\rho_1 - \rho_2) + p(\mathbf{C}_1 - \mathbf{C}_2)H(\phi)^{p-1}\left(\dfrac{\mu}{2}\boldsymbol{\varepsilon}(\mathbf{u}) + \boldsymbol{\varepsilon}(\boldsymbol{\lambda})\right)\cdot\boldsymbol{\varepsilon}(\mathbf{u}), \\ \qquad\qquad \text{if } g_r(\mathbf{u},\phi) < -\dfrac{\alpha_r}{c}, \end{cases} \tag{3.42}$$

is a field defined over D. In fact, $V(\phi)$ is the well-known velocity field in topology optimization problems, also known as shape gradient density [61]. The next chapters make use of $V(\phi)$ in the corresponding evolution equations to change the topology to a feasible local minimum. It will be proved that $V(\phi)$ is the term responsible for the decrease of the objective function by moving the level set boundary in this direction.

4 LEVEL SET EVOLUTION VIA HAMILTON-JACOBI EQUATION

4.1 INTRODUCTION

Previous chapter presented the topology optimization problem of mass minimization subject to local (von Mises-based) stress constraints formulated in terms of a penalization (augmented Lagrangian) and an implicit level set geometry control. In this context, a level set evolution technique is needed to move the boundaries to a local minimum. The first attempt was performed considering the solution of the so-called Hamilton Jacobi equation. This procedure is described in the present chapter.

4.2 OPTIMIZATION BY MOVING THE LEVEL SET

A classic approach to modify ϕ in (3.24) in order to obtain a minimization sequence consists of solving the time differential equation of Hamilton-Jacobi

$$\frac{\partial \phi(\mathbf{x}(t),t)}{\partial t} + \mathbf{v}(\mathbf{x}(t)) \cdot \nabla \phi(\mathbf{x}(t),t) = 0, \tag{4.1}$$

where $\mathbf{v}(\mathbf{x}(t))$ is the velocity for every point $\mathbf{x}(t)$ on the boundary. Since $\mathbf{n} = -\nabla\phi / \|\nabla\phi\|$, the above equation can be rewritten as

$$\frac{\partial \phi(\mathbf{x}(t),t)}{\partial t} - v_n(\mathbf{x}(t)) \|\nabla \phi(\mathbf{x}(t),t)\| = 0, \tag{4.2}$$

where $v_n = \mathbf{v} \cdot \mathbf{n}$ is the velocity normal to the boundary $\partial\Omega$, that is, for all $\mathbf{x}(t)$ with $\phi(\mathbf{x}(t)) = 0$. Equation (4.2) is commonly known in the literature as the level set equation [57, 27, 39]. A key issue in this equation is the choice of a proper field v_n which guarantees that for a sufficiently small time interval Δt, the new field ϕ decreases $J(\phi)$. Following the same arguments used by [25] and [26], it is concluded that the derivative $\frac{dJ}{d\phi}[\delta\phi]$ obtained in (3.40) provides this information.

4.2.1 Velocity field

A Taylor expansion of the objective function is formally given by

$$J(\phi + t\delta\phi) = J(\phi) + t\frac{dJ}{d\phi}[\delta\phi] + \vartheta(t^2). \tag{4.3}$$

It is shown in the literature (see, for example, [25, 26]) that choosing $\delta\phi$ based on (4.2)

$$\delta\phi = \frac{\partial\phi}{\partial t} = v_n\|\nabla\phi\|, \tag{4.4}$$

with

$$v_n = -V(\phi), \tag{4.5}$$

where $V(\phi)$ is given by (3.42), it is obtained that, for a small enough $t > 0$, the value of $J(\phi)$ decreases:

$$J(\phi + t\delta\phi) = J(\phi) - t\int_D V^2(\phi)\delta(\phi)\|\nabla\phi\|dD + \vartheta(t^2) < J(\phi). \tag{4.6}$$

In other words, using $v_n = -V(\phi)$ in the solution of the level set equation (4.2) is equivalent to move the boundary $\partial\Omega$ in direction $v_n\mathbf{n}$ with an amplitude proportional to the period of time integration $[0,T]$. The choice of a value for T will be justified later.

4.2.2 Level set regularization and treatment on the normal velocity field

It is also known that in order to obtain efficient minimization sequences, different improvements on v_n are convenient, so long as they satisfy descent condition (4.6).

The first consideration is related to the inclusion of a classic perimeter regularization which has the effect of smoothening the boundary [62, 63]. A consistent way of doing that is by modifying the objective function by the addition of a perimeter penalization term $P(\phi)$:

$$\hat{J}(\phi) := J(\phi) + P(\phi), \tag{4.7}$$

$$P(\phi) = \int_D \gamma\delta(\phi)\|\nabla\phi\| dD, \tag{4.8}$$

where $\gamma > 0$ is a penalization factor. By deriving the new expression (4.7), it can be shown that the field $V(\phi)$ modifies to

$$\hat{V}(\phi) := V(\phi) - \gamma \operatorname{div} \mathbf{n}\ , \tag{4.9}$$

where $\operatorname{div}\mathbf{n}$ plays the role of average curvature of the level set.

Other observed phenomenon in the present problem is that the velocity field (3.42) has severe variations in amplitude as a consequence of local stress constraints naturally appearing because of arbitrary moving geometries. This characteristic has the undesirable effect of locking the boundary: only very limited portions of the boundary move, while all the rest remains almost static. To avoid this effect, it is proposed a modified definition for v_n that provided significant improvements:

$$V_{\log}(\phi) = \begin{cases} \ln(\hat{V}(\phi)+1), & \text{if } \hat{V}(\phi) \geq 0, \\ -\ln(-\hat{V}(\phi)+1), & \text{if } \hat{V}(\phi) < 0. \end{cases} \tag{4.10}$$

Because this operation preserves the signal of v_n, it also satisfies the descent condition (4.6).

In addition, although the field $V_{\log}(\phi)$ calculated in (4.10) is defined everywhere, just its value on the boundary $\partial\Omega$ should be accounted for in (4.6). Among different techniques available to extend/regularize this field over D [23, 25, 63], the most performing for the present case was the smoothing scheme proposed in [64]. A new velocity $\bar{V}(\phi) \in H^1(D)$ more regular than $V_{\log}(\phi)$ is obtained by solving the variational problem

$$\int_D (\kappa\nabla\bar{V}(\phi)\cdot\nabla X + \bar{V}(\phi)X)\, dD = \int_D X V_{\log}(\phi) dD, \quad \forall X \in H^1(D) \tag{4.11}$$

where $\kappa > 0$ is a small smoothing-regularization parameter. Thus, $\bar{V}(\phi)$ intrinsically takes more regularity due to the classical regularity theory for elliptic equations. Finally, after performing all operations defined earlier, the velocity field v_n is normalized by

$$v_n = \frac{-\bar{V}(\phi)}{\max(|\bar{V}(\phi)|)}. \tag{4.12}$$

4.3 DISCRETIZATION AND NUMERICAL IMPLEMENTATION

The finite element method (FEM) is employed to solve the state equation (3.10) and the adjoint equation (3.34). The problem is generically formulated for any dimension but tested here with only 2D numerical examples under plane stress conditions. For the implementation of the examples, it is used a single mesh to discretize the level set function and for the analysis of finite elements, which uses a quadrilateral bilinear element.

For the discrete solution of the Hamilton-Jacobi equation (4.2), an upwind finite difference scheme is used. Furthermore, a reinitialization procedure is performed to maintain the level set function as a signed distance function. For details about the numerical solution schemes for Equation (4.2), the readers are referred to [25, 26, 27, 39].

The variational problem in (4.11) was also solved using FEM. Thus, the array $\bar{\mathbf{V}}$ is obtained from the linear equation system:

$$(\mathbf{T}_1 + \kappa \mathbf{T}_2)\,\bar{\mathbf{V}} = \mathbf{T}_1\,\mathbf{V}_{\log}. \tag{4.13}$$

where

$$\mathbf{T}_1 = \bigcup_e \int_{D_e} \overset{e}{\mathbf{N}}{}^T \overset{e}{\mathbf{N}}\, dD, \tag{4.14}$$

$$\mathbf{T}_2 = \bigcup_e \int_{D_e} \nabla \overset{e}{\mathbf{N}}{}^T \nabla \overset{e}{\mathbf{N}}\, dD. \tag{4.15}$$

Here, $\bigcup_e$ represents the union set of elements and $\mathbf{N}$ is the interpolation function. In numerical practice it is used a value of κ between 1-4 times $(\Delta x)^2$, being Δx the minimum grid size. High values of κ may smooth too much the velocity field (this means that the function might miss important relevant information somewhere) leading the algorithm to an undesirable local minimum.

4.3.1 Optimization algorithm

From the sensitivity analysis, a velocity field v_n was naturally defined for the level set equation (4.2). Thus, the optimization process should lead the structure to a local optimal design. The optimization algorithm to solve problem P_4 is then summarized in the succeeding text:

External loop:

1. Initialization of the level set function ϕ^0 as a signed distance function defining the initial guess $\Omega_0 \subset D$.

2. Define $k = 1$, $c^k > 0$, $\alpha_r^k \in \mathbb{R}$.

3. Perform the *internal loop* (see below) to minimize function $J^k(\phi, \alpha_r^k, c^k)$ obtaining ϕ^k.

4. Update c^k and α_r^k using (3.28).

5. $k = k+1$. Return to step 3.

The step 3 of the *external loop*, called *internal loop*, consists of the minimization of objective function J^k for fixed given values of c^k and α_r^k. However, as indicated in [60], the minimization in step 3 may be performed partially or, equivalently, substituted by a sufficient descent condition. For practical purposes this means that a fixed number of minimization iterations, say N_{iter}, must be accomplished prior to the Lagrange multipliers updating in step 4. Then, the iterative procedure for a sufficient decrease of $J^k(\phi, \alpha_r^k, c^k)$ is the following:

Internal loop: for $j = 1$ *to* $j \leq N_{iter}$:

1. Obtain the discretized fields $\mathbf{u}_j$ and $\boldsymbol{\lambda}_j$ by solving, respectively, the state equation (3.25) and adjoint equation (3.34).

2. Compute the velocity field $v_{nj}(\mathbf{u}_j, \boldsymbol{\lambda}_j)$ by means of Equation (4.12).

3. Solve the level set equation (4.2) during a time integration period ΔT_j, $T_{j+1} = T_j + \Delta T_j$, chosen such that $J(\phi_{j+1}) \leq J(\phi_j)$.

4. If $\left|J(\phi_{j+1}) - J(\phi_j)\right| \leq \varepsilon$, then stop the iterative process; otherwise continue.

5. $j = j+1$. Go to step 1.

Figure (4.1) shows a flowchart of the optimization algorithm presented above.

The discrete version of the level set equation (4.2) is given by

$$\phi^{i+1} = \phi^i - \Delta t(v_{nj}\|\nabla\phi^i\|), \tag{4.16}$$

where $i = 1...m$ is the number of level set updatings for a given normal velocity v_{nj} during the time integration period $\Delta T_j = m\Delta t$. The time integration

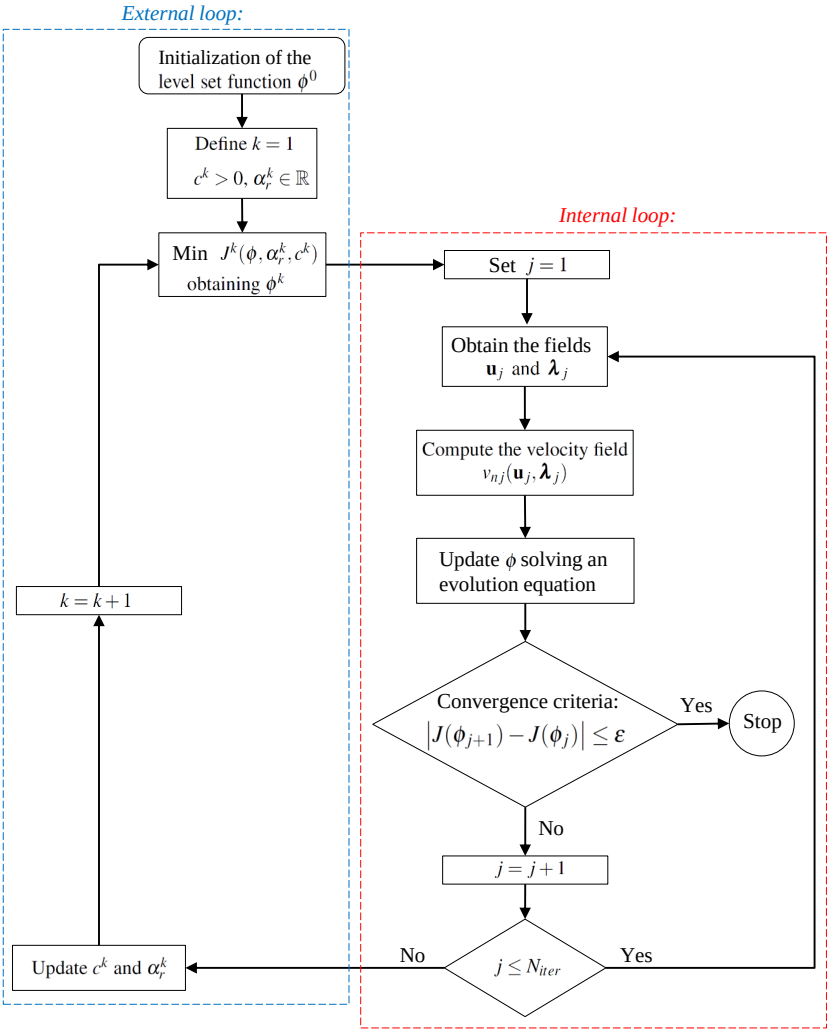

Figure 4.1: Flowchart of the optimization algorithm for obtaining a local optimal design.

period ΔT_j is analogous to the step size of a line search minimization in the descent direction provided by the velocity v_{nj}. The number of updatings m is conveniently chosen to satisfy a descent condition given in step 3 of the internal minimization loop. The numerical technique used here is an explicit first-order upwind scheme (see, for example, [27, 39]) where Δt must satisfy the so-called CFL condition:

$$\Delta t = \Delta t_{CFL} \leq \frac{\min(\Delta x)}{\max|v_n|}. \tag{4.17}$$

It has been noted in the numerical experiments that parameters m (associated to the time integration period) and N_{iter} (associated to the number of internal loops) have appreciable influence on the final optimal configuration. The first one is somehow limited by the descent condition of step 3 of the internal loop. In the present implementation, the objective function is tested periodically, and the time integration period ΔT_j is chosen when $J(\phi_j)$ stops decreasing (similarly to an inexact step determination). The choice of N_{iter} is more heuristical. At present, it has been chosen $N_{iter} = 20$ in most cases, unless particular cases indicated.

4.3.2 Sample points stress evaluation

The number of sample points should be enough to identify all possible stress peaks that may occur during the optimization process. Thus, in the present implementation the sample points $\mathbf{x}_r$ do coincide with the nodes of the finite element mesh. This distribution of sample points is consistent with the objective of enforcing the stress constraint all over the domain. It is then possible to say that with this choice, the number and position of sample points follow the resolution of the stress field provided by the finite element mesh. The corresponding neighborhood Ω_r is square with a length of a finite element size (see Figure 4.2). In this way, there is no overlapping among distinct neighborhoods, that is, $\Omega_{r_x} \cap \Omega_{r_y} = \emptyset$ for $x \neq y$, and all of domain D is covered by the neighborhoods.

Moreover, because bilinear quadrilateral elements are used, the strain field is discontinuous among elements. Thus, the strain $\boldsymbol{\varepsilon}_r(\mathbf{x}_r)$ at a node $\mathbf{x}_r$ is computed using a classical recovering technique given by the average of the

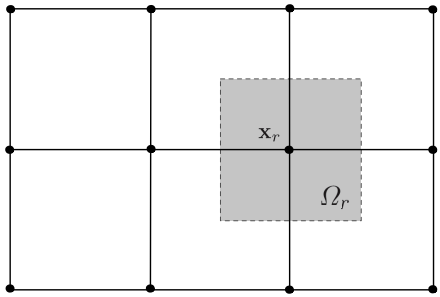

Figure 4.2: Example of a sample point $\mathbf{x}_r$ (coinciding with a node of the finite element mesh) and its neighborhood Ω_r.

elementar strains attached to the node:

$$\boldsymbol{\varepsilon}_r(\mathbf{x}_r) = \sum_{e=1}^{N_e} \frac{\mathbf{B}_e(\mathbf{x}_r)\mathbf{U}_e}{N_e}, \tag{4.18}$$

where N_e is the number of elements e attached to node $\mathbf{x}_r$, $\mathbf{B}_e(\mathbf{x}_r)$ is the array of shape function derivatives of element e, and $\mathbf{U}_e$ is the array of nodal displacements of element e. The stress at this node is then evaluated by (3.17) and the stress constraint by (3.21) where the value of $H_r(\phi)$ is computed using the code available in [58] in which an exact Heaviside function is used.

4.4 NUMERICAL RESULTS

In all examples, the densities of the solid and weak materials are respectively $\rho_1 = 1$ and $\rho_2 = 10^{-3}$. The Young's modulus of the solid material is normalized to $E_1 = 1$ and $E_2 = 10^{-3}$ Pa for the weak material. The Poisson's ratio is set at $\nu = 0.3$. In the loading region, it is assumed that the boundary Γ_N is kept fixed during the whole optimization process, that is, $\phi(\Gamma_N, t) \equiv 0 \; \forall t$. Besides this, it is imposed that velocity v_n at the boundary Γ_N is null. The examples are presented in 2D under plane stress state.

The number of sample points where the stress constraint is evaluated coincides with the number of nodes in the mesh. The Lagrange multipliers vector is initialized with a vector of zeroes, and the maximum penalization

factor is limited as $c_{\max} = 10c$.

At each iteration j of the *internal loop*, a number $m \leq 32$ of the first-order scheme (4.16) updatings are performed with a time step Δt set up to $\Delta t = 0.1(\min(\Delta x)/\max|v_n|)$. The number m may be less than 32 once the descent condition in step 3 of the *internal loop* is satisfied. The value of Δt may also be reduced if the objective function is not decreasing.

To reinitialize the level set function while approximately preserving the zero-level contour, the following partial differential equation (PDE) is solved [27, 39]:

$$\frac{\partial \phi}{\partial t} + S(\phi)(\|\nabla \phi\| - 1) = 0, \tag{4.19}$$

where

$$S(\phi) = \frac{\phi}{\sqrt{\phi^2 + \|\nabla \phi\|^2 (\Delta x)^2}}$$

is a sign function. The solution of (4.19) is a signed distance function[1]. In the examples in the succeeding text, the level set function was reinitialized every four updating steps.

The extension/regularization treatment for v_n described in Section 4.2.2 was used in the numerical examples. A smoothing-regularization parameter of $\kappa = 4(\Delta x)^2$, and penalization factor for the perimeter regularization of $\gamma = 0.01$, are used for all of the examples in this chapter. In all converging diagrams, each iteration corresponds to a normal velocity v_{nj} calculation, that is, to an iteration of the *internal loop*.

A relevant operational issue is related to the boundary conditions of ϕ. Since the level set function gradient has been included into the objective function and thus providing a perimeter penalization, the algorithm "prefers" designs attached to the boundaries. This observation was also reported in [4]. As a suggestion to avoid this preference, the value of ϕ of those nodes attached to the boundary $\partial D \backslash (\Gamma_D \cup \Gamma_N)$ whose associated elements have unitary density is set to $\phi = -\varepsilon$, where ε is a small value. In this chapter ε was set to 10^{-3}.

The numerical tests presented in next sections were executed in the following conditions[2]:

[1] A first-order upwind scheme is used to solve the reinitialization (4.19).

[2] This choice has historical reasons. The compliance term and the inclusion/exclusion of the second term of (3.42) are features of the formulation that were not originally considered in the first studies with the Hamilton-Jacobi evolution equation. When the reaction-diffusion approach was tested (described in the next chapter), these terms arise as a consequence and were included

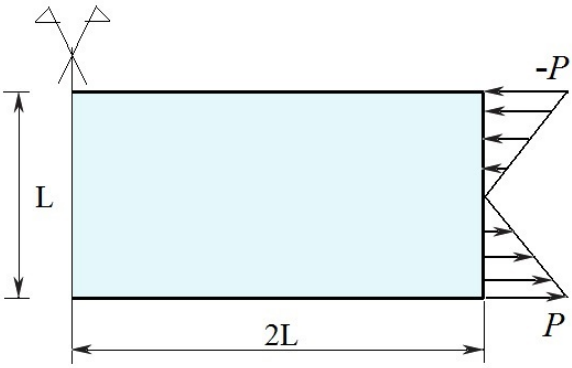

Figure 4.3: Beam problem.

a) the compliance term was not included, that is, $\mu = 0$, and
b) the penalization exponent was considered as $p = 1$. As a consequence, the second term of the right side of equation (3.42) defining velocity V is always present regardless if the point is inside or outside the material region.

4.4.1 Beam problem

The first example deals with a pure bending of a beam. Domain D is the rectangle shown in Figure 4.3 with $L = 1$ m. A pure moment is applied with a convenient pressure distribution with maximum value of $P = 30$ Pa varying linearly from the axis of the beam. The yield stress is $\sigma_{adm} = 35$ Pa. Considering symmetry, a mesh of 80×40 is used for half the structure. The initial level set is shown in Figure 4.4.

The following parameters were used: $q = 0.5$ for the exponent in (3.22) and penalization factor $c = 0.08$, updating $\beta = 1.2$. The optimization procedure was stopped after 19 external iterations considering a number of iterations $N_{iter} = 10$ for the internal optimization loop (therefore, the total of $19 \times 10 = 190$ iterations).

The final result is displayed in Figure 4.5 where an I-like profile was achieved, similar to that obtained in [1]. The mass ratio (final mass/total

in the corresponding numerical evaluations.

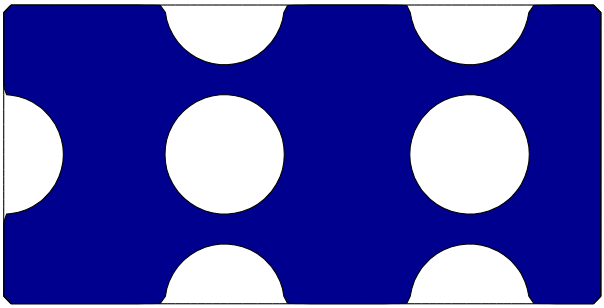

Figure 4.4: Beam problem: initial level set domain.

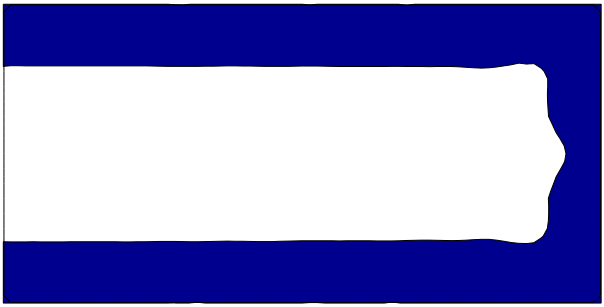

Figure 4.5: Beam problem: optimal structure with mass ratio=0.4628.

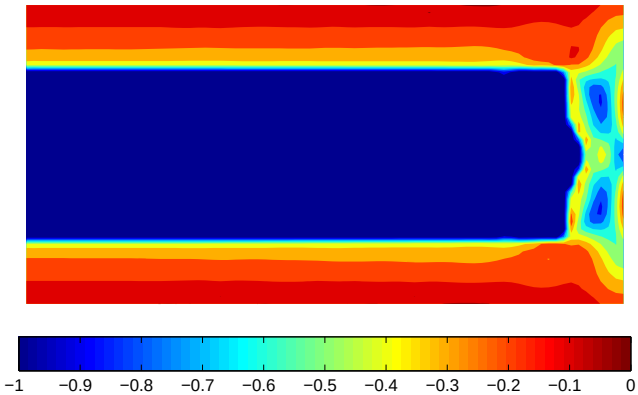

Figure 4.6: Beam problem: stress constraint distribution ($\max_D(g_r) = 6.2 \times 10^{-3}$).

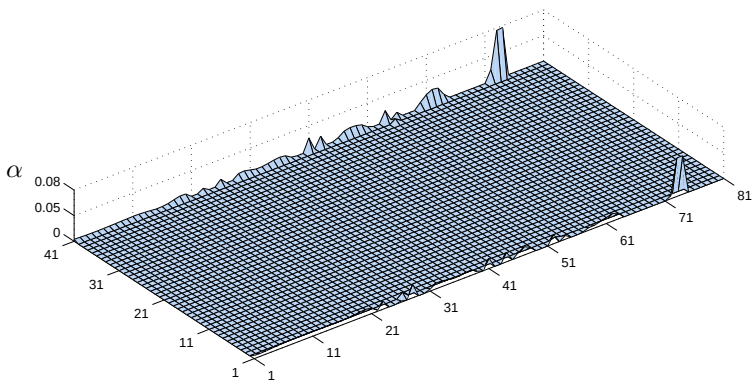

Figure 4.7: Beam problem: distribution of the Lagrange multipliers at each node in the last iteration.

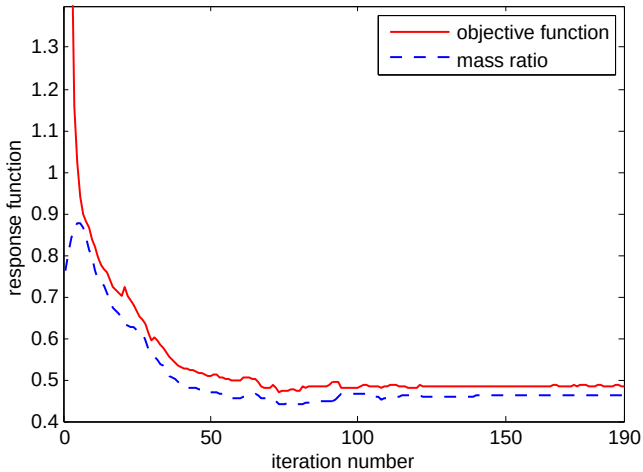

Figure 4.8: Beam problem: convergence of the objective function and mass ratio.

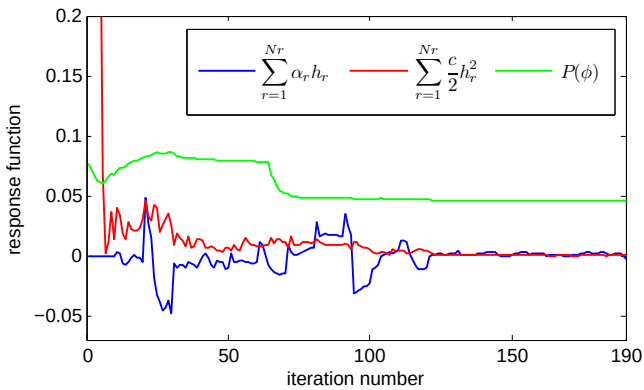

Figure 4.9: Beam problem: convergence of the penalty terms of the objective function.

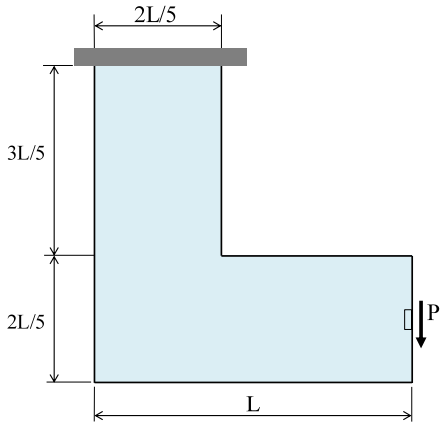

Figure 4.10: L-problem: model.

mass) is 0.4628 in the optimal structure. In Figure 4.6 is shown the distribution of (nodal) stress constraints. As expected, in the inner part of the horizontal bars, the stress constraint function is inactive, being close to zero on the external regions. The maximum value achieved for the constraints is $\max_D(g_r) = 6.2 \times 10^{-3}$, which means a small violation. This correlates to the distribution of the Lagrange multiplier values at the nodes shown in Figure 4.7. Note that most of them have zero value except those nodes of constraint activation. In addition, the distribution is quite regular, suggesting a good behavior of the algorithm. The history of the objective function is seen in Figure 4.8. Figure 4.9 shows the linear and quadratic contributions of the stress penalization terms (Equation (3.24)) converging to zero as expected and the convergence history of the perimeter constraint $P(\phi)$.

4.4.2 L-problem

This example is the classic benchmark problem of topology optimization considering stress constraints. Figure 4.10 shows the model clamped at its top boundary and submitted to a resultant force $P = 1$ N applied at the middle of the right side. The length is $L = 1$ m, and the yield stress $\sigma_{adm} = 42$ Pa.

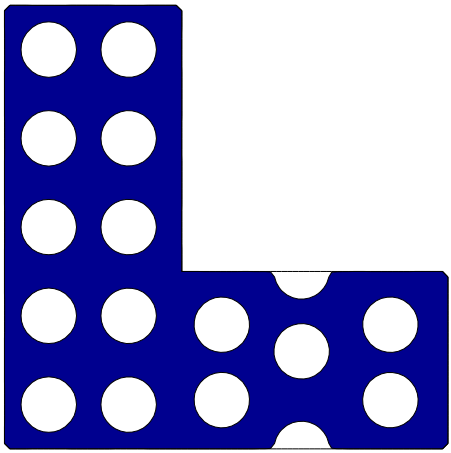

Figure 4.11: L-problem: initial level set domain for Figure 4.12 to 4.15.

Domain D was discretized with 80 elements along the longest sides in both horizontal and vertical directions giving a total of $4,096$ quadrilateral finite elements and $4,257$ nodes. Therefore, there exist $N_r = 4,257$ sample points for the stress evaluation. The optimization was run using the following parameters: $c = 0.15$ and $\beta = 1.2$. The exponent q was tested for the following values: $q = 0.25$, $q = 0.5$, $q = 0.75$, and $q = 1$. From the initial level set domain in Figure 4.11, the corresponding final designs and the constraint distribution for each of the four cases are shown in Figure 4.12-4.15. From the final mass ratio of each case, it is possible to see that the smaller the value of q, the more robust the design. This is consistent with the proposed constraint expression in which the stress of points localized near the boundary (even outside of it) are progressively considered as q decreases. It must be observed that in all cases **including the case $q = 1$, that is, no enhancement**, the reentrant corner with high stress concentration is eliminated with a well-defined arch. It is important to emphasize that among the four cases run the maximum value of the stress constraint is $\max_D(g_r) = 5.1 \times 10^{-3}$.

The convergence history of the objective function for $q = 0.5$ is shown in Figure 4.16. In this case, the minimization was stopped after 17 updates of the external loop and $N_{iter} = 20$ fixed iterations for each subproblem (internal loop), giving a total of 340 iterations. Figure 4.17 shows the convergence of

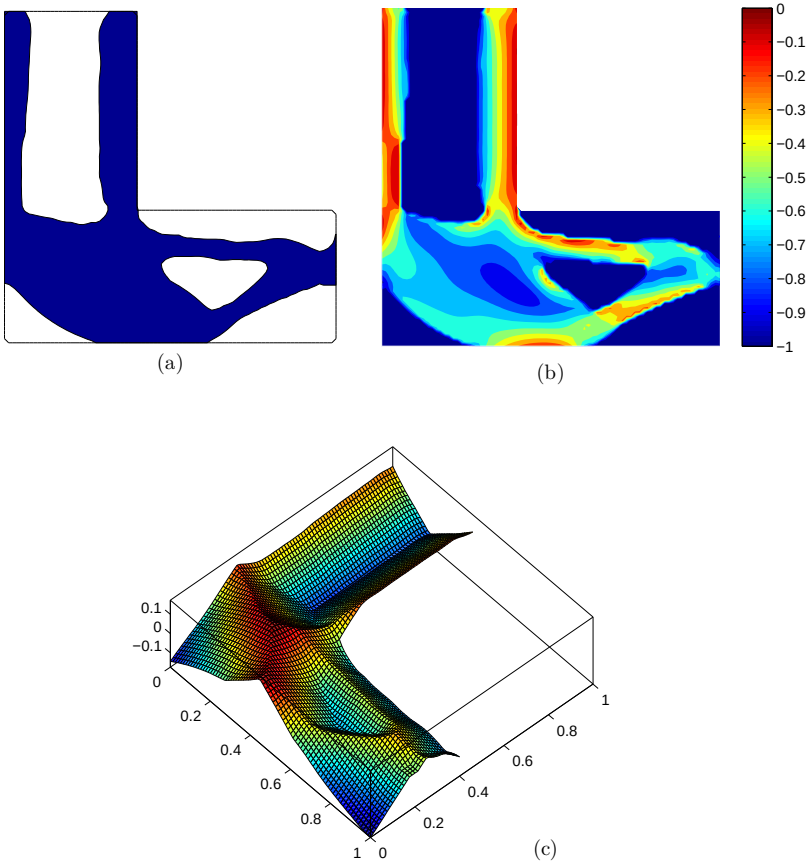

Figure 4.12: L-problem: (a) optimal structure; (b) stress constraint distribution for $q = 0.25$; and (c) level set surface of the optimal structure. The mass ratio is 0.5437 and $\max_D(g_r) = 3.5 \times 10^{-3}$.

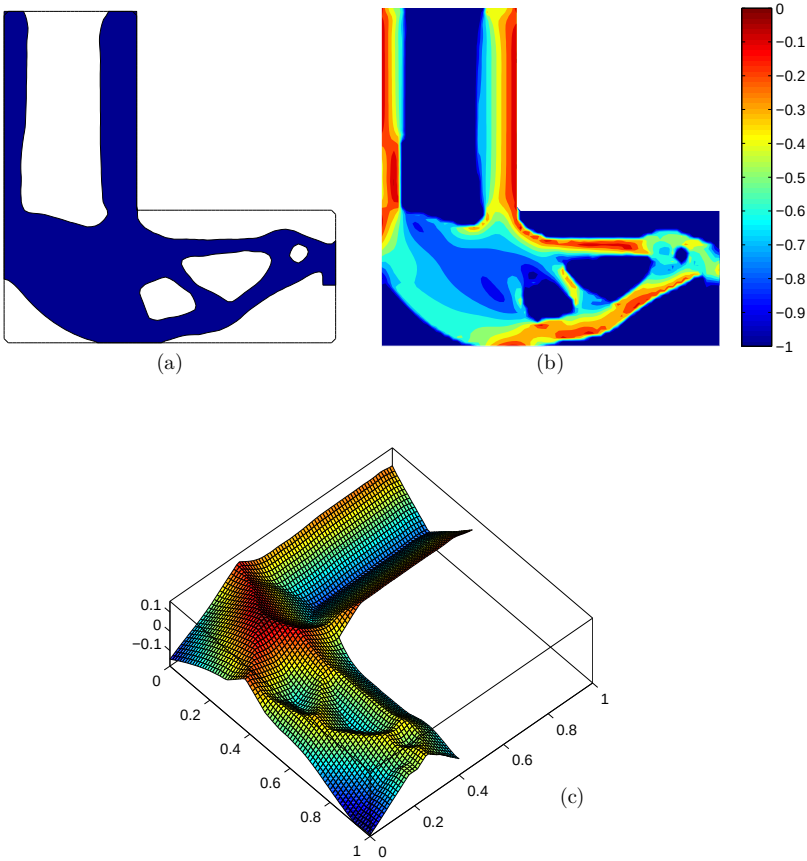

Figure 4.13: L-problem: (a) optimal structure; (b) stress constraint distribution for $q = 0.5$; and (c) level set surface of the optimal structure. The mass ratio is 0.5099 and $\max_D(g_r) = 2.3 \times 10^{-3}$.

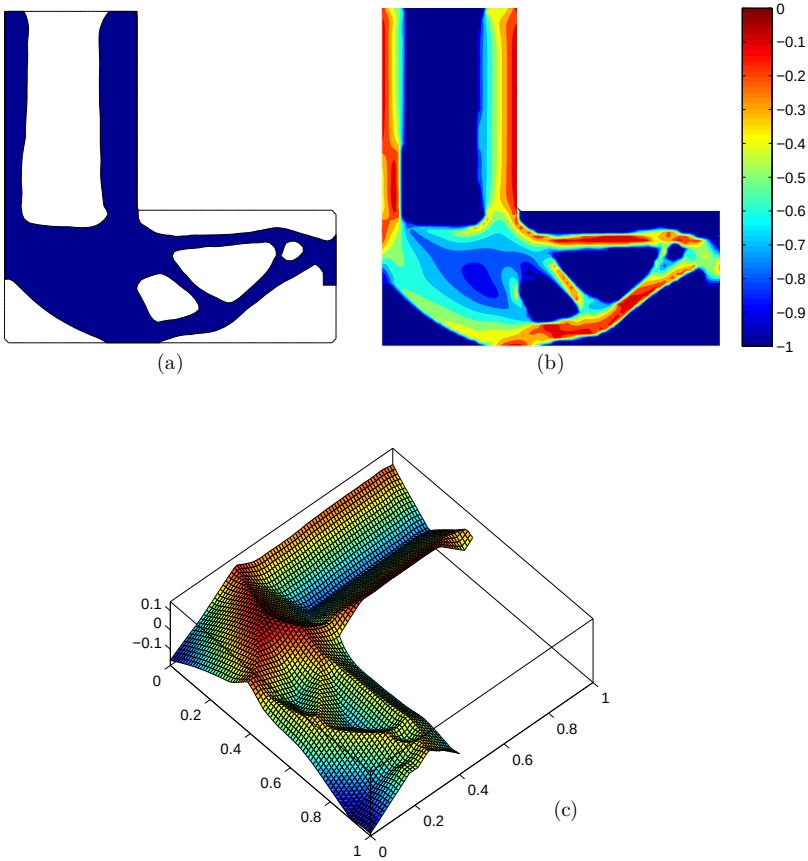

Figure 4.14: L-problem: (a) optimal structure; (b) stress constraint distribution for $q = 0.75$; and (c) level set surface of the optimal structure. The mass ratio is 0.4802 and $\max_D(g_r) = 5.1 \times 10^{-3}$.

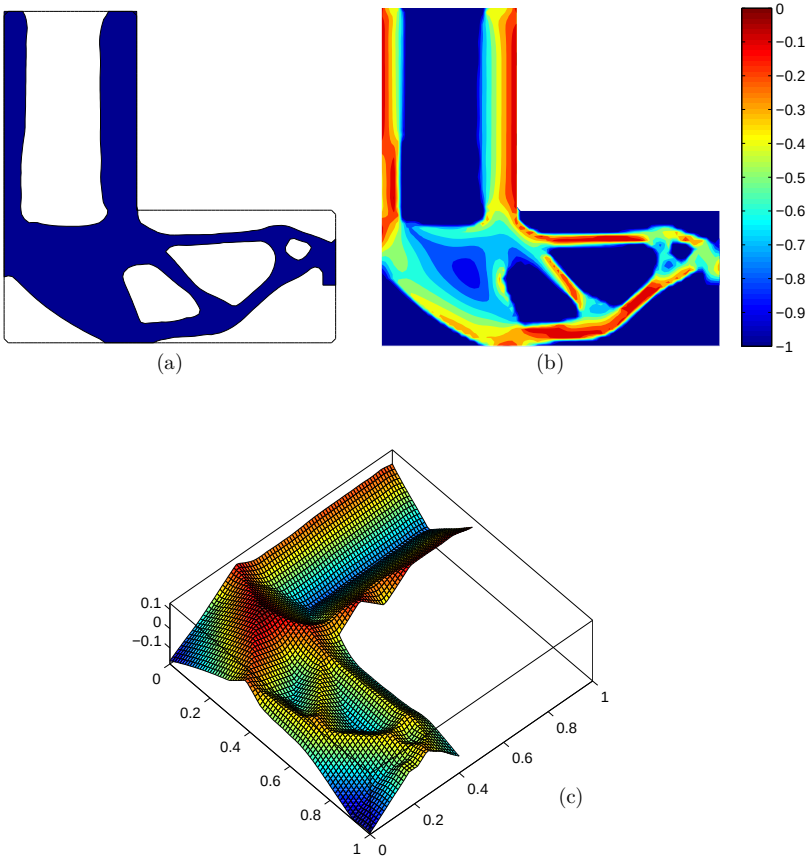

Figure 4.15: L-problem: (a) optimal structure; (b) stress constraint distribution for $q = 1$; and (c) level set surface of the optimal structure. The mass ratio is 0.4598 and $\max_D(g_r) = 2.1 \times 10^{-3}$.

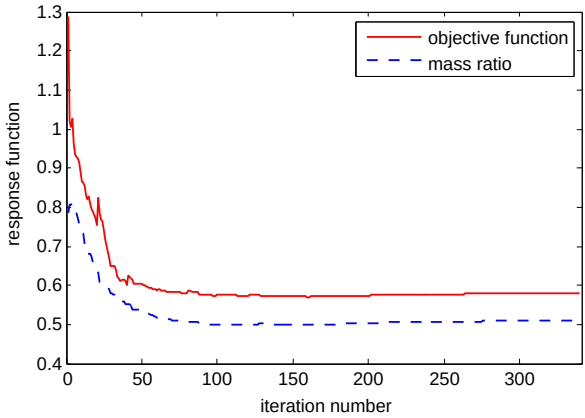

Figure 4.16: L-problem: convergence of the objective function and mass ratio for $q = 0.5$.

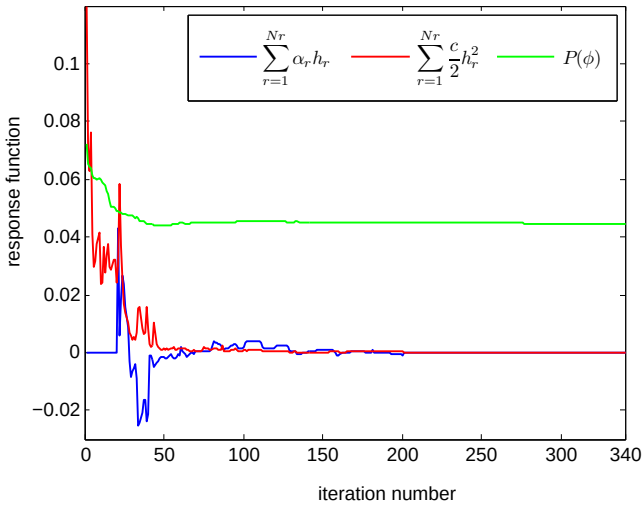

Figure 4.17: L-problem: convergence of the penalty terms of the objective function for $q = 0.5$.

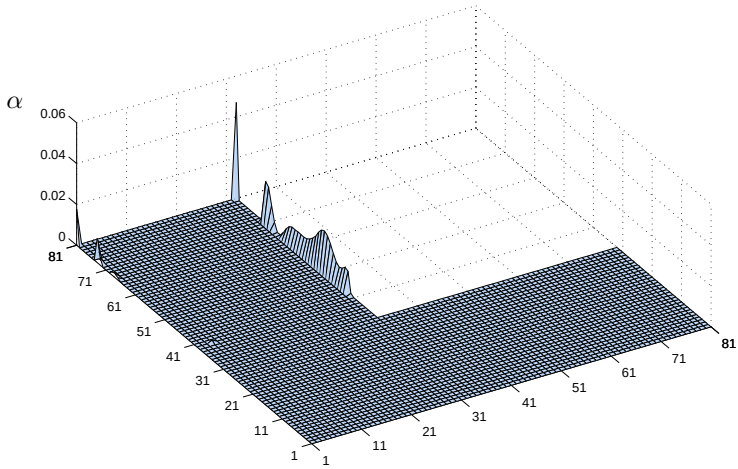

Figure 4.18: L-problem: distribution of the Lagrange multipliers at each node in the last iteration for the case where $q = 0.5$.

the penalty terms of the objective function (both figures for $q = 0.5$). The distribution of the Lagrange multipliers is shown in Figure 4.18.

A characterıstic of the level set method is the dependence of the final design in relation to the initialization. Figures 4.19 and 4.20 show different initializations. To improve convergence, the penalization factor values were modified to $c = 0.1$ and $c = 0.18$, respectively. It was used $q = 0.5$ for both examples. The optimal structures obtained at the end of the optimization process satisfy the constraints imposed in the problem. The layouts are quite different from the previously obtained; however, the rounding radius of the corner shows that the stress concentration has been detected and eliminated.

Finally, two mesh sizes were compared. The first one is that used in the previous cases, while the second has 160 elements along the longest sides in both horizontal and vertical directions, totaling $16,384$ quadrilateral finite elements and $16,705$ nodes. Figure 4.21 shows the results obtained.

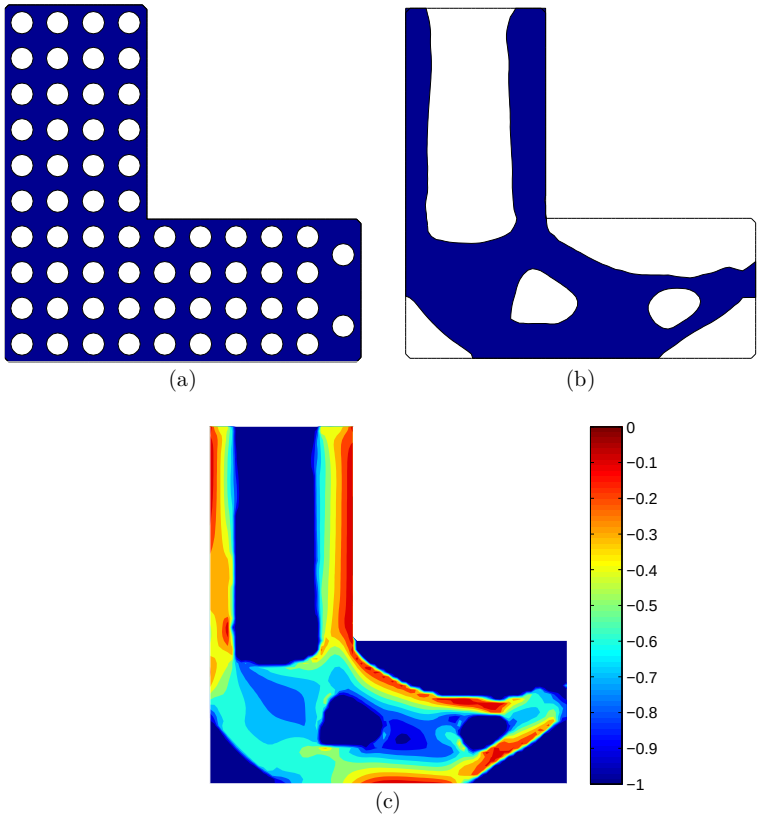

Figure 4.19: L-problem: (a) initial level set domain; (b) obtained design for $q = 0.5$; and (c) stress constraint distribution with $\max_D(g_r) = 5.6 \times 10^{-3}$. The mass ratio is 0.5066.

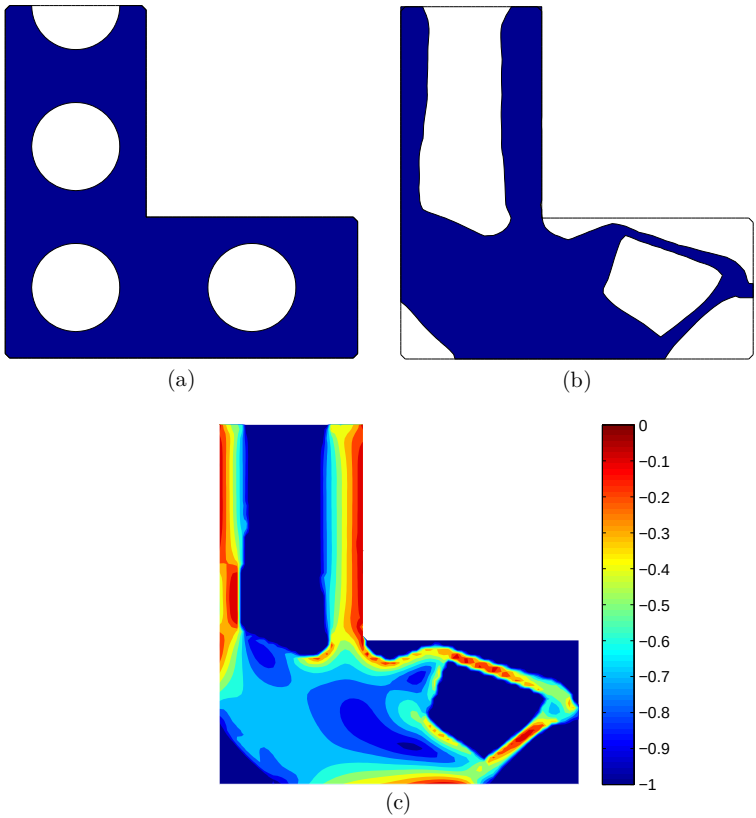

Figure 4.20: L-problem: (a) initial level set domain; (b) obtained design for $q = 0.5$; and (c) stress constraint distribution with $\max_D(g_r) = 1.7 \times 10^{-3}$. The mass ratio is 0.5630.

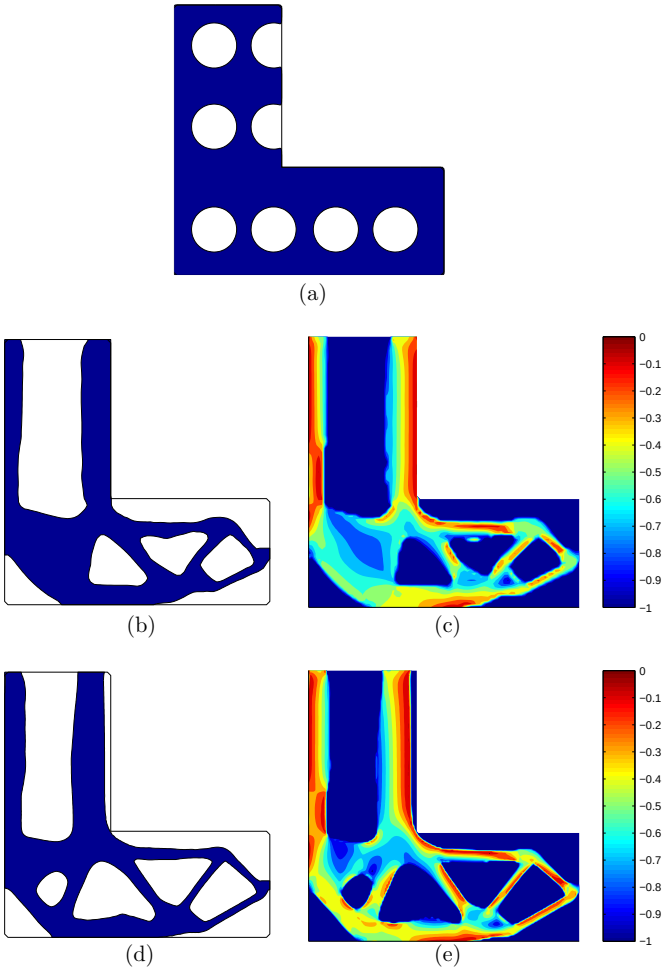

Figure 4.21: L-problem: results for different meshes and $q = 0.5$; (a) initial level set domain; (b) final design for coarse mesh (mass ratio = 0.4791); (c) stress constraints distribution for coarse mesh ($\max_D(g_r) = 3.2 \times 10^{-3}$); (d) final design for refined mesh (mass ratio = 0.4623); and (e) stress constraints distribution for refined mesh ($\max_D(g_r) = 4.0 \times 10^{-3}$).

4.4.3 Crack problem

This example emulates the fracture mode I of a squared plate of length $L = 1$ m and fracture length $L/2$. A unitary force is applied to open the fracture therefore producing high stresses at the fracture tip (Figure 4.22). The main objective of this example is to verify if the proposed approach is able to achieve a feasible design and a local minimum for the mass. Only the right symmetric part of the plate was partitioned with a mesh of 100×50 elements and $5,151$ nodes (equal to the number of stress sample points). The following parameters were used: $q = 0.5$, $c = 0.3$ and $\beta = 1.2$. The yield stress is $\sigma_{adm} = 23$ Pa. The initial and final configurations are shown in Figure 4.23(a) and (b), respectively. The final design eliminates the stress singularity, and a feasible design is achieved. The distribution of the stress constraint values is shown in Figure 4.24. The convergence graphs of mass and penalization terms are shown in Figures 4.25 and 4.26. It is possible to see that the penalization terms converge to zero, as expected for a feasible design.

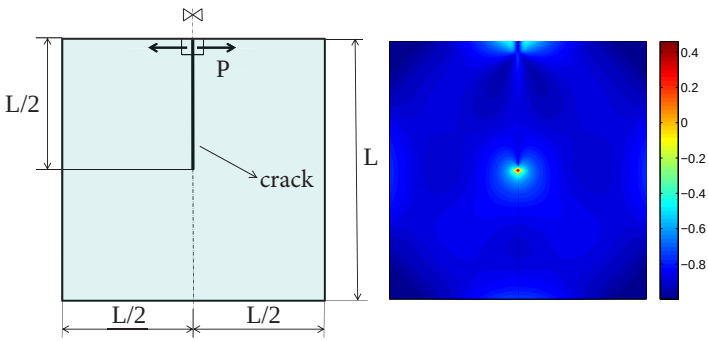

Figure 4.22: Crack problem: model and stress constraint distribution with high stress concentration at the fracture tip ($\max_D(g_r) = 0.4628$).

4.5 CONCLUDING REMARKS

A new approach combining a level set moving boundary and augmented Lagrangian technique was used to solve the structural (topological) optim-

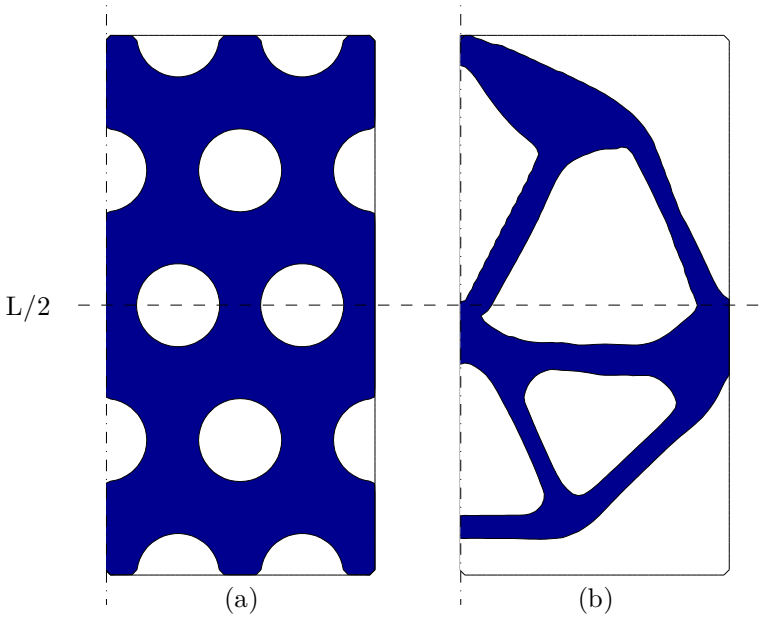

Figure 4.23: Crack problem: (a) initial level set domain and (b) optimal structure for $q = 0.5$. The mass ratio is 0.2945.

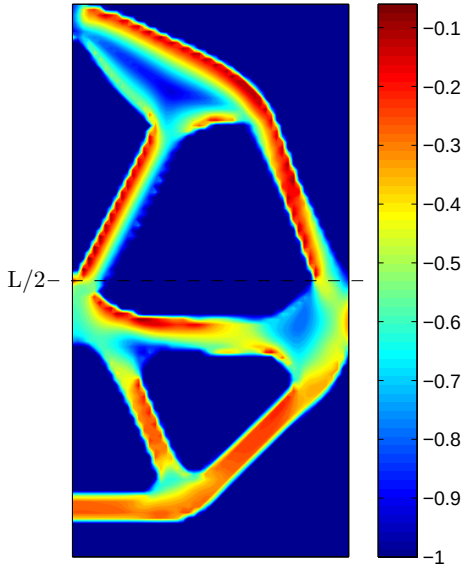

Figure 4.24: Crack problem: stress constraint distribution for $q = 0.5$ ($\max_D(g_r) = -5.04 \times 10^{-2}$).

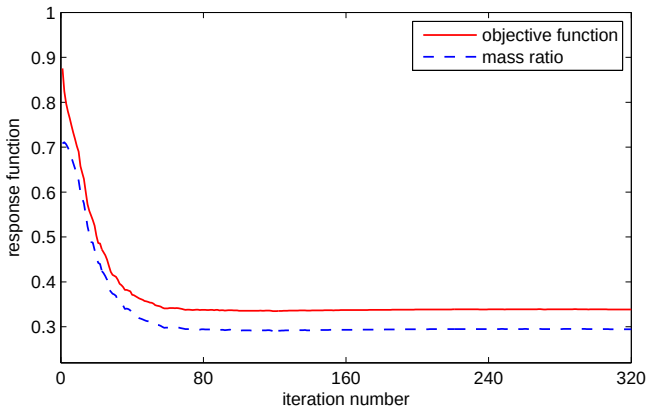

Figure 4.25: Convergence of the objective function and mass ratio for the crack problem ($q = 0.5$).

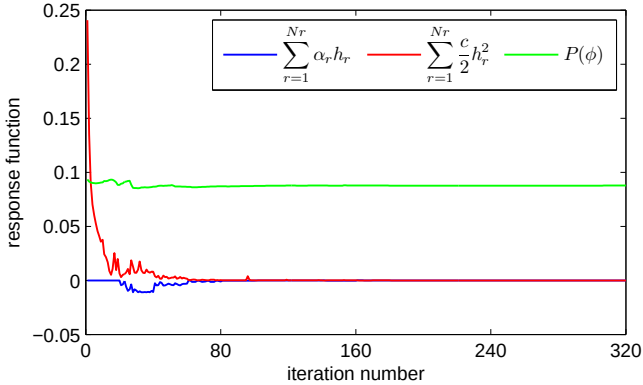

Figure 4.26: Convergence of the penalty terms of the objective function for the crack problem ($q = 0.5$).

ization problem of mass minimization under local stress constraints. The level set evolution was controlled by the classical approach based on Hamilton-Jacobi equation. Some observations should be emphasized:

1. Different values of q were tested with the L-shaped benchmark problem with successful results. Values of $q < 0.25$ reached convergence difficulties due to the almost discontinuous behavior of the stress constraints with respect to the boundary movement. However, it was observed that even in the case with no enhancement, that is, $q = 1$, the stress concentrations are identified and eliminated by rounded boundaries.

2. The conventional numerical solution of the Hamilton-Jacobi equation based on upwind schemes was used to move the boundary $\partial\Omega$ despite its well-known problems associated to the impossibility of creating new holes and the need of reinitialization [26, 25]. Reinitialization is particularly inconvenient at the end of the minimization process. At this stage, the boundary movements are usually smaller than those undesirably caused by the reinitialization technique, the fact that pollutes the solution and hinders complete convergence.

3. The velocity field v_n obtained from the sensitivity analysis showed to be a proper descent direction. However, the regularization techniques pro-

posed in Section 4.2.2 were crucial to avoid premature locking of the boundary movement. The velocity field seems to show a quite irregular distribution due to the characteristics of the adjoint solution. High stiffness ratios between material phases 1 and 2 as well as stress constraints cause peak values in the adjoint solution that are transferred to v_n. This difficulty has been overcome here by using the proposed logarithmic scaling (expression (4.10)) and the velocity extension proposed by [64] to regularize the distribution of v_n along D.

4. The classical benchmark example L-shape was tested for several initial level sets, driving to different final solutions. The important challenge of feasibility was successfully overcome in all cases. The optimization algorithm identified the stress concentration and drove to designs that eliminated undesired corners.

5 LEVEL SET EVOLUTION VIA REACTION-DIFFUSION EQUATION

5.1 INTRODUCTION

In Chapter 4 the design is modified by a level set that moves by upwind time integration of the classical Hamilton-Jacobi equation. Despite the satisfactory results obtained the creation of new holes was not allowed and the final topology is quite influenced by the initial level set domain. In addition, reinitialization techniques were needed to control the shape of the level set function during the optimization procedure. Consequently, these approaches are sometimes called not topology but shape optimization techniques.

An interesting approach proposed by Yamada and co-workers [37, 38] regularizes the optimization problem by introducing a reaction-diffusion equation for the evolution of the level set. Such proposition avoids the undesirable reinitialization procedure classically needed with Hamilton-Jacobi and also allows for the generation of new holes.

The purpose of the present chapter is to modify the level set updating procedure similarly to that proposed in [37]. Two important consequences of this choice are achieved. The first is the elimination of a reinitialization step, source of noise in the solution near convergence. The second is the possibility of creation of new holes, allowing the optimization sequence to start for different configurations, even with no holes at all.

5.2 OPTIMIZATION BY MOVING THE LEVEL SET

Many works in the literature have employed the level set equation (4.2) to the front propagation. As seen before, the conventional numerical solution of (4.2) has a well known drawback for the present application which is the need of reinitialization of ϕ after a certain number of time steps [26, 25]. This reshaping of ϕ (generally as a signed distance function) is particularly harmful at the end of the minimization process since the undesired boundary movements caused by reinitialization hinder complete convergence.

Another drawback attributed to level set minimization approaches guided by Hamilton-Jacobi evolutions is that it precludes the creation of new holes, which it is an important feature in a true topological optimization method.

In order to overcome the difficulties mentioned above, the level set

evolution technique proposed in Yamada et al. [37] will be used in the present chapter. To this aim, the objective funtion is modified by adding a regularization term[1]:

$$\min_{\phi} \quad J_R(\phi) = J(\phi) + \int_D \frac{1}{2}\tau \|\nabla\phi\|^2 dD, \tag{5.1}$$

where $J_R(\phi)$ is the regularized objective function and $\tau > 0$ is a diffusion coefficient that controls the effect of the regularization. Actually, this term works like a perimeter regularization that is commonly used to guarantee existence of solutions and to impose geometric constraints. Yamada et al. [37] relates the derivative of the cost function (5.1) to the time evolution of the level set function ϕ as follows:

$$\frac{\partial\phi}{\partial t} = -\frac{dJ_R(\phi)}{d\phi}, \tag{5.2}$$

where t is a pseudo-time variable. In this way, the evolution of ϕ will stop when the first order optimality condition of the minimization problem (5.1) is satisfied. The gradient of $J_R(\phi)$ is given by

$$\frac{dJ_R(\phi)}{d\phi} = \frac{dJ(\phi)}{d\phi} - \tau\nabla^2\phi\ . \tag{5.3}$$

Details to obtain the above expression are presented in Appendix C.

Substituting (5.3) into (5.2), the resulting time evolution equation with boundary and initial conditions is summarized as follows:

$$\begin{cases} \dfrac{\partial\phi}{\partial t} = \tau\nabla^2\phi - \dfrac{dJ(\phi)}{d\phi}, & \text{in } D \\ \phi(t=0) = \phi^0 & \text{in } D\cup\partial D \\ \dfrac{\partial\phi}{\partial\mathbf{n}} = 0, & \text{on } \partial D\backslash\partial D_N \\ \phi = 1, & \text{on } \partial D_N \end{cases} \tag{5.4}$$

The first line of (5.4) is a reaction-diffusion equation, also known as Allen-Cahn equation. The term $\tau\nabla^2\phi$ represents the diffusion while the derivative of the objective function $dJ(\phi)/d\phi$ given by Eq. (3.41) is the reaction term that accounts for the change of the shape and topology. It should be noted that boundary ∂D_N is kept fixed during the evolution of ϕ.

Furthermore, the level set function is constrained to satisfy the follow-

[1] In Yamada et al. [37] this term is called fictitious interface energy.

ing conditions:

$$\begin{aligned} -1 \leq \phi(\mathbf{x}) < 0, \quad & \forall \mathbf{x} \in D \backslash (\Omega \cup \partial\Omega) \ , \\ \phi(\mathbf{x}) = 0, \quad & \forall \mathbf{x} \in \partial\Omega \ , \\ 0 < \phi(\mathbf{x}) \leq 1, \quad & \forall \mathbf{x} \in \Omega \backslash \partial\Omega \ . \end{aligned} \tag{5.5}$$

The evolution of ϕ by means of (5.2) is strongly related to the steepest descent method. In order to justify this statement, let us consider a perturbation of ϕ in the (arbitrary) direction $\delta\phi$ to obtain the mapping

$$\phi_t = \phi + t\delta\phi. \tag{5.6}$$

Function ϕ_t defines the perturbed configuration Ω_t and $t \in \mathbb{R}^+$ represents the step size in the direction $\delta\phi$. From (5.6) and (5.2), it can be written that

$$\frac{\partial \phi_t}{\partial t} = \delta\phi = -\frac{dJ_R(\phi)}{d\phi}. \tag{5.7}$$

The derivative of $J_R(\phi)$ in the direction $\delta\phi$ provided by (5.7) is then

$$\begin{aligned} \frac{dJ_R(\phi)}{d\phi}[\delta\phi] &= \int_D \frac{dJ_R(\phi)}{d\phi}\delta\phi dD = \int_D \frac{dJ_R(\phi)}{d\phi}\left(-\frac{dJ_R(\phi)}{d\phi}\right) dD \\ &= -\int_D \left(\frac{dJ_R(\phi)}{d\phi}\right)^2 dD \leq 0. \end{aligned} \tag{5.8}$$

Thus, a Taylor expansion of the regularized objective function for a small enough $t > 0$, and being ϕ an element different from that satisfies the optimality condition, the value of J_R decreases:

$$J_R(\phi + t\delta\phi) = J_R(\phi) - t\int_D \left(\frac{dJ_R(\phi)}{d\phi}\right)^2 dD + \vartheta(t^2) < J_R(\phi). \tag{5.9}$$

This concludes that (5.4) should drive the function ϕ for a feasible local solution of the structural topology optimization problem.

5.2.1 Treatment and regularization on the reaction term (velocity field)

As shown in (5.9), the regularized objective function decreases if perturbed in a direction opposite to its gradient, given by equation (5.3), also the right-hand side of the reaction-diffusion problem (5.4). In other words, the numerical time integration of (5.4) provides finite updates of ϕ that decrease the objective function for small enough time steps. It is worth emphasizing that it is the reaction term of the gradient (5.3) who in fact contains the information for feasible topology changes, defining the velocity $V(\phi)$ in (3.41,3.42).

Borrowing analogous ideas found in mathematical programming, the updating direction $V(\phi)$, while keeping its descent properties, can be modified to improve the minimization sequence.

The first proposed modification is to extend the reaction term $dJ(\phi)/d\phi$ to the whole domain, eliminating the Dirac function in (3.41) and assuming the equality

$$\frac{dJ(\phi)}{d\phi} = V(\phi). \tag{5.10}$$

In this way, the reaction term is allowed to take any value (including zero) on D and consequently to generate changes in the level set function that lead to nucleation of new holes in the interior of the domain.

For the same reasons pointed out in Section 4.2.2, the second proposed improvement consists of the logarithmic scaling on $V(\phi)$:

$$V_{\log}(\phi) = \begin{cases} \ln(V(\phi)+1), & \text{if } V(\phi) \geq 0, \\ -\ln(-V(\phi)+1), & \text{if } V(\phi) < 0. \end{cases} \tag{5.11}$$

The last improvement of the field $V(\phi)$ refers to determine a new velocity $\bar{V}(\phi) \in H^1(D)$ more regular than $V_{\log}(\phi)$ by solving the variational problem (4.11) or its discrete version (4.13). Finally, the velocity $\bar{V}(\phi)$ is normalized by

$$v(\phi) = C\frac{\bar{V}(\phi)}{\max(|\bar{V}(\phi)|)}, \tag{5.12}$$

where C is a weight factor. Therefore, the reaction-diffusion equation solved

is:

$$\begin{cases} \dfrac{\partial \phi}{\partial t} = \tau \nabla^2 \phi - v(\phi) & \text{in } D \\ \phi(t=0) = \phi^0 & \text{in } D \cup \partial D \\ \nabla \phi \cdot \mathbf{n} = \dfrac{\partial \phi}{\partial \mathbf{n}} = 0 & \text{on } \partial D \backslash \partial D_N \\ \phi = 1 & \text{on } \partial D_N \end{cases} \tag{5.13}$$

where $v(\phi)$ is given by (5.12).

5.3 DISCRETIZATION AND NUMERICAL IMPLEMENTATION

In this section, the optimization algorithm is presented and some implementation aspects are discussed. The state equation (3.10) and the adjoint equation (3.32) are solved by FEM. Although the proposed framework for introducing local stress constraints could be used in 2D and 3D problems, only 2D numerical examples under plane stress state were tested at the present stage. A single mesh is used to discretize the level set function and to the analysis of finite elements, which uses a quadrilateral bilinear element.

The approximation of the material area fraction within each element was computed using the code available in [58], where an exact Heaviside function is used to relate the level set function to element densities.

In the present implementation the same choices of Section 4.3.2 were made for the stress sample points $\mathbf{x}_r$, making them coincide with the nodes of the finite element mesh.

5.3.1 Implicit scheme-based finite element (FE) method

To solve the system of time evolutionary equation (5.13), a scheme similar to [37] and [38] is employed. The Allen-Cahn equation is discretized in the time direction using finite diferences as follows:

$$\frac{\phi^{t+1}}{\Delta t} - \tau \, \nabla^2 \phi^{t+1} = -v(\phi^t) + \frac{\phi^t}{\Delta t} \tag{5.14}$$

where Δt is the time increment. Transferring the above equation to a weak form and assuming the boundary conditions imposed in (5.13), expression

(5.14) can be written as

$$\int_D \frac{\phi^{t+1}}{\Delta t}\,\delta\phi\;dD + \int_D \tau\,\nabla\phi^{t+1}\cdot\nabla\delta\phi\;dD = \int_D \left(\frac{\phi^t}{\Delta t} - v(\phi^t)\right)\delta\phi\;dD \quad \forall\delta\phi \tag{5.15}$$

where $\delta\phi$ is any test function. Next, discretizing (5.15) using FEM, the discretized evolution equation is given by:

$$\begin{cases} \left(\dfrac{1}{\Delta t}\mathbf{T}_1 + \tau\,\mathbf{T}_2\right)\mathbf{\Phi}^{t+1} = \mathbf{T}_1\left(\dfrac{1}{\Delta t}\mathbf{\Phi}^t - \mathbf{V}\right), & \text{in } D \\ \phi(t) = 1, & \text{on } \partial D_N, \end{cases} \tag{5.16}$$

where $\mathbf{V}$ is the velocity array (discrete version of $v(\phi)$), and $\mathbf{T}_1$ and $\mathbf{T}_2$ are given by Eq. (4.14) and (4.15), respectively. Thus, the updated level set field $\mathbf{\Phi}^{t+1}$ can be obtained by solving Eq. (5.16).

As already pointed out, the evolution of the level set function based on the numerical solution of the Hamilton-Jacobi equation has the known drawback of degrading the smoothness of $\mathbf{\Phi}$ and forcing its reinitialization using a signed distance function. Note that the explicit first order upwind scheme to solve the Hamilton-Jacobi equation uses the numerical approximation of $\nabla\mathbf{\Phi}$ demanding good quality of this function near the boundaries. The present approach, on the other hand, has two advantages on this issue. Firstly, it incorporates a useful diffusion (regularization) operator $\tau\mathbf{T}_2$ in and secondly, no approximate derivatives of $\mathbf{\Phi}$ are needed within the algorithm. Despite these observations, a sensitivity analysis on the value of the updating $\mathbf{\Phi}_{t+1}$ to the different possible treatments of the array $\mathbf{V}$ (section 5.2.1) is still lacking.

5.3.2 Optimization algorithm

It was shown in the previous sections that the minimization problem P_4 is solved by the pseudo-time evolution problem (5.13) or corresponding discrete version (5.16). The optimization algorithm used in present chapter follows the same concepts of the algorithm presented in Section 4.3.1. The *external loop* is identical, but the *internal loop* presents some particularities and it will be rewritten below.

Internal loop: for $j = 1$ *to* $j \leq N_{iter}$:

1. Obtain the discretized fields $\mathbf{u}_j$, solution of (3.25), and $\boldsymbol{\lambda}_j$, solution of (3.32).

2. Compute the field $v_j(\mathbf{u}_j, \boldsymbol{\lambda}_j)$ based on Eq. (5.12).

3. Update ϕ using (5.16) choosing Δt_j such that $J_R(\phi_{j+1}) \leq J_R(\phi_j)$.

4. If $\left|J_R(\phi_{j+1}) - J_R(\phi_j)\right| \leq \varepsilon$, then stop the iterative process; otherwise continue.

5. $j = j+1$. Go to step 1.

5.4 NUMERICAL RESULTS

Several numerical tests were performed to explore the features of the proposed optimization scheme. All the examples use the following parameters: densities $\rho_1 = 1$ and $\rho_2 = 10^{-3}$, Young's modulus $E_1 = 1$ and $E_2 = 10^{-3}$ and Poisson's ratio $\nu = 0.3$. The exponent q that enhances the stress at a sample point takes the value $q = 0.5$. The Lagrange multipliers vector $\boldsymbol{\alpha}$ is initialized with a vector of zeroes and updated as the rule (see expression $(3.28)_1$). The number of sample points N_r coincide with the number of nodes in the mesh. Moreover, the value of compliance $W(\phi)$ of the structure (given in graphs and tables) is defined as

$$W(\phi) = \int_D \mathbf{C}(\phi)\boldsymbol{\varepsilon}(\mathbf{u}) \cdot \boldsymbol{\varepsilon}(\mathbf{u}) dD. \tag{5.17}$$

With respect to N_{iter}, it is chosen $N_{iter} = 20$ fixed iterations for the internal optimization loop in most cases, unless indicated otherwise. In the convergence diagrams, each iteration corresponds to a single solution of the evolution equation (5.16), and the mass ratio is referred to as the ratio between the final mass and total mass. After some numerical tests regarding efficiency, it was chosen a convenient time step of $\Delta t \leq 0.25$. It is worth mentioning that diferently from the Hamilton-Jacobi evolution procedure where due to the CFL condition many time increments Δt were needed, the present updating was performed with a single Δt time step. Numerical experiments showed that, for the tested mesh sizes, the latter approach performed faster despite the need of an additional equation-system solution at every iteration.

To avoid the preference of designs attached to the boundaries the value of ϕ of those nodes attached to the boundary $\partial D \backslash (\Gamma_D \cup \Gamma_N)$ whose associated elements have unitary density is set to $\phi = -10^{-3}$. Regarding the smoothing-regularization parameter κ, in numerical practice it assumes values between 1-2 times $(\Delta x)^2$.

Differently from previous numerical results, the compliance term of the objective function is now considered in the objective function (that is, $\mu \neq 0$). Also, the penalization exponent is assumed as $p > 1$. As a consequence, the Heaviside function is always present in the second term of the right side of (3.42) and thus it controls the inclusion/exclusion of this term, depending on whether the point is inside or outside the material region. In numerical practice, the usage of an exponent $p > 1$ allows that the "islands" of material (or as written in [48], the pathological structures with small stiffness) from the design space that arise during the optimization process are eliminated.

5.4.1 L-problem

The benchmark example of Fig. 4.10 is tested now using the reaction-diffusion evolution. As before, $P = 1$ N, $L = 1$ m and the yield stress $\sigma_{adm} = 42$ Pa. Domain D was discretized with 160 elements along the longest sides in both horizontal and vertical directions giving a total of $16,384$ quadrilateral finite elements and $16,705$ nodes. Therefore, there exist $N_r = 16,705$ sample points for the stress evaluation. The optimization was run using the following parameters: $c = 0.15$ ($c_{\max} = 30c$), $\beta = 1.1$, $\mu = 0.0015$, $C = 0.25$, $p = 1.001$, $\kappa = 2(\Delta x)^2$ and $\tau = 7 \times 10^{-6}$. The optimization procedure was stopped after 60 updates of external loop (therefore, a total of $60 \times 20 = 1,200$ iterations), though in some cases the convergence has been reached with less iterations.

Figure 5.1(a) shows the initial level set domain and Fig. 5.1(b)-(i) show the intermediate results during the optimization process. The final design and its stress constraint distribution are presented in Fig. 5.2(a) and (b), respectively. Figure 5.3 shows the level set function corresponding to the final design bounded between -1 and 1 according to its definition (5.5). Figure 5.4 represents the convergence history for the mass ratio, the compliance $W(\phi)$ and the regularization term. It must be noted that the compliance value shown in Fig. 5.4 is not multiplied by the scale factor $\mu/2$.

Now, the algorithm is run using the same parameters but starting from a solid initial configuration (no holes) as shown in Fig. 5.5. In the minimization sequence it is observed that the optimization algorithm identifies and eliminates firstly the stress concentration in the corner, after which it begins to nucleate holes in the design domain. The final design and its respective stress constraint function is shown in Fig. 5.6(a) and (b), respectively. The graphics for the convergence of the mass ratio, the compliance $W(\phi)$ and the regularization term are shown in Fig. 5.6(c), (d) and (e), respectively. The

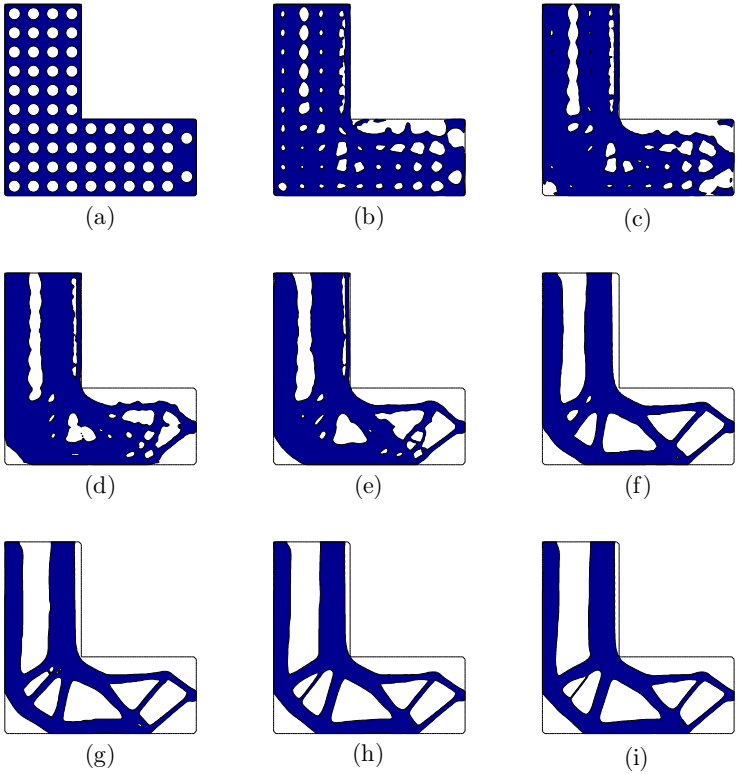

Figure 5.1: L-problem: (a) initial level set domain; Intermediate results at: (b) iteration 5; (c) iteration 10; (d) iteration 20; (e) iteration 50; (f) iteration 100; (g) iteration 150; (h) iteration 600; and (i) iteration 1000.

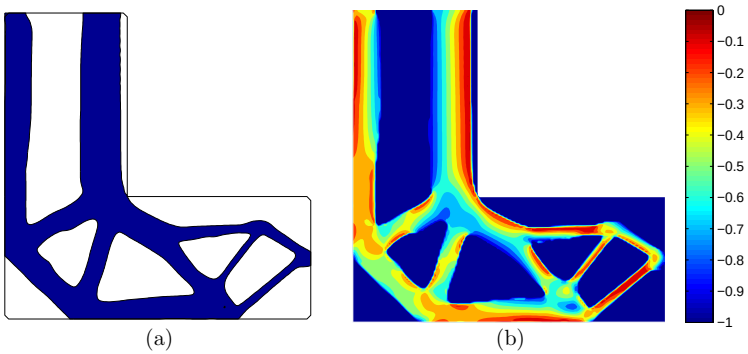

Figure 5.2: L-problem: (a) final design at iteration 1200; and (b) stress constraint distribution with $\max_D(g_r) = 6.1 \times 10^{-3}$. The mass ratio is 0.4643.

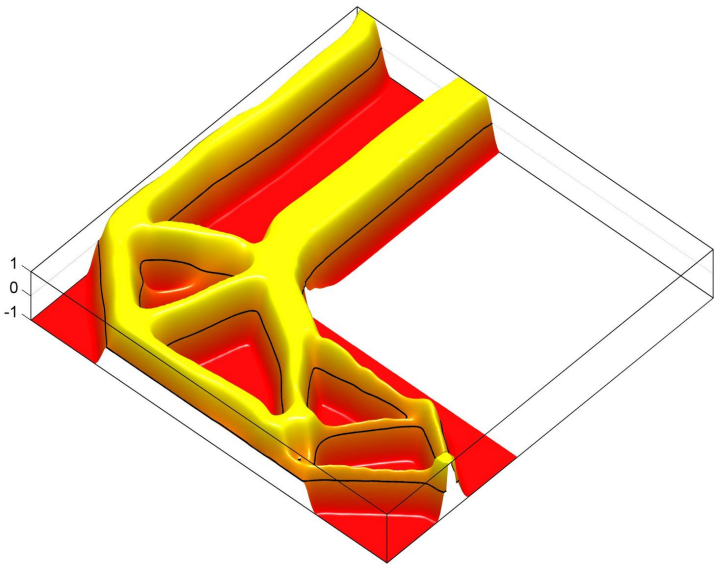

Figure 5.3: L-problem: level set function of the final design.

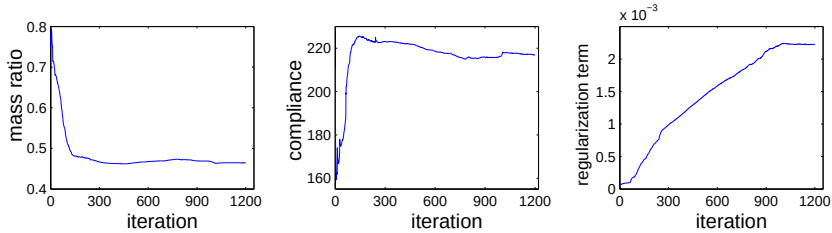

Figure 5.4: L-problem: convergence history for the mass ratio, the compliance and the regularization term.

stable behavior of the optimization process can be verified in Fig. 5.7. In this figure it is observed the penalty terms (linear and quadratic) of the stress penalization terms (Eq. (3.24)) converging to zero as expected. Also, for the objective function is shown the convergence for each iteration and for each update of the Lagrange multipliers (external loop). Note that the oscillations observed in the graph of objective function versus iterations are mostly due to the augmented Lagrangian actualization steps, where each of the stress Lagrange multipliers are updated.

Finally, the effect of the regularization parameter τ is analysed. In order to verify the capability of the optimization algorithm provides a local feasible solution for arbitrary initializations (that is, with or without holes), the initial level set function is changed again (see Fig. 5.8(a)). Three cases were tested where τ is set to 5×10^{-5}, 1×10^{-5} and 7×10^{-6}, respectively. The corresponding final designs and the constraint distribution for each of the three cases are shown in Fig. 5.8. Table 5.1 summarizes the indicators of the final mass ratio, the compliance $W(\phi)$ and the maximum value of the stress constraint ($\max_D(g_r)$) for each final design obtained in this example.

It is worth noting that all optimal structures obtained at the end of the optimization process satisfy the constraints imposed on the problem in a reasonable way. Also, the final designs can be very different depending on the initial configuration. However, the stress concentration has been detected and eliminated by a rounding radius in the corner.

An analysis of the stress state of an optimal design could be useful to a deeper understanding of the problem at hand. Let us consider the case shown in Fig. 5.6. The first issue to be highlighted is that the optimal feasible design is quite robust with few bars, occurrence possible related to the regulariza-

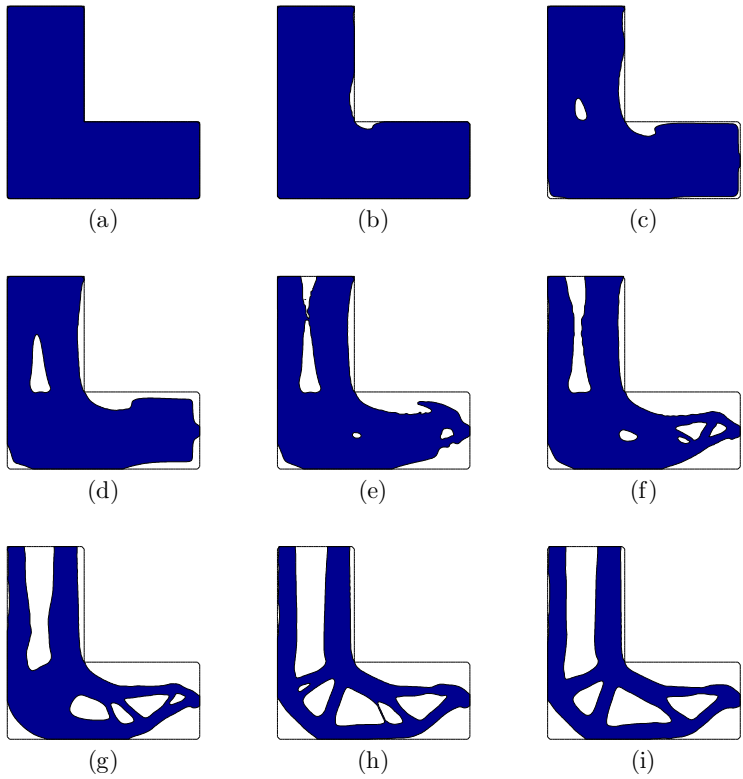

Figure 5.5: L-problem: (a) initial level set domain; Intermediate results at: (b) iteration 40; (c) iteration 80; (d) iteration 110; (e) iteration 120; (f) iteration 140; (g) iteration 200; (h) iteration 600; and (i) iteration 1000.

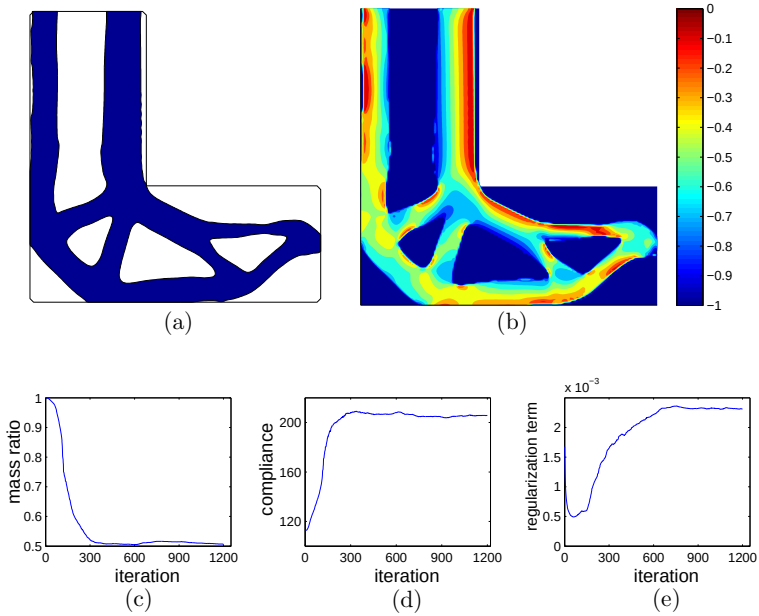

Figure 5.6: L-problem: (a) final design at iteration 1200; (b) stress constraint distribution with $\max_D(g_r) = 6.8 \times 10^{-5}$; (c) convergence history for the mass ratio (final mass ratio is 0.5066); (d) compliance convergence (final compliance value is 205.78); and (e) regularization term.

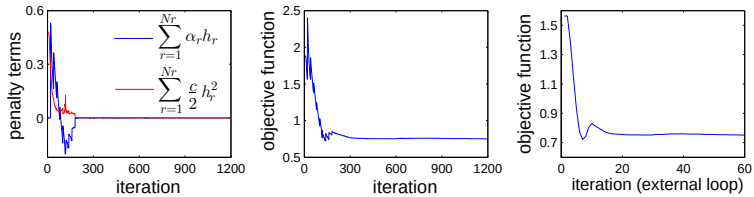

Figure 5.7: L-problem: convergence history for the penalty terms and the objective function. For the objective function, it is shown the convergence for each iteration and for each update of the Lagrange multipliers (external loop).

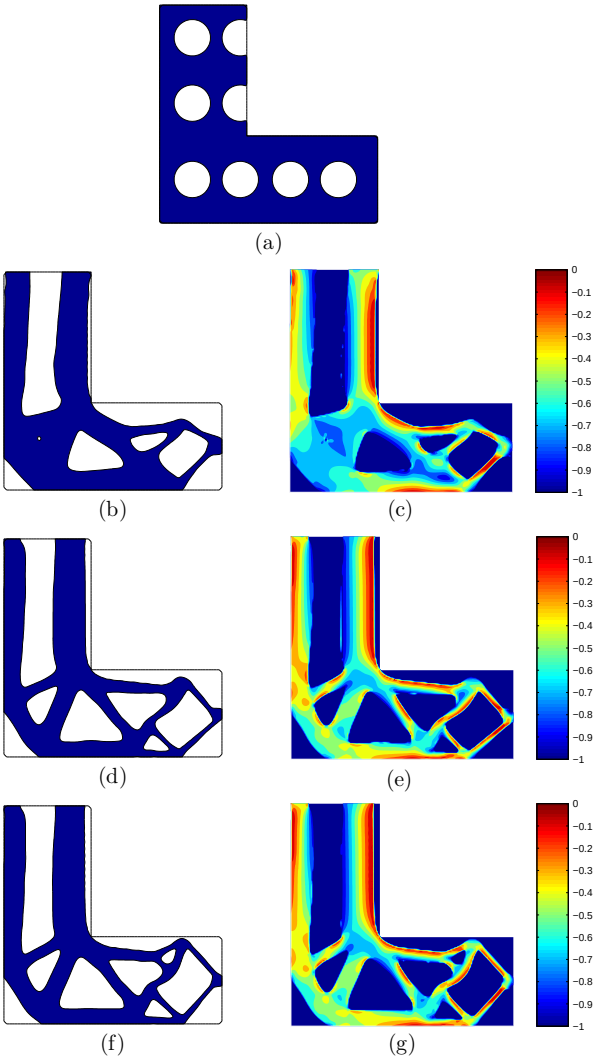

Figure 5.8: L-problem: (a) initial level set domain; (b) obtained design for $\tau = 5 \times 10^{-5}$; (c) stress constraint distribution of **b**; (d) obtained design for $\tau = 1 \times 10^{-5}$; (e) stress constraint distribution of **d**; (f) obtained design for $\tau = 7 \times 10^{-6}$; and (g) stress constraint distribution of **f**.

Table 5.1: L-problem: Summary of results for the obtained final designs

Final design	τ	mass ratio	$W(\phi)$	$\max_D(g_r)$
Fig. 5.2(a)	7×10^{-5}	0.4643	216.91	6.1×10^{-3}
Fig. 5.6(a)	7×10^{-6}	0.5066	205.78	6.8×10^{-5}
Fig. 5.8(b)	5×10^{-5}	0.5894	185.36	1.5×10^{-3}
Fig. 5.8(d)	1×10^{-5}	0.5124	210.53	3.7×10^{-3}
Fig. 5.8(f)	7×10^{-5}	0.5130	212.92	7.1×10^{-4}

tion terms included within the formulation. Secondly, these few structural members are submitted not only to axial efforts but also to bending. This is clearly seen on the failure stress distribution where a stress gradient is found along the cross section of the members. This final design and stress distribution is closely comparable to that obtained in e.g. Figure 13 of [1] where a similar approach to handle local stresses but a SIMP approach was used. We noted, however, that present proposition found the optimal design with a better boundary definition. Note that in the present case the "ersatz" material is contained in a narrow band of the size of a single element.

Moreover, an important issue inherent to the present problem but surprisingly not clearly highlighted in the literature, deserves a discussion. Differently from the classic compliance problem in which the design space is always non-empty no matter the amplitude of the applied loads, the present problem allows for cases with an empty design space. To exemplify this statement, let us consider the "L" case with a fixed failure stress. It is clear that for a sufficiently high value of external load, no feasible design is available within the given background domain.

5.4.2 Cantilever beam problem

This example deals with a cantilever beam problem. Domain D is a rectangle with a distributed vertical force $P = 1$ N applied at center of the right side and clamped at left side, as shown in Fig. 5.9 where $L = 1$ m. A mesh of 100×50 is used to discretize the fixed design domain, that means, $N_r = 5,151$ sample points for the stress evaluation. The yield stress is $\sigma_{adm} = 19$ Pa. The optimization was run using the following parameters: $c = 0.8$ ($c_{\max} = 10c$), $\beta = 1.1$, $\mu = 0.01$, $C = 0.25$, $p = 1.1$, $\kappa = 2(\Delta x)^2$ and $\tau = 3\times10^{-5}$.

Figure 5.10 presents the intermediate results during the optimization

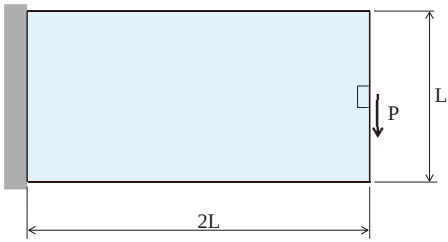

Figure 5.9: Cantilever beam problem: model.

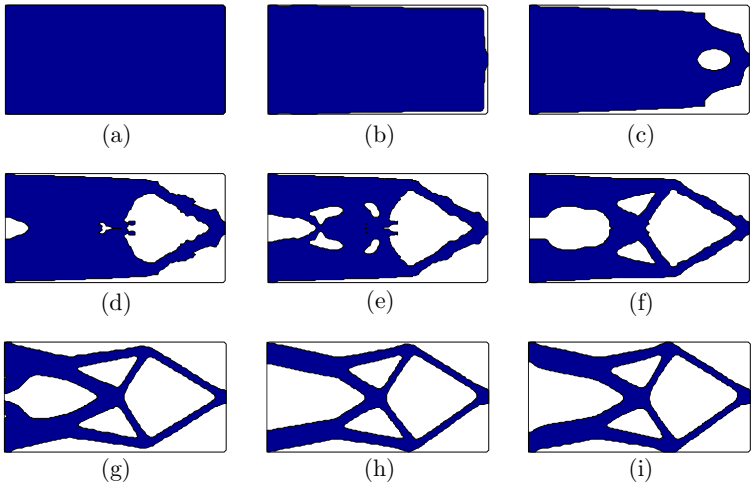

Figure 5.10: Cantilever beam problem: (a) initial level set domain; Intermediate results at: (b) iteration 40; (c) iteration 45; (d) iteration 50; (e) iteration 55; (f) iteration 60; (g) iteration 150; (h) iteration 300; and (i) iteration 400.

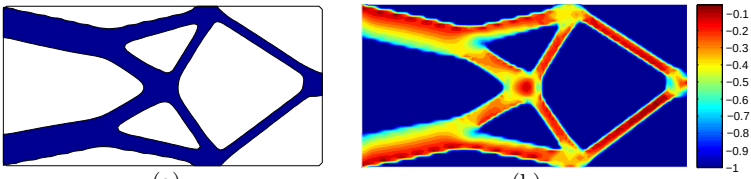

(a) (b)

Figure 5.11: Cantilever beam problem: (a) final design at iteration 600; and (b) stress constraint distribution with $\max_D(g_r) = -1.8 \times 10^{-2}$. The mass ratio is 0.3107 and the compliance value is 118.35.

process from an initial level set domain filled with solid material. After 30 external updates (external loop), the final design at iteration 600 is shown in Fig. 5.11(a). In Fig. 5.11(b) is shown the distribution of (nodal) stress constraints. The maximum value achieved for the constraints is $\max_D(g_r) = -1.8 \times 10^{-2}$.

Table 5.2: Cantilever beam problem: summary of the results shown in Figure 5.12.

k	μ	τ	p	mass ratio	$W(\phi)$	$\max_D(g_r)$
$2(\Delta x)^2$	0.01	3×10^{-5}	1.001	0.2937	120.49	1.46×10^{-4}
$2(\Delta x)^2$	0.01	3×10^{-5}	1.5	0.3291	112.96	4.7×10^{-3}
$2(\Delta x)^2$	0.01	3×10^{-5}	3	0.3966	96.81	1.30×10^{-3}

Next, the effect that different penalization exponent p values have upon the optimal solutions for problems with stress constraint is investigated. The initial level set function is shown in Fig. 5.12(a). Here, 26 updates of external loop and $N_{iter} = 30$ for each subproblem (internal loop) were used (therefore, a total of $26 \times 30 = 780$ iterations). The remaining parameters are unchanged. Three cases were examined where the penalization exponent p is set to 1.001, 1.5 and 3, respectively. Figure 5.12 shows the final configuration and its respective stress constraint distribution for each case. Some numerical data are reported in Table 5.2 for comparison. Higher values of p provide lower values to the compliance of the design. On the other hand, the mass ratio also increases as p increases. This fact may be explained due to the increase of consideration of the "intermediate" elements in the structure as p

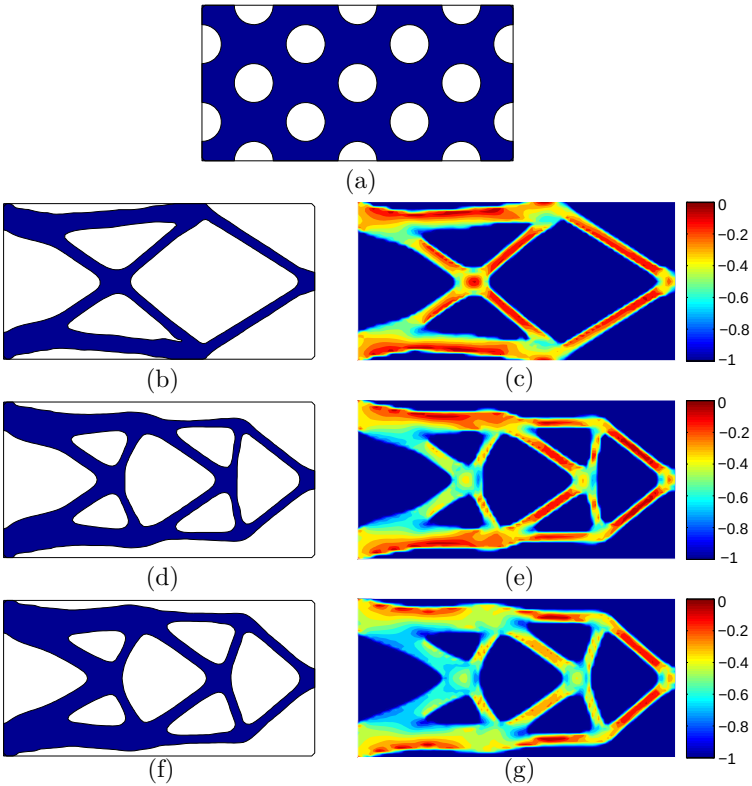

Figure 5.12: Cantilever beam problem: (a) initial level set domain; (b) final design for $p = 1.001$; (c) stress constraint distribution for $p = 1.001$; (d) final design for $p = 1.5$; (e) stress constraint distribution for $p = 1.5$; (f) final design for $p = 3$; and (g) stress constraint distribution for $p = 3$.

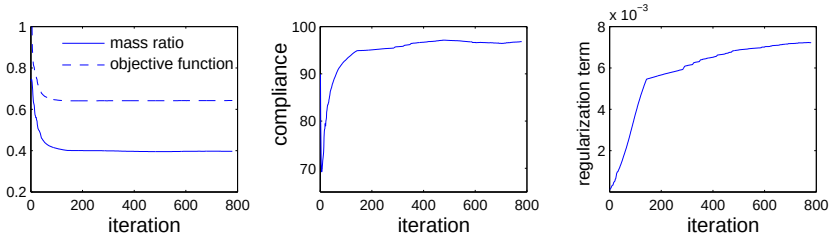

Figure 5.13: Cantilever beam problem: convergence history for the mass ratio and objective function, the compliance $W(\phi)$ and the regularization term for the final design shown in Figure 5.12(f), where $p = 3$.

increases (in the case of stress constraint problems). Figure 5.13 shows the convergence history for the mass ratio and objective function, the compliance and the regularization term for the case $p = 3$.

The cantilever beam problem is often used in the literature for topology optimization problems with compliance. The approaches developed in the present work (regularization schemes and evolution equation) were used for the compliance problem. Figure 5.14(a) shows the (typical) final design obtained with mass constraint set to 40% of the total mass. Figure 5.14(b) shows the stress constraint distribution presenting high stress concentration at the clamp. Although the final design for compliance problem has provided a lower compliance value than for stress constraint problem (see Fig. 5.14 and Table 5.2 for the case $p = 3$ that has practically the same mass ratio), it has not satisfied the more common engineering requirement, that is, support loads without failure. Moreover, the final designs are significantly different (compare Fig. 5.12(f) and Fig. 5.14).

5.4.3 Crack problem

This is the problem proposed in the previous chapter which emulates a fracture mode I. A force $P = 1$ N is applied to open the fracture and it is assumed a yield stress $\sigma_{adm} = 23$ Pa. It will be considered two models with different geometric sizes and load locations.

The first model consists of verifying the behavior of the present ap-

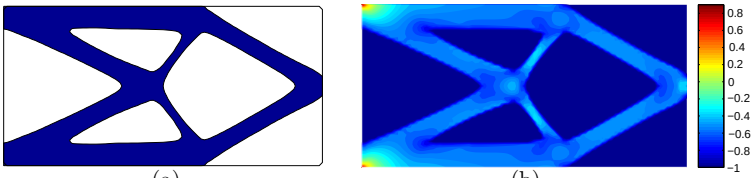

(a) (b)

Figure 5.14: Cantilever beam problem: (a) final design for the compliance problem; and (b) stress constraint distribution with $\max_D(g_r) = 0.9$. The mass constraint was set to 40% of the total mass. The compliance $W(\phi)$ of the final design is 76.8. The initial configuration has the material domain filled with material.

Table 5.3: Crack problem (model 1): parameters of the results shown in Figure 5.15.

mesh	k	τ	c	$c_{\max}$	mass ratio	$W(\phi)$	$\max_D(g_r)$
100×50	$1(\Delta x)^2$	3×10^{-5}	0.8	$10c$	0.2340	113.49	-0.0159
180×90	$2(\Delta x)^2$	1×10^{-5}	0.25	$20c$	0.2277	117.36	-0.0171

proach to the problem in Fig. 4.22. As this same model was tested in Chapter 4 (with Hamilton-Jacobi evolution), the same initial configuration will be used for comparison purposes (see Fig. 5.15a). Only the right symmetric part of the plate was discretized. Two mesh sizes were compared to verify the influence of the finite element mesh size on the final design. The first one was partitioned with a mesh of 100×50 elements and $5,151$ nodes (equal to the number of stress sample points N_r) and another one with 180×90 elements and $16,471$ nodes (equal to the number of N_r). The following parameters were used to both meshes: $\beta = 1.1$, $\mu = 0.004$, $C = 0.25$ and $p = 1.001$; the remaining parameters are shown in Table 5.3 for each mesh. The minimization was stopped after 30 updates of external loop giving a total of $30 \times 20 = 600$ iterations. Figure 5.15 shows the optimal configurations with its respective stress constraint distribution for each mesh size. It is possible to observe that the dependence on the finite element mesh size is small. To achieve this feature, the penalization factor and the parameters related to the element size were appropriately changed. In comparison to results from the previous chapter (Section 4.4.3) the designs obtained in this chapter with

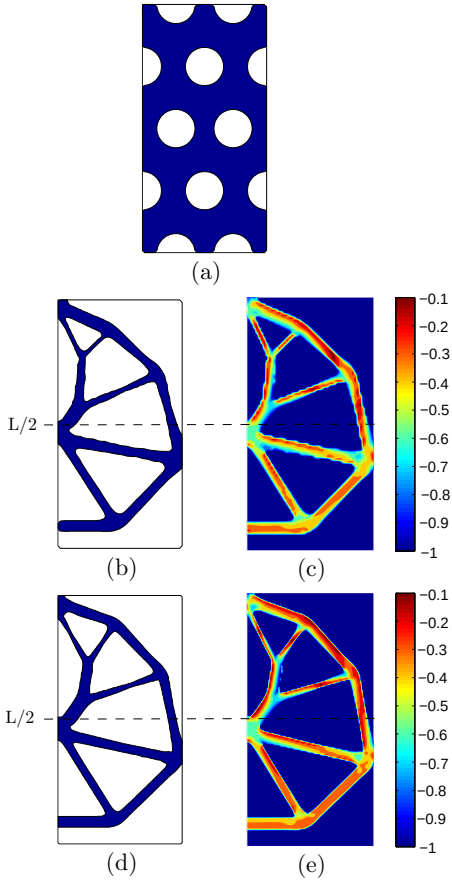

Figure 5.15: Crack problem (model 1): results for different meshes; (a) initial level set domain; (b) final design for 100×50 mesh; (c) stress constraints distribution for 100×50 mesh; (d) final design for 180×90 mesh; and (e) stress constraints distribution for 180×90 mesh.

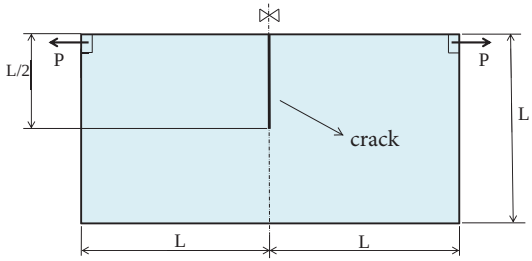

Figure 5.16: Crack problem: model 2.

a reaction-diffusion evolution are more slender, that is, they have a smaller mass ratio. This slenderness can be attributed to the possibility of nucleation holes in the minimization process which allows for a better stress distribution. The mass ratio, the compliance $W(\phi)$ and the maximum value of the stress constraint ($\max_D(g_r)$) for each mesh also are shown in Table 5.3.

The second model consist on a plate of length $2L \times L$ where $L = 1$ m and fracture length $L/2$, as shown in Fig. 5.16. Note that now the force is applied on a different location compared to model 1. Considering symmetry, a mesh of 100×100 elements is used to discretize the right half of the plate ($N_r = 10,201$). Optimization is performed for: $c = 0.8$ ($c_{\max} = 20c$), $\beta = 1.1$, $\mu = 0.004$, $C = 0.25$, $p = 1.001$, $\kappa = 1(\Delta x)^2$ and $\tau = 2 \times 10^{-5}$. The optimization algorithm was stopped after 35 updates of external loop (a total of $35 \times 20 = 700$ iterations). In this case, the optimization process was tested for two initial configurations. Figure 5.17 shows the optimal configurations as well as the distribution of the stress constraint values for each initial level set domain. Although the designs are different, the compliance and mass ratio have close values. Once again, the final design eliminates the stress singularity and a feasible design is achieved. Figure 5.18 shows the 3D level set function for the optimal designs of Fig. 5.17(b) and (e). Figure 5.19 shows the convergence history for the mass ratio and objective function, the compliance $W(\phi)$ and the regularization term for the final configuration shown in Fig. 5.17(e).

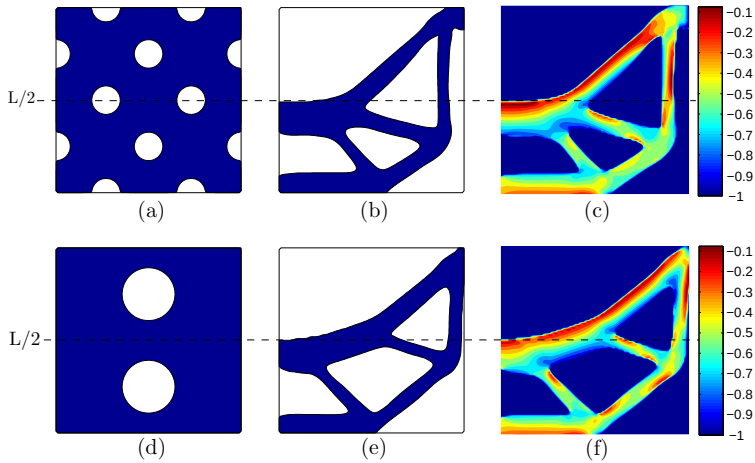

Figure 5.17: Crack problem (model 2): (a) initial configuration; (b) final design (mass ratio is 0.34 and compliance is 59.73); (c) stress constraint distribution with $\max_D(g_r) = -6.6 \times 10^{-4}$; (d) initial configuration; (e) final design (mass ratio is 0.33 and compliance is 57.16); and (f) stress constraint distribution with $\max_D(g_r) = -3.14 \times 10^{-4}$.

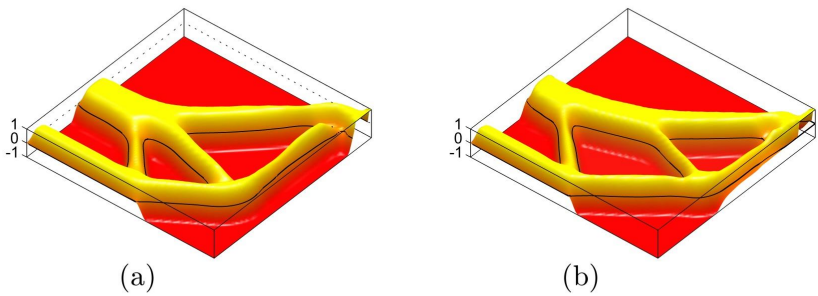

Figure 5.18: Crack problem (model 2): (a) 3D level set function for Fig. 5.17b; and (b) 3D level set function for Fig. 5.17e.

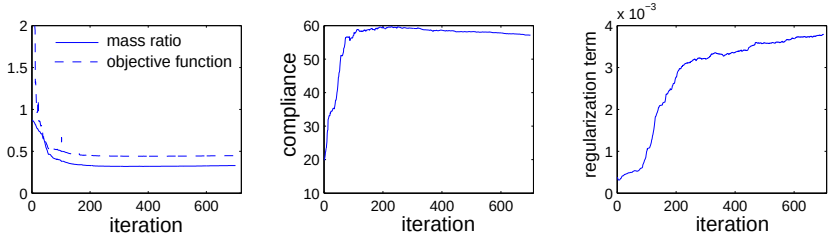

Figure 5.19: Crack problem (model 2): convergence history for the mass ratio and objective function, the compliance and the regularization term for the final configuration shown in Figure 5.17(e).

5.5 CONCLUDING REMARKS

The structural topology optimization problem of mass minimization under local stress constraints was addressed. An augmented Lagrangian technique associated with the stress constraint proposed in Chapter 3 was used to transform a minimization problem with multiple constraints into a sequence of unconstrained minimization problems. The level set evolution, differently from the classical approach based on Hamilton-Jacobi equation used in Chapter 4, was controlled by a reaction-diffusion problem as proposed in [37]. Some conclusions are highlighted:

1. The optimization algorithm was clearly successful to identify high stresses and to create minimizing sequences arriving to local optimum feasible designs.

2. Numerical experiences showed that the use of the reaction-diffusion evolutionary equation (5.13) conferred the algorithm with good numerical behavior, allowing for quite stable optimization sequences. As already pointed out, the elimination of reinitialization operations was certainly an important feature contributing to this fact. Moreover, the algorithm uses fewer parameters than those needed for Hamilton-Jacobi based evolutions.

3. Although the velocity field V is, by means of equation (3.40), meaningful on the boundary, its extension to the complete domain D was verified to turn the algorithm capable of nucleating holes in appropri-

ate regions, which in the present case are those with lower stresses and, consequently, the stress constraints are inactive. Thus, we did not observe significant oscillations in the objective function when a hole is inserted during the optimization process.

4. The reaction-diffusion equation used in this chapter was clearly inspired in that used in Yamada et al. [37] for compliance problem. Yamada et al. [37] verified that the initial level set domain has low influence on the final design. For the present stress-constrained problem, this low dependency did not occur. It is reasonable to hypothesize that this fact is due to the great number of local minima characterizing stress-constrained optimization problems. Since the proposed algorithm does not guarantee to find a global optimum, the final designs still show significant dependence on the initial configuration.

5. The velocity regularization techniques (logarithmic scaling and reaction term regularization) described in Section 5.2.1 were crucial to avoid premature locking of the boundary movement.

6 A LEVEL SET WITH A POLYGONAL FINITE ELEMENT APPROACH

6.1 INTRODUCTION

In previous chapters, the proposed approach to stress-constrained problems was discretized using uniform grids with quadrilateral elements. In Compliance-SIMP problems, it was shown in [65] that structured grids may influence the orientation of members of the structure leading to mesh-dependent sub-optimal designs. In addition, structured meshes constraint the possible geometries of the background domain, which is used to conveniently bound the design space.

In order to extend the approach to practical engineering applications, the goal of this chapter is to implement the level set-based formulation proposed in the present thesis with unstructured meshes. An option might be a mesh with triangular elements, widely used in the literature and commercial programs. Another alternative that has been adopted in recent years is to use polygonal elements.

An attractive feature of polygonal meshes is the set of geometric properties of a centroidal Voronoi Tessellation. Such properties are appropriate to use finite volume schemes in the numerical solution of the Allen-Cahn equation (5.4). The literature has registered an increasing number of works that use concepts of control volumes in the solution of structural problems [66, 67]. Moreover, unstructured polygonal meshes have shown to remove mesh bias. In view of this, it is desired to verify the behavior of the algorithm presented in Chapter 5 using polygonal finite elements[1].

6.2 POLYGONAL FINITE ELEMENTS

As mentioned above, the main objective of this chapter is to employ polygonal meshes for the numerical implementation of the topology optimization procedure proposed in Chapter 5. To this end, *PolyMesher*[2] of Talischi et al. [68] is employed to generate the polygonal mesh based on Voronoi dia-

[1]The subject of this chapter results from a collaboration work with Prof. Glaucio H. Paulino, University of Illinois at Urbana-Champaign, USA, who received the author of this thesis during a year.

[2]The code to discretize two-dimensional geometries written in Matlab is available in the article [68].

grams. In this approach, the concepts of signed distance function are used to represent the design domain. Firstly, a set of random points/seeds lying inside the domain is generated, and each seed in the domain is reflected about the closest boundary point. The Voronoi diagram is constructed for the set of random seeds and their reflections. If the Voronoi cells of a seed and its reflection have a common edge, then this edge form an approximation to the domain boundary. The collection of Voronoi cells corresponding to the random seeds represents the discretized design domain with convex polygons. In order to obtain a better quality of the mesh, the Lloyd's algorithm [69] is used to replace the initial random seeds by the centroids of the Voronoi diagram. The convergence of Lloyd's iterations produces the Centroidal Voronoi Tessellations (CVTs).

In this work, the Wachspress shape functions [70] are used for the polygonal finite elements. In the sequel the finite element scheme for convex polygons is briefly reviewed. Let $\boldsymbol{\xi}$ an interior point for a reference n-gon. The Wachspress shape function corresponding to node i, $1 \leq i \leq n$, is defined as [71]:

$$N_i(\boldsymbol{\xi}) = \frac{w_i(\boldsymbol{\xi})}{\sum_{j=1}^{n} w_j(\boldsymbol{\xi})}, \tag{6.1}$$

where w_i are the interpolants of the form:

$$w_i(\boldsymbol{\xi}) = \frac{A(\mathbf{p}_{i-1}, \mathbf{p}_i, \mathbf{p}_{i+1})}{A(\mathbf{p}_{i-1}, \mathbf{p}_i, \boldsymbol{\xi}) A(\mathbf{p}_i, \mathbf{p}_{i+1}, \boldsymbol{\xi})}. \tag{6.2}$$

Here A denotes the area of the triangle formed by its arguments (see Fig. 6.1a). As shown in Fig. 6.1(b), the nodes of the reference n-gon are located at $\mathbf{p}_i = (\cos 2\pi i/n, \sin 2\pi i/n)$. Because the n-gon is regular, $A(\mathbf{p}_{i-1}, \mathbf{p}_i, \mathbf{p}_{i+1})$ is the same for all i and thus can be factored out of expression (6.1). Thus, instead of (6.2) the formula for the interpolants can be simplified as:

$$w_i(\boldsymbol{\xi}) = \frac{1}{A(\mathbf{p}_{i-1}, \mathbf{p}_i, \boldsymbol{\xi}) A(\mathbf{p}_i, \mathbf{p}_{i+1}, \boldsymbol{\xi})}. \tag{6.3}$$

Wachspress shape functions satisfy all the desirable properties from the viewpoint of a conforming Galerkin approximation such as non-negativity, Kronecker-delta property, and partition of unity:

$$0 \leq N_i(\boldsymbol{\xi}) \leq 1, \qquad N_i(\boldsymbol{\xi}_j) = \delta_{ij}, \qquad \sum_{i=1}^{n} N_i(\boldsymbol{\xi}) = 1. \tag{6.4}$$

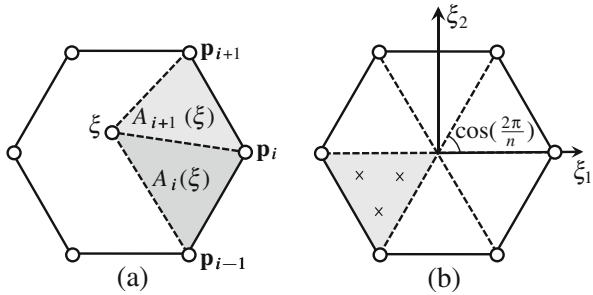

Figure 6.1: (a) Illustration of the triangular areas used to define w_i in expression (6.2). (b) Triangulation of the reference regular polygon and integration points defined on each triangle

Also, these functions are linearly precise or complete:

$$\sum_{i=1}^{n} N_i(\boldsymbol{\xi})\boldsymbol{\xi}_i = \boldsymbol{\xi} \ , \tag{6.5}$$

which indicates that a linear function is represented exactly by these shape functions. Moreover, Wachspress functions are linear along the edges of the polygon and $N_i \in C^\infty$ within the polygon [72]. When $n = 3$ and $n = 4$ the Wachspress basis recovers the usual linear and bilinear shape functions.

6.3 NUMERICAL IMPLEMENTATION

Only 2D numerical examples under plane stress state were performed in the present work. The state equation (3.10) and adjoint equation (3.32) are solved by FEM. For the numerical integration, it is employed the approach adopted in Talischi et al. [73] (*PolyTop* code): the polygonal canonical element is sub-divided into triangles and the usual quadrature rules on a triangle (three integration points) are used.

A single polygonal mesh is used to discretize the level set function and the finite elements analysis. For the approximation of the material area fraction, the (physical) polygonal finite element is divided into triangles (see

Fig. 6.2) which it is assumed that

$$\phi_c = \frac{1}{N_{node}} \sum_{i=1}^{N_{node}} \phi_i \ , \tag{6.6}$$

where ϕ_c is the value of ϕ in the centroid of the element and N_{node} is the number of nodes of the polygonal element. Thus the area fraction for each resulting triangle is calculated through code available in Dijk at al. [58], where an exact Heaviside function is used to relate the level set function to element densities.

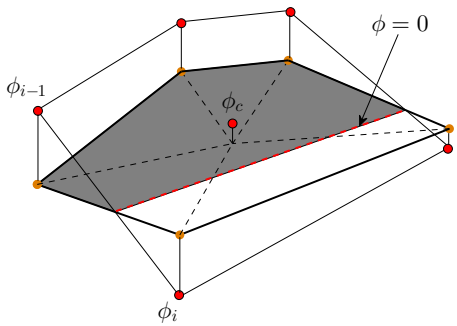

Figure 6.2: Representation of the level set function ϕ in a polygonal element, where the dark region represents the material in the element. The value of ϕ on the centroid is the average of the ϕ values at the nodes.

6.3.1 Sample points and its neighborhoods

As carried out before for structured mesh with quadrilateral elements, in the present case it is also assumed that the sample points $\mathbf{x}_r$, $r = 1...N_r$ coincide with the nodes of the polygonal finite element mesh. This distribution of sample points is consistent with the objective of enforcing the stress constraint all over the domain, following the resolution of the stress field provided by the finite element mesh. The corresponding neighborhoods Ω_r are defined from centroids of the neighbor elements around each node (or sample point), as shown in Fig. 6.3. The black lines represent the polygonal mesh and the

blue lines are the neighborhoods (that is, the dual of the Voronoi cell). This proposed representation of sample points and its neighborhoods provide a complete covering of D. The area fraction $H_r(\phi)$ is also computed making use of the code in [58] and Eq. 6.6.

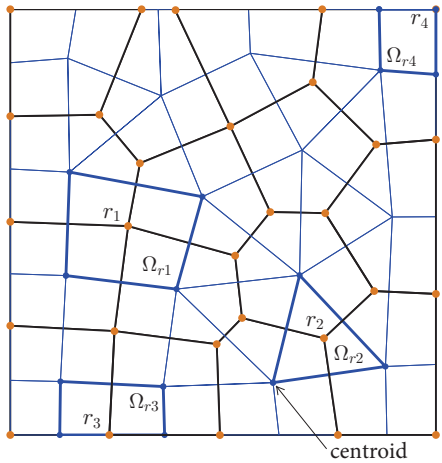

Figure 6.3: Example of sample points $\mathbf{x}_r$ (coinciding with the nodes of the polygonal finite element mesh) and its neighborhoods Ω_r defined from centroids of the elements (blue lines). The black lines correspond to the polygonal mesh.

The reaction-diffusion equation defined in Chapter 5 will be used for the level set evolution. Two approaches are employed to solve the system of time evolutionary equation (5.13) with a polygonal discretization. The first one is the implicit scheme-based finite element (FE) method proposed in Section 5.3.1. The second approach, called CVT-based finite volume method, takes advantage of geometrical properties of the polygonal elements and will be discussed in the following.

6.3.2 CVT-based finite volume (FV) method for unstructured meshes

This is a popular method of choice for solving PDEs when dealing with unstructured grids (see, for example, [74, 67]). In this work, a scheme similar to that proposed in [75] will be used to solve the Eq. $(5.13)_1$. The approach utilizes the geometrical properties of a polygonal mesh based on centroidal Voronoi tessellation (CVT).

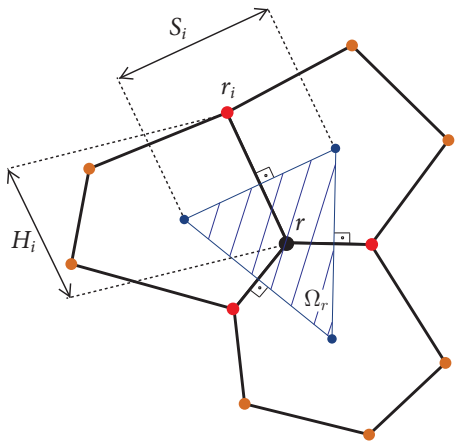

Figure 6.4: Illustration of the CVT-based finite volume scheme. The parameter S_i represents the distance between the centroids of the common elements to the nodes r and r_i, and H_i denotes the distance between the nodes r and r_i.

Consider the polygonal mesh of Fig. 6.4. The figure shows the geometrical properties for each neighborhood Ω_r. Consider a node r and let the set of nodes $\mathscr{R} = \{r_1, r_2, ...r_n\}$ be its natural neighbors (for example, in Fig. 6.4 the nodes in red are the natural neighbors of r). The integral form of $(5.13)_1$, over time t and on each neghborhood Ω_r, can be expressed as:

$$\int_{t,\Omega_r} \frac{\partial \phi}{\partial t} dt d\Omega = \int_{t,\Omega_r} \tau \operatorname{div}(\nabla \phi) dt d\Omega - \int_{t,\Omega_r} v(\phi) dt d\Omega \,, \tag{6.7}$$

or, using the Divergence Theorem, as

$$\int_{t,\Omega_r} \frac{\partial \phi}{\partial t} dt d\Omega = \int_{t,\Gamma_r} \tau \nabla \phi \cdot \mathbf{n} dt d\Gamma - \int_{t,\Omega_r} v(\phi) dt d\Omega \ . \tag{6.8}$$

Based on Fig. 6.4, each term in (6.8) can be integrated as

- First term:

$$\int_{t,\Omega_r} \frac{\partial \phi}{\partial t} dt d\Omega = \int_{\Omega_r} (\phi^{t+1} - \phi^t) d\Omega \approx (\phi_r^{t+1} - \phi_r^t) a_r \ , \tag{6.9}$$

  where ϕ_r^t is the value of ϕ at the node r at time t and a_r is the area of the control volume. Note that the control volume corresponds to the neighborhood Ω_r.

- Second term:

$$\begin{aligned} \int_{t,\Gamma_r} \tau \nabla \phi \cdot \mathbf{n} dt d\Gamma &\approx \int_t \sum_{\mathscr{R}} \left[\tau \nabla \phi^t \cdot \mathbf{n}\, S \right]_i dt \\ &= \left(\sum_{\mathscr{R}} \left[\left(\tau \frac{\partial \phi^t}{\partial \mathbf{n}} \right)_{r,r_i} S_i \right] \right) \Delta t = P_0(\phi^t) \ , \end{aligned} \tag{6.10}$$

  where S_i represents the distance between the centroids of the common elements to the nodes r and r_i. The directional derivative $(\partial \phi^t / \partial \mathbf{n})_{r,r_i}$ can be calculated taking advantage of the local orthogonality property of Voronoi cell:

$$\left(\frac{\partial \phi^t}{\partial \mathbf{n}} \right)_{r,r_i} = \frac{\phi_{r_i}^t - \phi_r^t}{H_i} \ , \tag{6.11}$$

  where H_i is the distance between nodes r and r_i.

- Third term:

$$\int_{t,\Omega_r} v(\phi) dt d\Omega \approx a_r \Delta t \, v(\phi_r^t) \ . \tag{6.12}$$

Substituting (6.9), (6.10) and (6.12) in (6.8), the semi-implicit FV updating scheme for ϕ in (5.13) can thus be expressed as:

$$\phi_r^{t+1} = \phi_r^t + \frac{1}{a_r} P_0(\phi^t) - \Delta t \, v(\phi_r^t) \ . \tag{6.13}$$

The expression (6.13) provides the update value of ϕ at each node.

6.3.3 Sample points stress evaluation

It is assumed that the strain at a node i, namely $\boldsymbol{\varepsilon}(i)$, is the average of the strains at the integration points ip closer the corresponding node (see Fig. 6.5):

$$\boldsymbol{\varepsilon}(i) = \frac{1}{2}\left(\boldsymbol{\varepsilon}_{ip1} + \boldsymbol{\varepsilon}_{ip2}\right) \ , \tag{6.14}$$

$$\boldsymbol{\varepsilon}_{ip1} = \mathbf{B}_e(ip1)\mathbf{U}_e, \quad \boldsymbol{\varepsilon}_{ip2} = \mathbf{B}_e(ip2)\mathbf{U}_e \ , \tag{6.15}$$

where $\mathbf{B}_e(ip)$ is the array of Wachspress shape function gradients (see Appendix D) evaluated at ip, and $\mathbf{U}_e$ is the array of nodal displacements of element e.

To determine $\boldsymbol{\varepsilon}_r(\mathbf{x}_r)$ which represents the strain of a sample point r, it is simply taken the average

$$\boldsymbol{\varepsilon}_r(\mathbf{x}_r) = \frac{1}{N_e}\sum_{e=1}^{N_e}\boldsymbol{\varepsilon}_e(i) \ , \tag{6.16}$$

where N_e is the number of elements e attached to node $\mathbf{x}_r$, and $\boldsymbol{\varepsilon}_e(i)$ is the strain at a node i (located at $\mathbf{x}_r$) to the element e calculated by (6.14). The stress at this node is then computed by (3.18) and the stress constraint by (3.21).

6.4 NUMERICAL RESULTS

The minimization sequence adopted in this chapter follows the optimization algorithm of Section 5.3.2. The effectiveness of the algorithm with a polygonal discretization will be demonstrated in this section by means of numerical tests. The examples use the following parameters: densities $\rho_1 = 1$ and $\rho_2 = 10^{-3}$, Young's modulus $E_1 = 1$ and $E_2 = 10^{-3}$, and Poisson's ratio $\nu = 0.3$. The exponent q that enhances the stress at a sample point takes the fixed value $q = 0.5$. The Lagrange multipliers vector $\boldsymbol{\alpha}$ is initialized with a vector of zeroes and updated as the rule (see expression 3.28_1). Moreover, the number of sample points N_r coincide with the number of nodes in the mesh.

For polygonal elements, in the numerical practice, the smoothing-

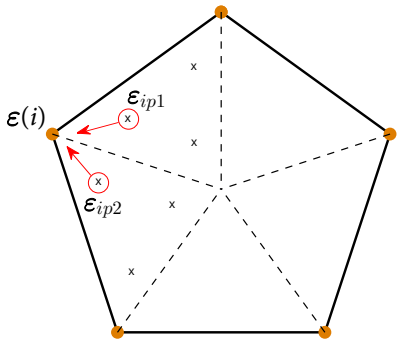

Figure 6.5: The strain field is calculated at the integration points. The strain at a node $\boldsymbol{\varepsilon}(i)$ is assumed as the average of the strains $\boldsymbol{\varepsilon}_{ip}$ closer the node.

regularization parameter κ is adopted as being

$$\kappa = a \min\left(\int_{D_e} dD\right), \quad e = 1...N_e$$

where a is a value between 0.5 to 1.

The number of iterations for the internal optimization loop is fixed $N_{iter} = 20$. In the convergence diagrams, each iteration corresponds to a single solution of the evolution equation (5.16), and the mass ratio is referred to as the ratio between the final mass and total mass.

For the same reasons pointed out in the earlier chapters, the value of ϕ of those nodes attached to the boundary $\partial D \backslash (\Gamma_D \cup \Gamma_N)$ whose associated elements have unitary density is set to $\phi = -10^{-3}$.

Concerning the choice of the numerical scheme to solve the time evolutionary equation (5.13), "FE scheme" refers in following text to the method presented in Section 5.3.1, and "FV scheme" to the method proposed in Section 6.3.2. For a given velocity (descent direction) $v(\phi)$, the Allen-Cahn equation is performed m FE/FV scheme update steps during the time (integration)

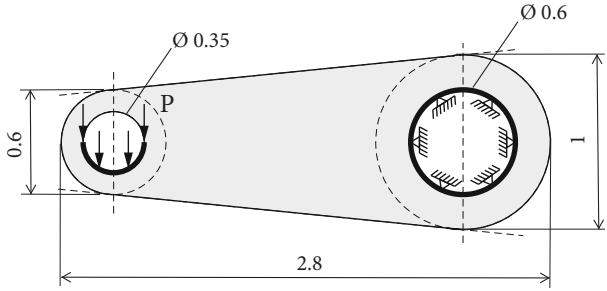

Figure 6.6: Wrench problem: model.

step $\Delta t = m\Delta t_{CFL}$ that satisfies the CFL condition, where:

$$\Delta t_{CFL} \leq \frac{\min(\sqrt{a_e})}{\max|v(\phi)|} \ .$$

The number of updatings m is conveniently chosen to satisfy a descent condition given in step 3 of the internal minimization loop.

6.4.1 Wrench problem

In this example, a non-squared background domain is considered. Figure 6.6 shows the design domain with the boundary conditions (dimension in meters). The model is clamped at the right hole and a distributed vertical force $P = 1$ N is applied at semi-circle of the left hole. A mesh of $10,000$ polygonal elements with $19,857$ nodes (or sample points) is used to discretize the fixed domain. This means that there are $19,857$ stress constraints for the problem. It is assumed $\sigma_{adm} = 18$ Pa. The optimization was run using the following parameters: $c = 0.5$ ($c_{\max} = 10c$), $\beta = 1.1$, $\mu = 0.005$, $C = 0.5$, $p = 1.001$, $a = 1$ and $\tau = 1 \times 10^{-4}$. The algorithm was stopped after 16 external updates (external loop) and, therefore, there is a total of $16 \times 20 = 320$ iterations.

From an initial level set domain filled with solid material (see Fig. 6.7), Fig. 6.8(a) and (b) present the final design and its corresponding distribution of (nodal) stress constraints, respectively, using FE scheme to update Allen-Cahn equation. On the other hand, Fig. 6.9(a) and (b) present the final design and its stress constraints, respectively, using FV scheme. Table 6.1

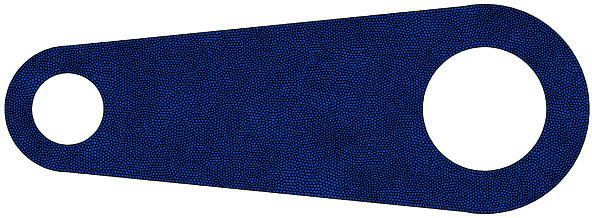

Figure 6.7: Wrench problem: Initial level set topology with 10,000 polygonal element mesh.

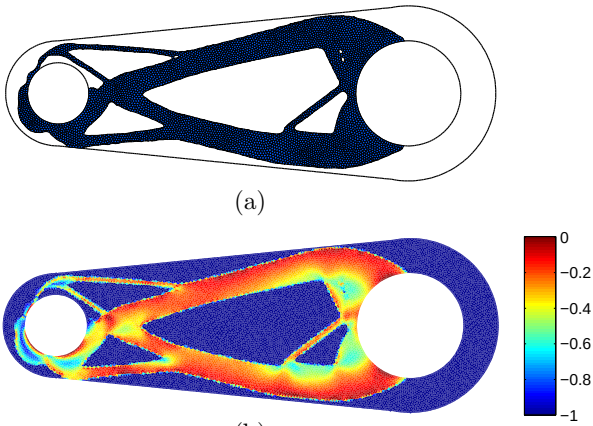

Figure 6.8: Wrench problem: (a) Final design using FE scheme; and (b) stress constraint distribution.

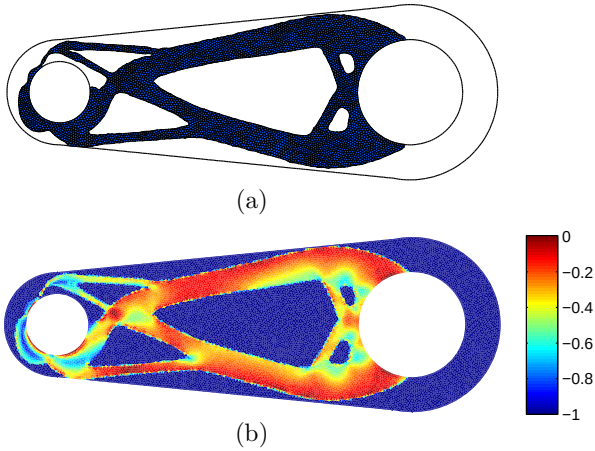

Figure 6.9: Wrench problem: (a) Final design using FV scheme; and (b) stress constraint distribution.

compares the values for the mass ratio, the minimum compliance $W(\phi)$ and the maximum value of the stress constraint ($\max_D(g_r)$) for both numerical schemes. Moreover, Fig. 6.10(a) and (b) show the objective function and the mass ratio along the optimization process for each scheme.

Table 6.1: Wrench problem: Summary of results to the final designs using FE and FV schemes.

Final Design	Scheme	Mass ratio	$W(\phi)$	$\max_D(g_r)$
Fig. 6.8(a)	FE	0.3984	121.59	3.4×10^{-3}
Fig. 6.9(a)	FV	0.4041	120.40	3.7×10^{-3}

The wrench problem was also tested for the minimum compliance problem. Figure 6.11(a) shows the final topology obtained with mass constraint set to 40% of the total mass, and Fig. 6.11(b) shows the corresponding stress constraint distribution. There are several regions where the admissible stress is exceeded (see the different colors of shades of blue in Fig. 6.11b), however, the stress concentration is more critical on the semi-circle where the load is applied. Note that the designs are quite different: for compliance, the bars of the structure are attached to the boundary, while for stress constraint

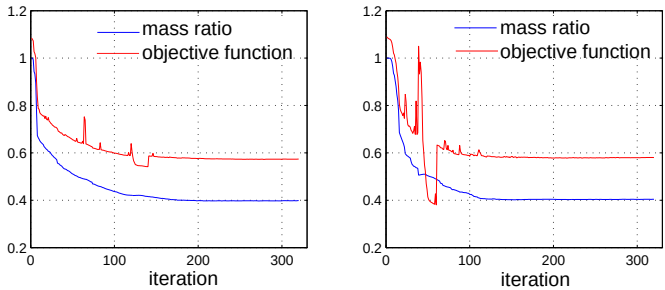

(a) FE scheme (b) FV scheme

Figure 6.10: Wrench problem: Objective function and mass ratio along the 320 iterations for (a) FE scheme and (b) FV scheme.

problem the bars are curved like pliers.

6.4.2 L-problem

Now the benchmark example of Fig. 4.10 is tested with a polygonal framework. As before, $P = 1$ N, $L = 1$ m and the yield stress $\sigma_{adm} = 42$ Pa. Domain D was discretized with $10,000$ polygonal elements and $19,885$ nodes (that is, $N_r = 19,885$ sample points for the stress evaluation). The following parameters were taken to the optimization algorithm: $c = 0.15$ ($c_{\max} = 30c$), $\beta = 1.1$, $\mu = 0.0015$, $C = 0.5$, $p = 1.001$, $a = 0.5$ and $\tau = 7 \times 10^{-6}$. The optimization procedure was stopped after 40 updates of the external loop (a total of $40 \times 20 = 800$ iterations).

Table 6.2: L-problem: Summary of results to the final designs of Fig. 6.12 using FE and FV schemes.

Final design	Scheme	Mass ratio	$W(\phi)$	$\max_D(g_r)$
Fig. 6.12(b)	FE	0.5335	199.14	-3.2×10^{-3}
Fig. 6.12(d)	FV	0.5030	205.92	3.1×10^{-3}

From an initial level set domain with holes (see Fig. 6.12a), FE and FV schemes are employed to the evolution of the reaction-diffusion equation.

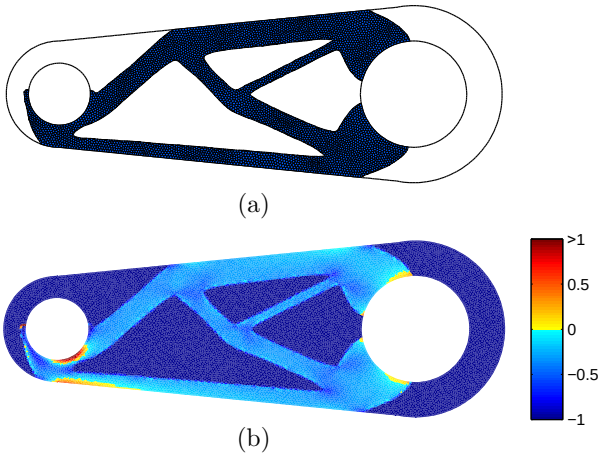

Figure 6.11: Wrench problem: (a) final design for the compliance problem; and (b) stress constraint distribution with $\max_D(g_r) = 5.75$. The mass constraint was set to 40% of the total mass. The compliance $W(\phi)$ of the final design is 111.66.

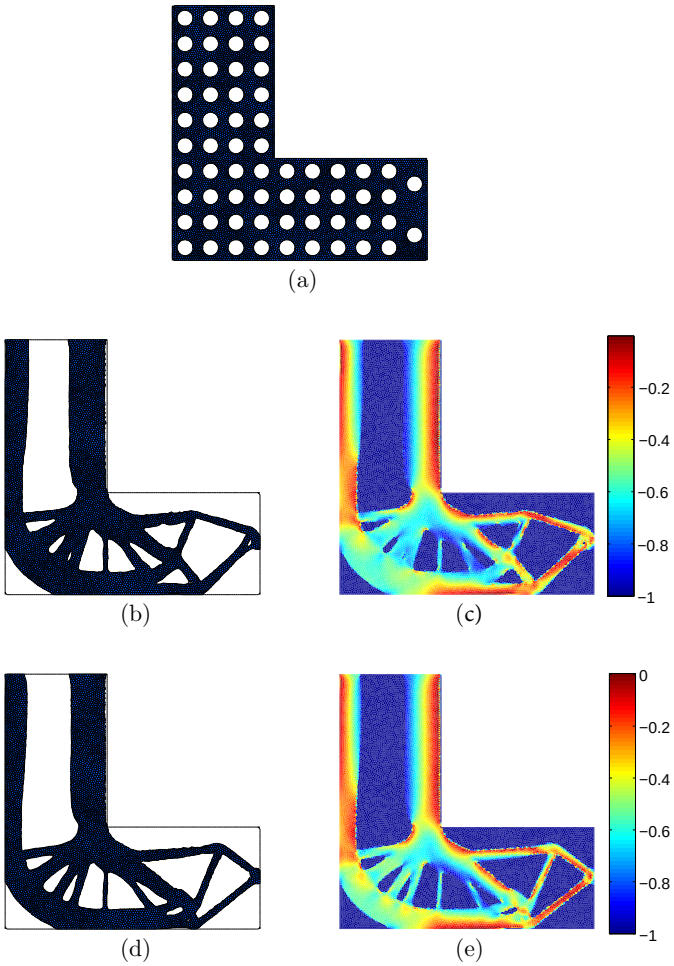

Figure 6.12: L-problem: (a) Initial level set topology; (b) Final design using FE scheme; (c) stress constraint distribution; (d) Final design using FV scheme; (e) stress constraint distribution.

The final topologies and its corresponding stress constraint distributions are shown, respectively, in Fig. 6.12(b) and (c) for the FE scheme, and Fig. 6.12(d) and (e) for the FV scheme. A comparative analysis for the mass ratio, the compliance $W(\phi)$ and the maximum value of the stress constraint are showed in Tab. 6.2 for both schemes.

Next, using only the FV scheme the L-shape problem is tested from a solid initial configuration (no holes). Figure 6.13(a) shows the initial level set domain and Fig. 6.13(b)-(f) show the intermediate results during the minimization. Note that the stress concentration is eliminated at the beginning of the optimization process, and thereafter was started the nucleation of holes in the domain. The final design and its stress constraint distribution are presented in Fig. 6.14(a) and (b), respectively. The graphics for the convergence of the mass ratio and objective function, the penalty terms (linear and quadratic) and the compliance term are also shown in Fig. 6.14(c), (d) and (e), respectively. Observe that the stress penalization terms converge to zero at the final of optimization.

Now, the region of load application is shifted: P is applied at the top of the right side (see Fig. 6.15). The parameters remain unchanged, except $a = 1$ and only 30 updates of the external loop. A different initial configuration with random values is assigned to the level set function, as shown in Fig. 6.16(a). The intermediate results of the optimization process are shown in Fig. 6.16(b)-(f). The final topology is presented in Fig. 6.17(a). A zoom near the reentrant corner (Fig. 6.17b) shows the well-defined round that eliminated the stress concentration. The stress constraint distribution and the convergence along the iterations for the mass ratio and objective function are shown in Fig. 6.17(c) and (d), respectively.

Note that the L-shape example was tested for different initial configurations and boundary condition obtaining optimal designs and numerical data quite differents. However, all optimal topologies eliminated the stress concentration with a rounding radius in the corner.

6.4.3 Crack problem

Again the problem of a plate emulating a fracture mode I is discussed. The following parameters are adopted: $P = 1$ N, $L = 1$ m and $\sigma_{adm} = 23$ Pa. The remaining parameters of optimization are: $c = 0.25$ ($c_{\max} = 20c$), $\beta = 1.1$, $\mu = 0.004$, $C = 0.5$, $p = 1.001$, $a = 1$ and $\tau = 1 \times 10^{-5}$. Moreover, the minimization was stopped after 30 updates of the external loop giving a

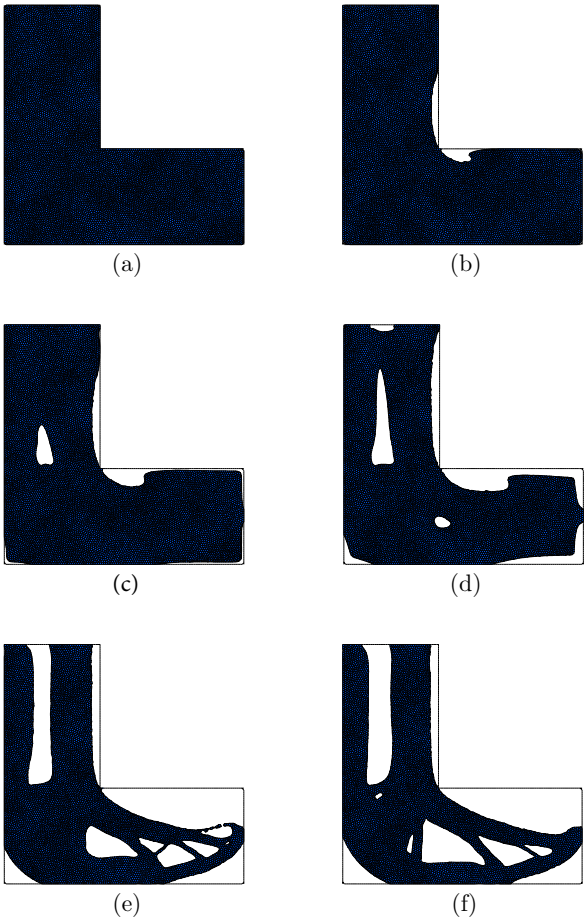

Figure 6.13: L-problem: (a) initial level set domain; Intermediate results at iterations: (b) 40; (c) 60; (d) 80; (e) 200; and (f) 400.

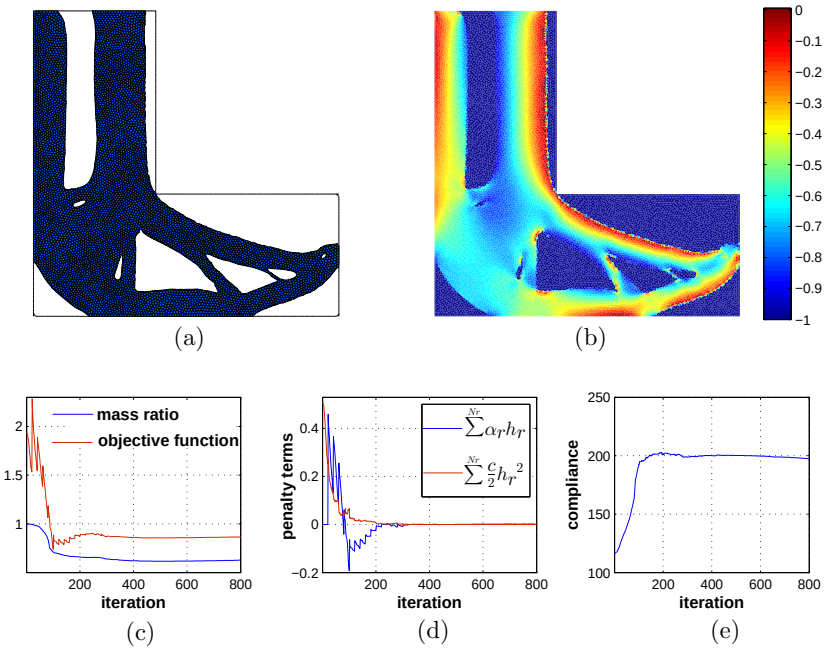

Figure 6.14: L-problem: (a) final design at iteration 800; (b) stress constraint distribution with $\max_D(g_r) = 5.3 \times 10^{-3}$; (c) convergence history of the mass ratio (final mass ratio is 0.6277); (d) convergence of the stress penalization terms (linear and quadratic); and (e) convergence of the compliance term (final value is 197.43).

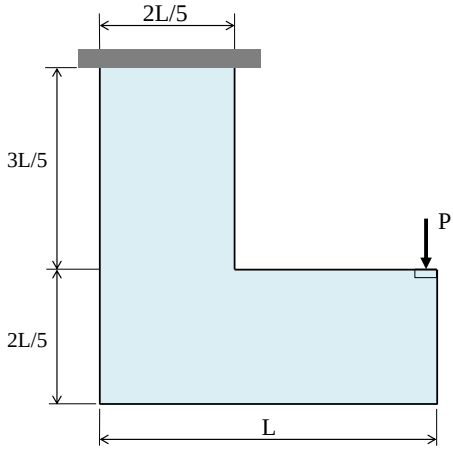

Figure 6.15: L-problem: model 2.

total of $30 \times 20 = 600$ iterations. In this example, the loading was applied at three distinct locations (no simultaneous) of the model.

The first location of the loading consists on the model of Fig. 5.16. This case was tested in the previous chapter where the force P is applied on the lateral of the plate. Only the right symmetric part was discretized with a mesh of $10,000$ polygonal elements and $19,844$ nodes (equal to the number of stress sample points N_r). From an initial configuration with arbitrary values for the level set function (see Fig. 6.18a), the final topology using FE scheme and its respective stress constraint distribution are shown in Fig. 6.18(b) and (c), respectively. On the other hand, the final design using FV scheme and its corresponding stress constraint distribution are shown in Fig. 6.18(d) and (e), respectively.

Also, considering the same load location (Fig. 5.16) but a different initial configuration (see Fig. 6.19a), the optimal design (only using FV scheme) is shown in Fig. 6.19(b). The respective distribution of (nodal) stress constraints is presented in Fig. 6.19(c). The graphics of the objective function and the regularization term are shown in Fig. 6.19(d) and (e), respectively. Some numerical data of the obtained designs are reported in Table 6.3 for comparison.

Next, the loading is applied at a hole in the interior of the domain. Two

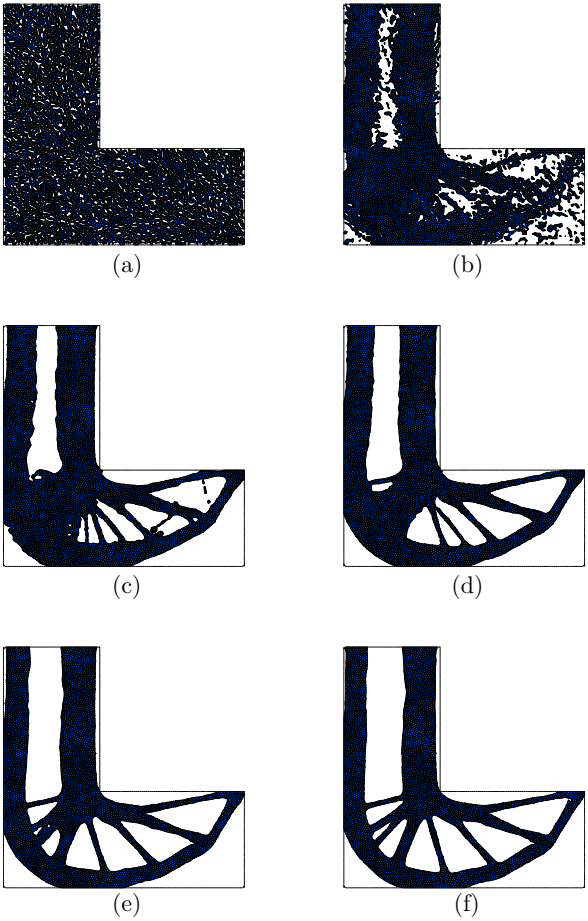

Figure 6.16: L-problem: (a) random initial level set domain; Intermediate results at iterations: (b) 40; (c) 160; (d) 200; (e) 260; and (f) 360.

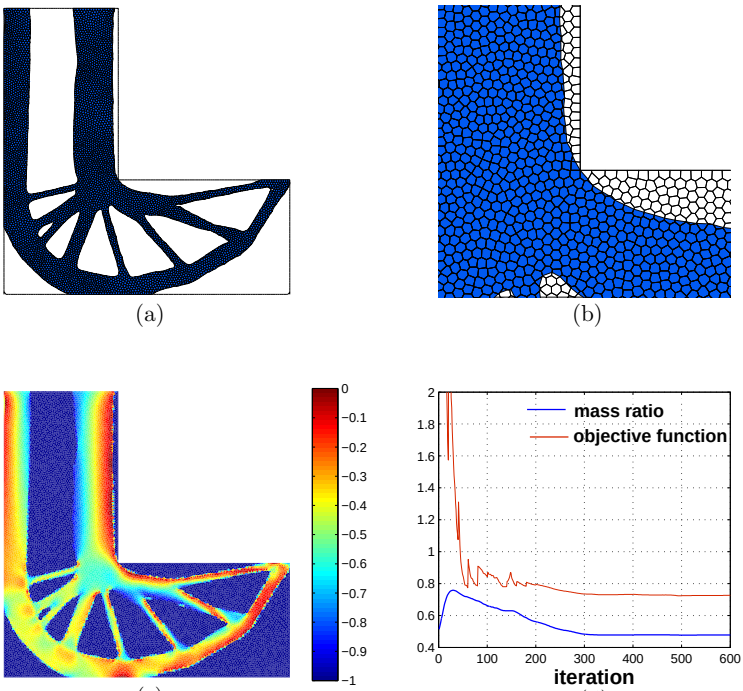

Figure 6.17: L-problem: (a) final design at iteration 600; (b) zoom near the reentrant corner; (c) stress constraint distribution with $\max_D(g_r) = 8.99 \times 10^{-4}$; and (d) convergence history of the mass ratio (final mass ratio is 0.4782) and objective function.

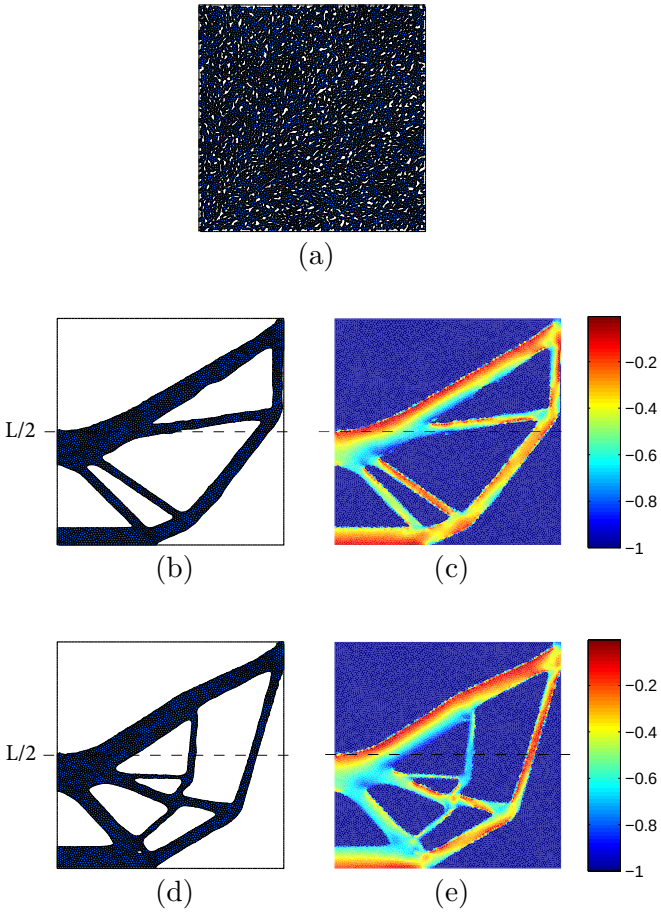

Figure 6.18: Crack problem: (a) Initial level set topology; (b) Final design using FE scheme; (c) stress constraint distribution; (d) Final design using FV scheme; (e) stress constraint distribution.

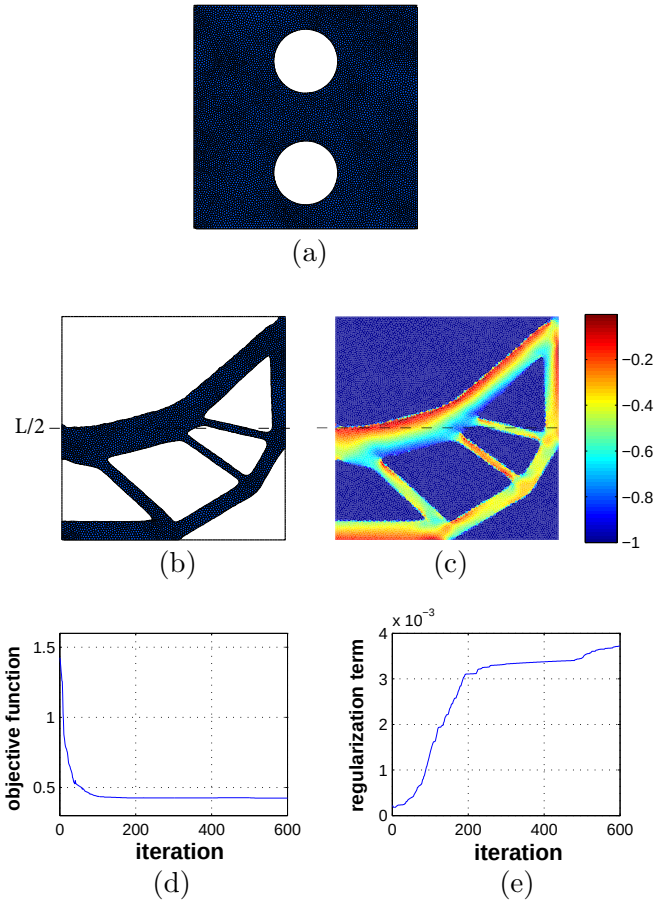

Figure 6.19: Crack problem: (a) Initial level set domain; (b) final design using FV scheme; (c) stress constraint distribution; (d) convergence history of the objective function; and (e) behavior of the regularization term.

Table 6.3: Crack problem: Summary of results to the final design of Fig. 6.18 and 6.19.

Final design	Scheme	Mass ratio	$W(\phi)$	$\max_D(g_r)$
Fig. 6.18(b)	FE	0.26	57.55	-5.1×10^{-3}
Fig. 6.18(d)	FV	0.2791	54.13	-3.6×10^{-3}
Fig. 6.19(b)	FV	0.3027	58.94	-3.6×10^{-3}

distinct positions of the hole were considered where the force P is distributed along of semi-circle, as can be seen in Fig. 6.20. Only the right symmetric part of the plate was discretized with $10,000$ polygonal elements. Using FV scheme, Fig. 6.21 shows the initial configuration (with no holes), the final design and the stress constraint distribution for positions 1 and 2 of the hole. The data for the mass ratio, the compliance $W(\phi)$ and the maximum value of the stress constraints are shown in Table 6.4 to the two positions of the load. Observe that the final designs eliminated the stress singularity and a feasible design is achieved.

Table 6.4: Crack problem: Summary of results to the final designs of Fig. 6.21 for the hole in the positions 1 and 2.

Final design	Hole	Scheme	N_r	Mass ratio	$W(\phi)$	$\max_D(g_r)$
Fig. 6.21(b)	position 1	FV	$19,842$	0.2099	30.64	1×10^{-3}
Fig. 6.21(e)	position 2	FV	$19,840$	0.2315	27.60	-3×10^{-3}

6.4.4 Cantilever modified

This numerical example deals with a cantilever beam problem containing a stress singularity. The design domain D is clamped at left side and a distributed vertical force $P = 1$ N is applied on the bottom of the right side, as shown in Fig. 6.22. It is assumed a yield stress $\sigma_{adm} = 74$ Pa. Domain D was discretized with $10,000$ polygonal elements and $19,905$ nodes (that is, $N_r = 19,905$ sample points for the stress evaluation). Figure 6.23 shows the stress constraint distribution of the model presenting a high stress concentration in the geometrical singularity and at the clamp. The following parameters were used: $c = 0.5$ ($c_{\max} = 30c$), $\beta = 1.1$, $\mu = 0.0008$, $C = 0.5$, $p = 1.001$, $a = 1$ and $\tau = 4\times10^{-5}$. For this example, only FV scheme was employed.

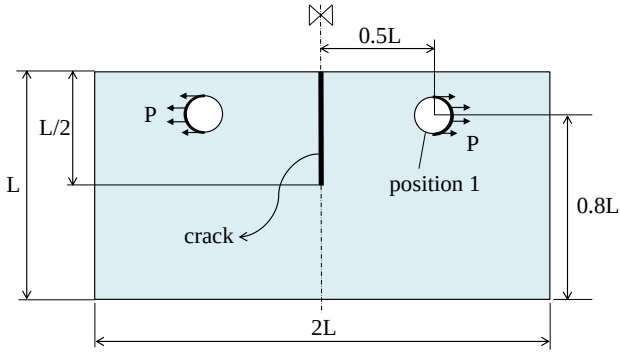

(a) Model with hole at position 1

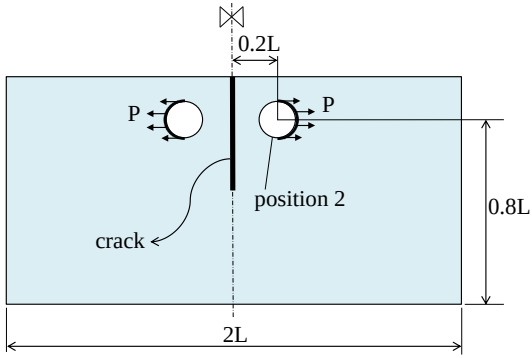

(b) Model with hole at position 2

Figure 6.20: Crack problem: Models with loading applied in a hole.

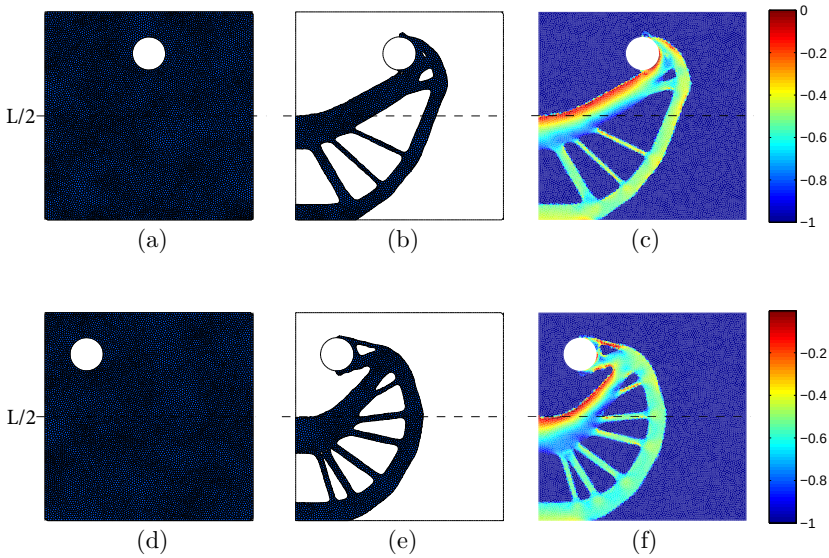

Figure 6.21: Crack problem: (a) Initial level set topology; (b) Final design to the loading applied at position 1; (c) stress constraint distribution of b; (d) Initial level set topology; (e) Final design to the loading applied at position 2; and (f) stress constraint distribution of e.

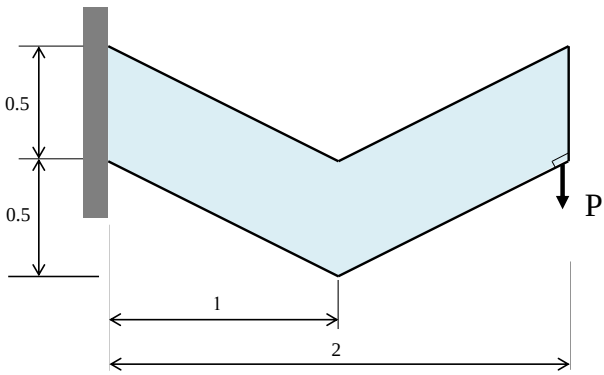

Figure 6.22: Cantilever modified: model.

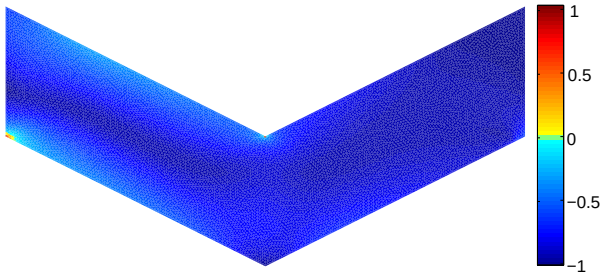

Figure 6.23: Cantilever modified: Stress constraint distribution of the model with $\max_D(g_r) = 1.04$.

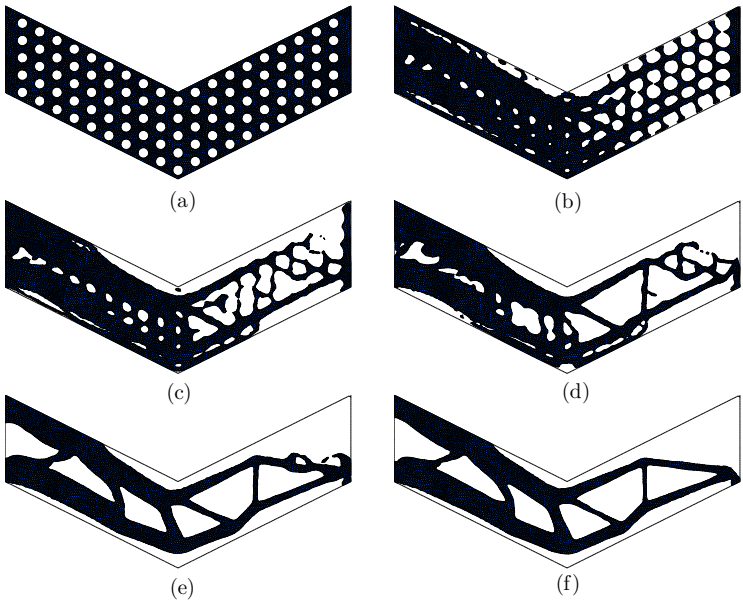

Figure 6.24: Cantilever modified: (a) initial level set domain; Intermediate results at iterations: (b) 10; (c) 40; (d) 70; (e) 200; and (f) 400.

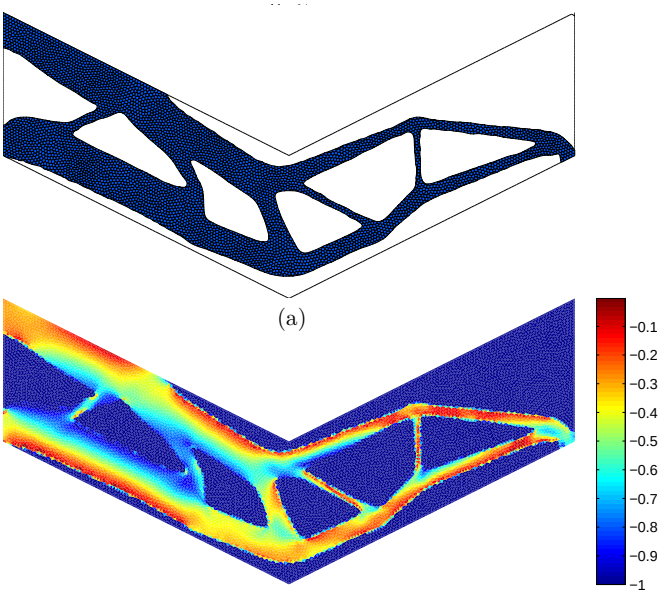

(a)

(b)

Figure 6.25: Cantilever modified: (a) Final design from the initial configuration of Fig. 6.24a; and (b) stress constraint distribution with $\max_D(g_r) = -2.8 \times 10^{-3}$.

From an initial level set domain with holes (Fig. 6.24a), the intermediate results during the minimization process are shown in Fig. 6.24(b)-(f). Note that the singularity in the corner is easily eliminated on the first iterations. The final topology and its respective (nodal) stress constraint distribution are shown in Fig. 6.25(a) and (b), respectively.

Now, the algorithm is tested from an initial configuration with random values to the level set function (see Fig. 6.26a). The final design and the corresponding stress constraints are shown in Fig. 6.26(b) and (c), respectively. Observe as the final design can be different depending on the initial configuration. However, both results found a feasible local minimum to get rid of the initial stress concentrations. Figure 6.27 shows the graphics of the objective function and mass ratio for the two initial configurations.

Although the minimum compliance problem is not the main purpose of the present work, it was also tested for comparison reasons. Figure 6.28(a) shows the final topology with mass constraint set to 42% of the total mass (the same mass ratio of Fig. 6.25a and 6.26b). Figure 6.28(b) shows the corresponding stress constraint distribution. Note that the initial stress concentrations were not eliminated but increased even further.

Finally, the obtained design for the minimum compliance problem (Fig. 6.28a) is used as the initial level set domain for the stress constraint problem. Figure 6.29(a) and (b) show the final design obtained after 20 updates of the external loop and the corresponding stress constraint distribution, respectively. Observe that the value of the maximum stress constraint g_r in D was drastically reduced. The values for the mass ratio, the compliance $W(\phi)$ and the maximum value of the stress constraint are presented in Tab. 6.5 for each final design obtained in this example.

Table 6.5: Cantilever modified: Summary of results of the final topologies shown in Fig. 6.25 (from an initial configuration with holes), Fig. 6.26 (from a random initial domain), Fig. 6.28a (obtained design to the minimum compliance problem) and Fig. 6.29a (initial configuration is Fig. 6.28a).

Final design	Scheme	Mass ratio	$W(\phi)$	$\max_D(g_r)$
Fig. 6.25(a)	FV	0.42	834.4	-2.8×10^{-3}
Fig. 6.26(b)	FV	0.42	856.57	-7.0×10^{-3}
Fig. 6.28(a)	FV	0.42	589.20	1.96
Fig. 6.29(a)	FV	0.37	772.99	9.19×10^{-4}

Clearly, it was verified that the greatest difficulty of the algorithm

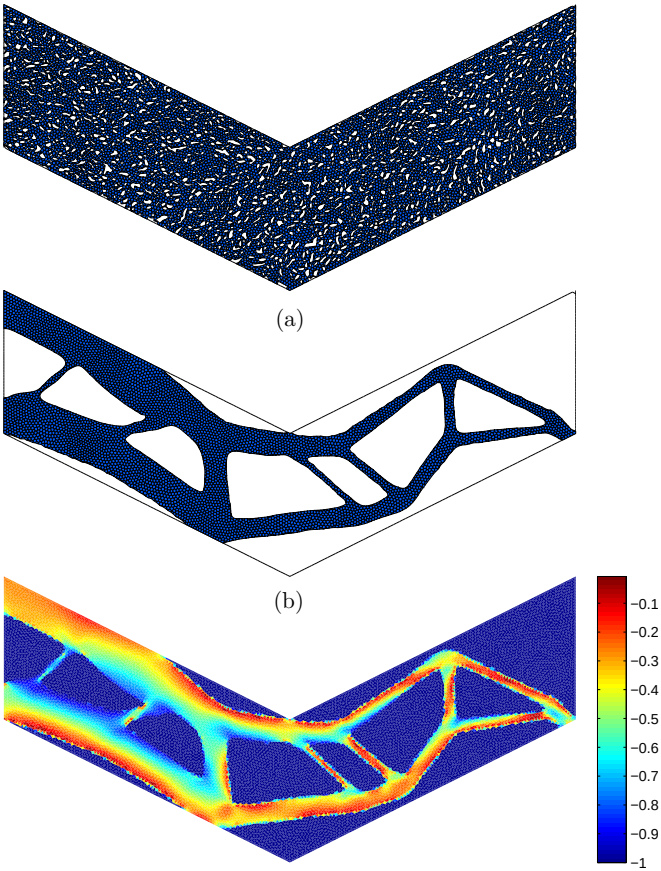

Figure 6.26: Cantilever modified: (a) random initial level set domain; (b) final design; and (c) stress constraint distribution with $\max_D(g_r) = -7 \times 10^{-3}$.

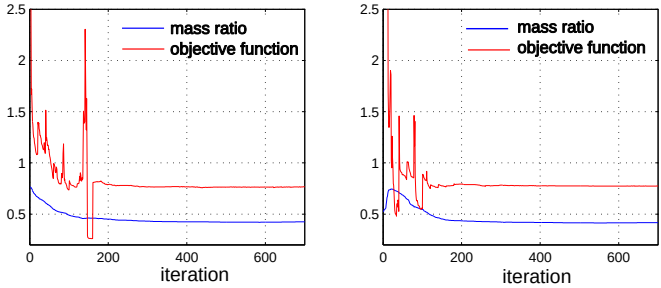

(a) initial domain with holes (b) random initial domain

Figure 6.27: Cantilever modified: Objective function and mass ratio for different initial configurations.

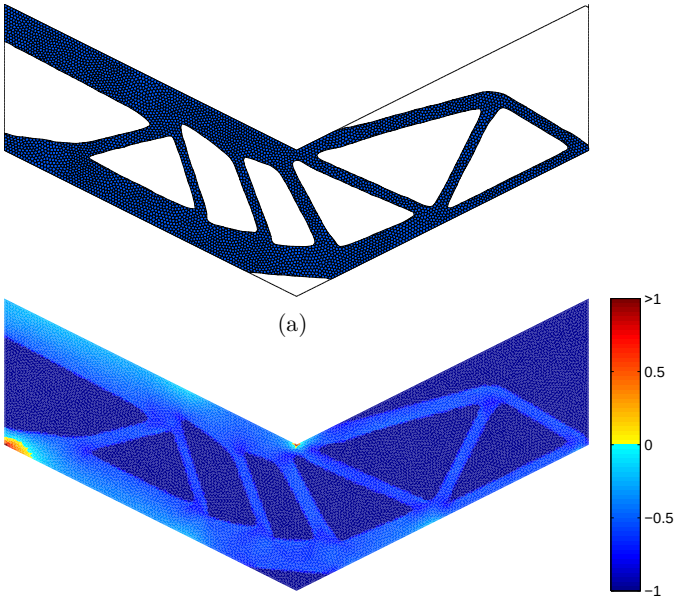

(a)

(b)

Figure 6.28: Cantilever modified: (a) Final design for the compliance problem; and (b) stress constraint distribution with $\max_D(g_r) = 1.96$.

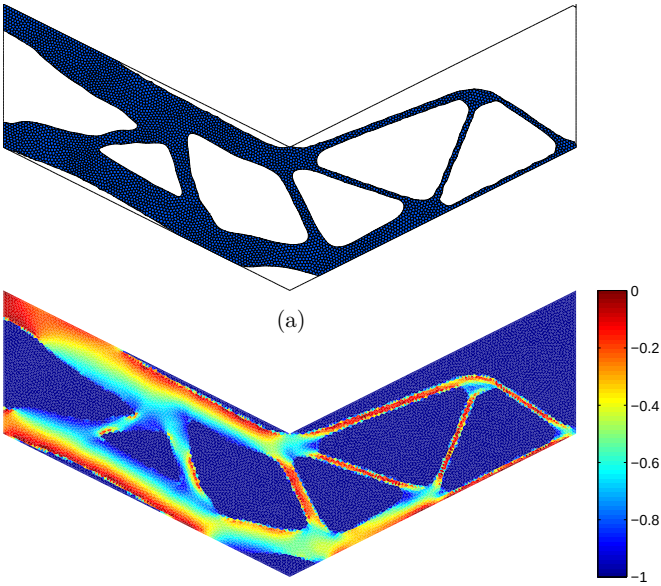

(a)

(b)

Figure 6.29: Cantilever modified: Considering the initial level set domain the design obtained for the compliance problem (Fig. 6.28a), (a) shows the final design after 400 iterations for the stress-constrained problem; and (b) stress constraint distribution with $\max_D(g_r) = 9.19 \times 10^{-4}$.

along of the optimization process is to satisfy the stress constraints at the clamp (see region with high stress in Fig. 6.23). Observe that for all the optimal topology designs the boundary of $\partial\Omega$ is detached from ∂D at the region near the clamp.

6.5 CONCLUDING REMARKS

Rather than using a regular background grid of quadrilateral elements, an unstructured mesh with polygonal finite elements was used in present chapter to solve the optimization problem set up in Chapter 5. Some comments are worth mentioning:

1. Voronoi polygonal meshes showed to be a viable option for meshing general domains, typical of practical engineering applications. Irregular background domains and respective meshes were easily used with successful results. In the same way, as observed in regular background domains, feasible designs were achieved with the same ability to eliminate corners with stress concentrations. In addition, overall numerical costs associated to the meshes are comparable to that of regular ones.

2. The (discrete) definition of the neighbors of sample points associated with the geometric properties of the polygonal elements based on Voronoi Tessellations allowed for employing a finite volume scheme, providing good results.

3. During the optimization process, it was observed that the polygonal discretization had some difficulties to stabilize on a final design. This behavior may be due to a tendency of the algorithm to keep thin bars in the design (that is, bars formed by only one element). Thus, when the rupture of a thin bar occurs, the energy accumulated by this bar is transferred to the structure causing convergence oscillations along the iterations.

7 CONCLUSIONS

The main goal of this thesis was to propose and evaluate the effectiveness of a level-set-based approach for topology optimization problems involving local stress constraints. Chapter 3 provided theoretical foundations necessary to describe the proposed problem. A detailed discussion of the sensitivity analysis and the similarities between the design evolution using time integration and mathematical programming techniques are provided in the text. The work also described various scaling, smoothing and normalization steps that are applied in order to obtain good convergence. For each case, discretization aspects were discussed. Additional variations in parameters or meshes were studied and were helpful in illustrating the robustness of the method and the influence of various settings. Details about the performance of the proposed formulation were also provided using multiple benchmark problems. Next, a summary of the main contributions of this work, followed by some overall considerations and suggestions for future research are presented.

7.1 SUMMARY OF CONTRIBUTIONS

In Chapter 3 two novel strategies to solve the topology optimization problem are proposed. The first one consists of an appropriate stress constraint expression for the continuous inclusion/exclusion of stress points during the boundary movements. The second novel strategy consists on the simultaneous use of an augmented Lagrangian mathematical programming technique and level sets implicit boundaries for handling local stress constraints in topology optimization.

Also, Chapter 5 presents a novelty by using a reaction-diffusion equation to solve the stress-constrained problem within a level set approach. The proposed formulation allows for results in better optimized performance with reduced dependence on the initial design. Among other characteristics, it has the capability of introducing new holes along the optimization procedure, and a level set evolution free of reinitialization that provides significant improvements in local stress constrained problems.

Another novelty associated with the efficiency in the minimization sequences is the successful proposition of post processing treatment on the velocity field used in the evolution equations.

Finally, a novel level set with a polygonal finite element approach is

presented. Parallely, the (discrete) definition of the neighborhood of sample points from central Voronoi tessellations allowed for the application of finite volume numerical schemes.

7.2 OVERALL CONSIDERATIONS

Different evolution equations and meshes were employed to the level set updating. So, in order to obtain a better understanding of each proposed approach, concluding remarks were presented in each chapter that showed numerical results. However, some overall considerations are worth mentioning:

- It is proposed the definition of a neighborhood around each sample point (node) in such a way that the activation of the stress constraint associated to the sample point is proportional to the overlapping between the current domain and the considered neighborhood. In this way, the activation/deactivation of stress constraints associated to the sample points is performed in a continuous way as long as the boundary moves over the background domain D. The stress measured, however, remains *local* in the sense that it represents the stress at $\mathbf{x}_r$ and not its average over a neighborhood.

- A stress constraint function was proposed in such a way that enhances the area fraction $H_r(\phi) < 1$ that measures the intersection between Ω and the neighborhood of $\mathbf{x}_r$. This is performed by an exponent $q < 1$. However, small values of q have an almost discontinuous behavior of the stress constraints with respect to the boundary movement. Consequently, the optimization algorithm can present convergence difficulties.

- A very simple recovering technique was employed to obtain a continuous strain field based on the same bilinear shape functions used for the displacement solution (other techniques could be tested). Then as pointed out in Section 4.3.2, a distribution of sample points that are coincident with the nodes of the (Lagrangian) mesh is consistent with the objective of enforcing the stress constraint all over the domain. It is then possible to say that with this choice, the number and position of sample points follow the resolution of the stress field provided by the finite element mesh.

- In Chapter 5 and 6 (where a reaction-diffusion equation is used), it was assumed a stress penalization exponent $p > 1$. As a consequence, the Heaviside function in the velocity field cancels terms for all points outside the material region. The proposed methodology requires this consideration for the optimization algorithm to find a feasible topology.

- Only the finite element scheme has been utilized in Chapter 5 to solve the reaction-diffusion equation. However, structured quadrilateral meshes have the necessary geometry properties to employ the finite volume scheme as well.

- Let a polygonal mesh and a quadrilateral mesh with the same number of nodes. Both meshes provide a problem with the same number of constraints and similar size of stiffness matrix. In general, in these cases a polygonal mesh holds a lower number of elements and, thus, it can have a worst representation of the zero level set curves.

7.3 FUTURE WORK

Based on the results achieved, the following proposals are pointed out as possible activities for future work:

- So far, the approach has been applied only for single load cases. The first suggestion for taking advantage of the proposed methodology is to extend the formulation to multiple load cases and/or contact boundary conditions.

- As the problem was generically formulated for any dimension, a challenging suggestion for future developments is to implement the proposed formulation to 3D problems. Stress-constrained topology optimization problems with successful results in 3D remain scarce in the literature.

- Another topic for future research is to use the proposed approach with another method of implicit function description, as for example, phase field method.

- An interesting extension is to employ a failure criterion with different stress limits in tension and compression.

- An addition that would be complementary is to employ triangle elements from Delaunay triangulations to the discretization of the problem. In the same way as performed with polygonal elements, it is possible to use the finite volume scheme for updating the level set since the Delaunay triangulation is the dual of the Voronoi tessellation.

- Another important extension is to include the recent developments with manufacturing constraints, namely Additive Manufacturing (3D printing), for the proposed approach.

REFERENCES

[1] PEREIRA, J. T.; FANCELLO, E. A.; BARCELLOS, C. S. Topology optimization of continuum structures with material failure constraints. *Structural and Multidisciplinary Optimization*, v. 26, p. 50–66, 2004.

[2] DUYSINX, P.; BENDSØE, M. P. Topology optimization of continuum structures with local stress constraints. *International Journal for Numerical Methods in Engineering*, v. 1478, n. June 1997, p. 1453–1478, 1998.

[3] FANCELLO, E. A.; PEREIRA, J. T. Structural topology optimization considering material failure constraints and multiple load conditions. *Latin American Journal of Solids and Structures*, v. 1, p. 3–24, 2003.

[4] FANCELLO, E. A. Topology optimization for minimum mass design considering local failure constraints and contact boundary conditions. *Structural and Multidisciplinary Optimization*, v. 32, p. 229–240, 2006.

[5] ALLAIRE, G.; JOUVE, F.; MAILLOT, H. Topology optimization for minimum stress design with the homogenization method. *Structural and Multidisciplinary Optimization*, v. 28, p. 87–98, 2004.

[6] GUILHERME, C. E. M.; FONSECA, J. S. O. Topology optimization of continuum structures with e-relaxed stress constraints. In: ALVES, M.; da Costa Mattos, H. S. (Ed.). *Mechanics of Solids in Brazil*. Rio de Janeiro, Brasil: ABCM, 2007. p. 239–250.

[7] PARÍS, J. et al. Topology optimization of continuum structures with local and global stress constraints. *Structural and Multidisciplinary Optimization*, v. 39, p. 419–437, 2009.

[8] PARÍS, J. et al. Block aggregation of stress constraints in topology optimization of structures. *Advances in Engineering Software*, Elsevier Ltd, v. 41, n. 3, p. 433–441, 2010.

[9] LE, C. et al. Stress-based topology optimization for continua. *Structural and Multidisciplinary Optimization*, v. 41, n. 4, p. 605–620, 2010.

[10] LEE, E.; JAMES, K. A.; MARTINS, J. R. R. A. Stress-constrained topology optimization with design-dependent loading. *Structural and Multidisciplinary Optimization*, v. 46, n. 5, p. 647–661, 2012.

[11] MOON, S. J.; YOON, G. H. A newly developed qp-relaxation method for element connectivity parameterization to achieve stress-based topology optimization for geometrically nonlinear structures. *Computer Methods in Applied Mechanics and Engineering*, Elsevier B.V., v. 265, p. 226–241, 2013.

[12] LUO, Y.; WANG, M. Y.; KANG, Z. An enhanced aggregation method for topology optimization with local stress constraints. *Computer Methods in Applied Mechanics and Engineering*, Elsevier B.V., v. 254, p. 31–41, 2013.

[13] HOLMBERG, E.; TORSTENFELT, B.; KLARBRING, A. Stress constrained topology optimization. *Structural and Multidisciplinary Optimization*, v. 48, n. 1, p. 33–47, 2013.

[14] LUO, Y. et al. Reliability based topology optimization for continuum structures with local failure constraints. *Computers and Structures*, Elsevier Ltd, v. 143, p. 73–84, 2014.

[15] FARIAS, J.-M. C.; CARDOSO, E. L.; MUÑOZ-ROJAS, P. A. Topology optimization with stress constraints using superconvergent patch recovery. In: *3rd International Symposium on Solid Mechanics*. Florianópolis, SC, Brazil: [s.n.], 2011. p. 175–195.

[16] CHENG, G.; GUO, X. ε-relaxed approach in structural topology optimization. *Structural and Multidisciplinary Optimization*, v. 13, p. 258–266, 1997.

[17] BRUGGI, M. On an alternative approach to stress constraints relaxation in topology optimization. *Structural and Multidisciplinary Optimization*, v. 36, n. 2, p. 125–141, jan 2008.

[18] BRUGGI, M.; VENINI, P. A mixed FEM approach to stress-constrained topology optimization. *International Journal for Numerical Methods in Engineering*, John Wiley & Sons, v. 73, n. 12, p. 1693–1714, 2008.

[19] BRUGGI, M.; DUYSINX, P. Topology optimization for minimum weight with compliance and stress constraints. *Structural and Multidisciplinary Optimization*, v. 46, n. 3, p. 369–384, jan 2012.

[20] LUO, Y.; KANG, Z. Topology optimization of continuum structures with Drucker-Prager yield stress constraints. *Computers and Structures*, Elsevier Ltd, v. 90-91, p. 65–75, 2012.

[21] AMSTUTZ, S.; NOVOTNY, A.; SOUZA-NETO, E. Topological derivative-based topology optimization of structures subject to Drucker-Prager stress constraints. *Computer Methods in Applied Mechanics and Engineering*, Elsevier B.V., v. 233-236, p. 123–136, 2012.

[22] JEONG, S. H.; CHOI, D.-H.; YOON, G. H. Fatigue and static failure considerations using a topology optimization method. *Applied Mathematical Modelling*, Elsevier Inc., v. 39, n. 3-4, p. 1137–1162, 2015.

[23] SETHIAN, J. A.; WIEGMANN, A. Structural boundary design via level set and immersed interface methods. *Journal of Computational Physics*, v. 163, n. 2, p. 489–528, 2000.

[24] BELYTSCHKO, T.; XIAO, S. P.; PARIMI, C. Topology optimization with implicit functions and regularization. *International Journal for Numerical Methods in Engineering*, v. 57, n. 8, p. 1177–1196, 2003.

[25] ALLAIRE, G.; JOUVE, F.; TOADER, A. M. Structural optimization using sensitivity analysis and a level-set method. *Journal of Computational Physics*, v. 194, p. 363–393, 2004.

[26] WANG, M. Y.; WANG, X. M.; GUO, D. M. A level set method for structural topology optimization. *Computer Methods in Applied Mechanics and Engineering*, v. 192, p. 217–224, 2003.

[27] SETHIAN, J. A. *Level Set Method and Fast Marching Methods: Evolving Interfaces in Computational Geometry, Fluid Mechanics, Computer Vision, and Materials Science*. Cambridge, U.K.: Cambridge University Press, 1999.

[28] AMSTUTZ, S.; ANDRÄ, H. A new algorithm for topology optimization using a level-set method. *Journal of Computational Physics*, v. 216, n. 2, p. 573–588, 2006.

[29] WANG, S. Y. et al. An extended level set method for shape and topology optimization. *Journal of Computational Physics*, v. 221, p. 395–421, 2007.

[30] JIA, H. et al. Evolutionary level set method for structural topology optimization. *Computers and Structures*, 2011.

[31] DUNNING, P. D.; KIM, H. A. A new hole insertion method for level set based structural topology optimization. *International Journal for Numerical Methods in Engineering*, v. 93, p. 118–134, 2013.

[32] LUO, Z. et al. A level set-based parameterization method for structural shape and topology optimization. *International Journal for Numerical Methods in Engineering*, v. 76, n. 1, p. 1–26, 2008.

[33] LUO, J. et al. A semi-implicit level set method for structural shape and topology optimization. *Journal of Computational Physics*, v. 227, p. 5561–5581, 2008.

[34] YAMASAKI, S. et al. A structural optimization method based on the level set method using a new geometry-based re-initialization scheme. *International Journal for Numerical Methods in Engineering*, v. 83, n. 12, p. 1580–1624, 2010.

[35] LUO, Z. et al. Structural shape and topology optimization using a meshless Galerkin level set method. *International Journal for Numerical Methods in Engineering*, v. 90, n. 3, p. 369–389, 2011.

[36] MOHAMADIAN, M.; SHOJAEE, S. Binary level set method for structural topology optimization with MBO type of projection. *International Journal for Numerical Methods in Engineering*, v. 89, p. 658–670, 2012.

[37] YAMADA, T. et al. A topology optimization method based on the level set method incorporating a fictitious interface energy. *Computer Methods in Applied Mechanics and Engineering*, Elsevier B.V., v. 199, n. 45-48, p. 2876–2891, 2010.

[38] CHOI, J. S. et al. Topology optimization using a reaction-diffusion equation. *Computer Methods in Applied Mechanics and Engineering*, Elsevier B.V., v. 200, n. 29-32, p. 2407–2420, jul 2011.

[39] OSHER, S.; FEDKIW, R. *Level Set Methods and Dynamic Implicit Surfaces*. New York: Springer, 2003.

[40] DIJK, N. P. V. et al. Level-set methods for structural topology optimization: a review. *Structural and Multidisciplinary Optimization*, v. 48, n. 3, p. 437–472, 2013.

[41] GAIN, A. L.; PAULINO, G. H. A critical comparative assessment of differential equation-driven methods for structural topology optimization. *Structural and Multidisciplinary Optimization*, v. 48, n. 4, p. 685–710, 2013.

[42] ALLAIRE, G.; JOUVE, F. Minimum stress optimal design with the level set method. *Engineering Analysis with Boundary Elements*, v. 32, p. 909–918, 2008.

[43] JAMES, K. A.; LEE, E.; MARTINS, J. R. Stress-based topology optimization using an isoparametric level set method. *Finite Elements in Analysis and Design*, Elsevier, v. 58, p. 20–30, oct 2012.

[44] MIEGROET, L. van; DUYSINX, P. Stress concentration minimization of 2D filets using X-FEM and level set description. *Structural and Multidisciplinary Optimization*, v. 33, n. 4-5, p. 425–438, 2007.

[45] XIA, Q. et al. A level set solution to the stress-based structural shape and topology optimization. *Computers and Structures*, Elsevier Ltd, v. 90-91, p. 55–64, jan 2012.

[46] XIA, Q.; SHI, T.; WANG, M. Y. A level set based method for topology optimization of continuum structures with stress constraint. In: *6th China-Japan-Korea Joint Symposium on Optimization of Structural and Mechanical Systems*. Kyoto, Japan: [s.n.], 2010.

[47] GUO, X.; ZHANG, W. S.; WANG, M. Y. Stress-related topology optimization via level set approach. In: *6th China-Japan-Korea Joint Symposium on Optimization of Structural and Mechanical Systems*. Kyoto, Japan: [s.n.], 2010.

[48] GUO, X. et al. Stress-related topology optimization via level set approach. *Computer Methods in Applied Mechanics and Engineering*, Elsevier B.V., v. 200, n. 47-48, p. 3439–3452, 2011.

[49] VERBART, A. et al. Level Set Based Topology Optimization with Stress Constraints and Consistent Sensitivity Analysis. In: *53rd AIAA/ASCE/AHS/ASC Structures, Structural Dynamics and Materials Conference*. Honolulu, Hawaii: [s.n.], 2012.

[50] WANG, M. Y.; LI, L. Shape equilibrium constraint: a strategy for stress-constrained structural topology optimization. *Structural and Multidisciplinary Optimization*, v. 47, n. 3, p. 335–352, 2013.

[51] EMMENDOERFER-JR, H.; FANCELLO, E. A. A level set approach for topology optimization with local stress constraints. *International Journal for Numerical Methods in Engineering*, v. 99, n. April, p. 129–156, 2014.

[52] ZHANG, W. S. et al. Optimal topology design of continuum structures with stress concentration alleviation via level set method. *International Journal for Numerical Methods in Engineering*, v. 93, p. 942–959, 2013.

[53] BURGER, M.; STAINKO, R. Phase-field relaxation of topology optimization with local stress constraints. *SIAM Journal of Control Optimization*, v. 45, n. 4, p. 1447–1466, 2006.

[54] JEONG, S. H. et al. Development of a novel phase-field method for local stress-based shape and topology optimization. *Computers and Structures*, Elsevier Ltd, v. 132, p. 84–98, feb 2014.

[55] AMSTUTZ, S.; NOVOTNY, A. A. Topological optimization of structures subject to Von Mises stress constraints. *Structural and Multidisciplinary Optimization*, v. 41, n. 3, p. 407–420, 2010.

[56] SURESH, K.; TAKALLOOZADEH, M. Stress-constrained topology optimization: a topological level-set approach. *Structural and Multidisciplinary Optimization*, v. 48, n. 2, p. 295–309, 2013.

[57] OSHER, S.; SETHIAN, J. Fronts propagating with curvature-dependent speed: Algorithms based on Hamilton-Jacobi formulations. *Journal of Computational Physics*, v. 79, p. 12–49, 1988.

[58] DIJK, N. P. V.; LANGELAAR, M.; KEULEN, F. V. Explicit level-set-based topology optimization using an exact Heaviside function and consistent sensitivity analysis. *International Journal for Numerical Methods in Engineering*, v. 91, n. May, p. 67–97, 2012.

[59] BERTSEKAS, D. P. *Constrained Optimization and Lagrange Multiplier Methods*. Belmont, MA, U.S.A.: Athena Scientific, 1996.

[60] MARTíNEZ, J. M. *Otimização prática usando o Lagrangiano Aumentado*. [S.l.], 2009. Disponível em: <http://www.ime.unicamp-.br/*nsim*martinez/lagraum.pdf>.

[61] HAUG, E. J.; CHOI, K. K.; KOMKOV, V. *Design Sensitivity Analysis of Structural Systems*. Orlando: Academic Press, 1986.

[62] WANG, M. Y.; WANG, X. PDE-Driven Level Sets, Shape Sensitivity and Curvature Flow for Structural Topology Optimization. *Computer Modeling in Engineering and Sciences*, v. 6, p. 373–395, 2004.

[63] WANG, X.; WANG, M. Y.; GUO, D. Structural shape and topology optimization in a level-set-based framework of region representation. *Structural and Multidisciplinary Optimization Multidisc Optimi*, v. 27, p. 1–19, 2004.

[64] GOURNAY, F. Velocity extension for the level-set method and multiple eigenvalues in shape optimization. *SIAM - Journal on Control and Optimization*, v. 45, n. 1, p. 343–367, 2006.

[65] TALISCHI, C. et al. Polygonal finite elements for topology optimization: A unifying paradigm. *Proceedings of the 2011 American Control Conference*, v. 82, p. 671–698, 2010.

[66] VAZ-JR, M.; MUÑOZ-ROJAS, P. A.; FILIPPINI, G. On the accuracy of nodal stress computation in plane elasticity using finite volumes and finite elements. *Computers and Structures*, Elsevier Ltd, v. 87, n. 17-18, p. 1044–1057, 2009.

[67] FILIPPINI, G.; MALISKA, C. R.; VAZ-JR., M. A physical perspective of the element-based finite volume method and FEM-Galerkin methods within the framework of the space of finite elements. *International Journal for Numerical Methods in Engineering*, v. 98, p. 24–43, 2014.

[68] TALISCHI, C. et al. PolyMesher: A general-purpose mesh generator for polygonal elements written in Matlab. *Structural and Multidisciplinary Optimization*, v. 45, n. 3, p. 309–328, 2012.

[69] LLOYD, S. Least squares quantization in PCM. *IEEE Transactions on Information Theory*, v. 28, n. 2, p. 129–137, 1982.

[70] WACHSPRESS, E. L. *A Rational Finite Element Basis*. New York, NY: Academic Press, 1975.

[71] SUKUMAR, N.; TABARRAEI, A. Conforming polygonal finite elements. *International Journal for Numerical Methods in Engineering*, v. 61, n. 12, p. 2045–2066, 2004.

[72] TALISCHI, C. et al. Polygonal finite elements for incompressible fluid flow. *International Journal for Numerical Methods in Fluids*, v. 74, p. 134–151, 2014.

[73] TALISCHI, C. et al. PolyTop: A Matlab implementation of a general topology optimization framework using unstructured polygonal finite element meshes. *Structural and Multidisciplinary Optimization*, v. 45, n. 3, p. 329–357, 2012.

[74] VASCONCELLOS, J. F. V.; MALISKA, C. R. a Finite-Volume Method Based on Voronoi Discretization for Fluid Flow Problems. *Numerical Heat Transfer B*, v. 45, n. 4, p. 319–342, 2004.

[75] GAIN, A. L.; PAULINO, G. H. Phase-field based topology optimization with polygonal elements: a finite volume approach for the evolution equation. *Structural and Multidisciplinary Optimization*, v. 46, n. 3, p. 327–342, apr 2012.

[76] GURTIN, M. E. Generalized Ginzburg-Landau and Cahn-Hilliard equations based on a microforce balance. *Physica D*, v. 92, p. 178–192, 1996.

APPENDIX A – AUGMENTED LAGRANGIAN METHOD

As discussed in [59], it is possible to convert an inequality constraint into an equality constraint by introducing a vector of additional variables $z = (z_1, ..., z_r)$. Thus, problem P_3 in (3.23) is given by

$$\min_{\phi,z} \quad m_\phi(\mathbf{u}) = \int_D \left[\rho(\phi) + \frac{\mu}{2}\mathbf{C}(\phi)\boldsymbol{\varepsilon}(\mathbf{u})\cdot\boldsymbol{\varepsilon}(\mathbf{u})\right] dD,$$

$$\text{subject to:} \left\{ \begin{array}{ll} a_\phi(\mathbf{u},\mathbf{v}) = l_\phi(\mathbf{v}), & \forall \mathbf{v} \in V, \\ g_j(\mathbf{u},\phi) + z_j^2 = 0, & j = 1, ..., r \end{array} \right. \tag{A.1}$$

We have that ϕ^* is a local (global) minimum of (3.23) if and only if $(\phi^*, z_1^*, ..., z_r^*)$, where $z_j^* = \sqrt{-g_j(\mathbf{u},\phi^*)}$, $j = 1, ..., r$, is a local (global) minimum of (A.1).

Consider the augmented Lagrangian for problem (A.1) defined for $c > 0$ by

$$\begin{aligned} \bar{J}(\phi,z) = &\int_D \left[\rho(\phi) + \frac{\mu}{2}\mathbf{C}(\phi)\boldsymbol{\varepsilon}(\mathbf{u})\cdot\boldsymbol{\varepsilon}(\mathbf{u})\right] dD \\ &+ \sum_{j=1}^{r} \left\{ \alpha_j \left[g_j(\mathbf{u},\phi) + z_j^2\right] + \frac{c}{2}\left[g_j(\mathbf{u},\phi) + z_j^2\right]^2 \right\}. \end{aligned} \tag{A.2}$$

We must minimize the augmented Lagrangian (A.2) with respect to (ϕ, z) for various values of α and c. An important point here is that minimization of $\bar{J}(\phi,z)$ with respect to z can be carried out explicitly for each fixed ϕ. To see this, note that

$$\begin{aligned} \min_z \quad \bar{J}(\phi,z) = &\int_D \left[\rho(\phi) + \frac{\mu}{2}\mathbf{C}(\phi)\boldsymbol{\varepsilon}(\mathbf{u})\cdot\boldsymbol{\varepsilon}(\mathbf{u})\right] dD \\ &+ \sum_{j=1}^{r} \min_{z_j} \left\{ \alpha_j \left[g_j(\mathbf{u},\phi) + z_j^2\right] + \frac{c}{2}\left[g_j(\mathbf{u},\phi) + z_j^2\right]^2 \right\}. \end{aligned} \tag{A.3}$$

The minimization with respect to z_j is equivalent to

$$\min_{\bar{z}_j \geq 0} \left\{ \alpha_j \left[g_j(\mathbf{u},\phi) + \bar{z}_j\right] + \frac{c}{2}\left[g_j(\mathbf{u},\phi) + \bar{z}_j\right]^2 \right\} \tag{A.4}$$

(Note that $\bar{z}_j := z_j^2$). The function in braces above is quadratic in $\bar{z}_j$. Its

unconstrained (global) minimum is the scalar $\hat{z}_j$ at which the derivative is zero. We have

$$\alpha_j + c\,[g_j(\mathbf{u},\phi) + \hat{z}_j] = 0$$

from which

$$\hat{z}_j = -\,[(\alpha_j/c) + g_j(\mathbf{u},\phi)]\,.$$

There are two possibilities. Either $\hat{z}_j \geq 0$ in which case $\hat{z}_j$ solves problem (A.4), or else the solution of problem (A.4) is $\bar{z}_j^* = 0$, that is,

$$\bar{z}_j^* = \begin{cases} -\,[(\alpha_j/c) + g_j(\mathbf{u},\phi)]\,, & \text{if } -\,[(\alpha_j/c) + g_j(\mathbf{u},\phi)] > 0 \\ 0, & \text{if } -\,[(\alpha_j/c) + g_j(\mathbf{u},\phi)] \leq 0 \end{cases}.$$

Thus the solution of problem (A.4) is

$$\bar{z}_j^* = \max\left\{0\ ;\ -\,[(\alpha_j/c) + g_j(\mathbf{u},\phi)]\right\}, \tag{A.5}$$

and we have

$$h_j(\mathbf{u},\phi) = g_j(\mathbf{u},\phi) + \bar{z}_j^* = g_j(\mathbf{u},\phi) + z_j^{*2} = \max\left\{g_j(\mathbf{u},\phi)\ ;\ -\frac{\alpha_j}{c}\right\} \tag{A.6}$$

Note that the variable z was eliminated from the problem.

By using (A.6) into (A.2), we are thus led to the following definition of the augmented Lagrangian:

$$\begin{aligned} J(\phi) = &\int_D \left[\rho(\phi) + \frac{\mu}{2}\mathbf{C}(\phi)\boldsymbol{\varepsilon}(\mathbf{u})\cdot\boldsymbol{\varepsilon}(\mathbf{u})\right]\, dD \\ &+ \sum_{j=1}^{r}\left\{\alpha_j h_j(\mathbf{u},\phi) + \frac{c}{2}\,[h_j(\mathbf{u},\phi)]^2\right\}. \end{aligned} \tag{A.7}$$

The conclusion from the preceding discussion is that the problem

$$\begin{array}{c} \min \quad \bar{J}(\phi,z) \\ \text{subject to: } (\phi,z) \in \mathbb{R}^{n+r} \end{array} \tag{A.8}$$

is equivalent to the problem

$$\begin{array}{c} \min \quad J(\phi) \\ \text{subject to: } \phi \in \mathbb{R}^{n} \end{array} \tag{A.9}$$

and $[\phi(\alpha,c),\ z(\alpha,c)]$ is a solution of problem (A.8) if and only if $\phi(\alpha,c)$ is

a solution of problem (A.9).

As a result, problem (A.1) can be converted to an equality-constrained problem and rewritten as

$$\begin{aligned} \min_{\phi} \quad J(\phi) = & \int_D \left[\rho(\phi) + \frac{\mu}{2} \mathbf{C}(\phi) \boldsymbol{\varepsilon}(\mathbf{u}) \cdot \boldsymbol{\varepsilon}(\mathbf{u}) \right] \, dD \\ & + \sum_{j=1}^{r} \left\{ \alpha_j h_j(\mathbf{u}, \phi) + \frac{c}{2} \left[h_j(\mathbf{u}, \phi) \right]^2 \right\}, \qquad \text{(A.10)} \\ \text{subject to:} \quad & a_\phi(\mathbf{u}, \mathbf{v}) = l_\phi(\mathbf{v}), \quad \forall \mathbf{v} \in V, \end{aligned}$$

where $h_j(\mathbf{u}, \phi)$ is given by

$$h_j(\mathbf{u}, \phi) = \max \left\{ g_j(\mathbf{u}, \phi) \; ; \; -\frac{\alpha_j}{c} \right\}. \qquad \text{(A.11)}$$

Note that the computation of (A.10) need not involve the additional variables $z_1, ..., z_r$ since we can solve in place of problem (A.8) the equivalent problem (A.9).

APPENDIX B – DERIVATIVE OF THE FAILURE FUNCTION

A material failure criterion consists of a function g capable of identifying how far a material point submitted to a quasi-static stress state is from failure. It is a usual approach to write the failure function of any isotropic material as

$$g(I_1, J_2, J_3, k_1, k_2, ...) = 0, \tag{B.1}$$

where k_1 and k_2 are material parameters, and I_1, J_2 and J_3 are the three invariants of the stress tensor $\boldsymbol{\sigma}(\mathbf{u})$ given by

$$I_1 = tr[\boldsymbol{\sigma}(\mathbf{u})] = \mathbf{I} \cdot \boldsymbol{\sigma}(\mathbf{u}), \tag{B.2}$$

$$J_2 = \frac{1}{2}\mathbf{s}(\mathbf{u}) \cdot \mathbf{s}(\mathbf{u}), \tag{B.3}$$

$$J_3 = \frac{1}{3}\mathbf{s}(\mathbf{u})\mathbf{s}(\mathbf{u}) \cdot \mathbf{s}(\mathbf{u}), \tag{B.4}$$

where

$$\mathbf{s}(\mathbf{u}) = \mathbf{P}\boldsymbol{\sigma}(\mathbf{u}), \quad \mathbf{P} = \mathbf{II} - \frac{1}{3}\mathbf{I} \otimes \mathbf{I} \tag{B.5}$$

is the tensor of deviatoric stresses.

The derivative of $h_r(\mathbf{u}, \phi)$ in the direction $\delta\mathbf{u}$ may be written as function of the invariants of the stress tensor $\boldsymbol{\sigma}_r$ through the chain rule:

$$\begin{aligned} \frac{\partial h_r(\mathbf{u}, \phi)}{\partial \mathbf{u}}[\delta\mathbf{u}] = & \frac{\partial h_r(\mathbf{u}, \phi)}{\partial I_1}\frac{\partial I_1}{\partial \mathbf{u}}[\delta\mathbf{u}] + \frac{\partial h_r(\mathbf{u}, \phi)}{\partial J_2}\frac{\partial J_2}{\partial \mathbf{u}}[\delta\mathbf{u}] \\ & + \frac{\partial h_r(\mathbf{u}, \phi)}{\partial J_3}\frac{\partial J_3}{\partial \mathbf{u}}[\delta\mathbf{u}]. \end{aligned} \tag{B.6}$$

Calculating the derivatives of the stress invariants in relation to $\mathbf{u}$,

$$\begin{aligned} \frac{\partial I_1}{\partial \mathbf{u}}[\delta\mathbf{u}] = & \left.\frac{\partial}{\partial t}[\mathbf{I} \cdot \boldsymbol{\sigma}_r(\mathbf{u} + t\delta\mathbf{u})]\right|_{t=0}, \\ & = \mathbf{I} \cdot \boldsymbol{\sigma}_r(\delta\mathbf{u}) = \mathbf{I} \cdot \mathbf{C}_r\boldsymbol{\varepsilon}_r(\delta\mathbf{u}), \\ & = \mathbf{C}_r\mathbf{I} \cdot \boldsymbol{\varepsilon}_r(\delta\mathbf{u}), \end{aligned} \tag{B.7}$$

$$\begin{aligned}\frac{\partial J_2}{\partial \mathbf{u}}[\delta\mathbf{u}] &= \frac{\partial}{\partial t}\left[\frac{1}{2}\mathbf{s}_r(\mathbf{u}+t\delta\mathbf{u})\cdot\mathbf{s}_r(\mathbf{u}+t\delta\mathbf{u})\right]\Bigg|_{t=0},\\ &= \mathbf{s}_r(\mathbf{u})\cdot\mathbf{P}\boldsymbol{\sigma}_r(\delta\mathbf{u}),\\ &= \mathbf{P}^T\mathbf{s}_r(\mathbf{u})\cdot\mathbf{C}_r\boldsymbol{\varepsilon}_r(\delta\mathbf{u}),\\ &= \mathbf{C}_r\mathbf{P}^T\mathbf{s}_r(\mathbf{u})\cdot\boldsymbol{\varepsilon}_r(\delta\mathbf{u}),\end{aligned} \tag{B.8}$$

$$\begin{aligned}\frac{\partial J_3}{\partial \mathbf{u}}[\delta\mathbf{u}] &= \frac{\partial}{\partial t}\left[\frac{1}{3}\mathbf{s}_r(\mathbf{u}+t\delta\mathbf{u})\mathbf{s}_r(\mathbf{u}+t\delta\mathbf{u})\cdot\mathbf{s}_r(\mathbf{u}+t\delta\mathbf{u})\right]\Bigg|_{t=0},\\ &= \mathbf{s}_r(\mathbf{u})\mathbf{s}_r(\mathbf{u})\cdot\mathbf{P}\mathbf{C}_r\boldsymbol{\varepsilon}_r(\delta\mathbf{u}),\\ &= \mathbf{C}_r\mathbf{P}^T\mathbf{s}_r(\mathbf{u})\mathbf{s}_r(\mathbf{u})\cdot\boldsymbol{\varepsilon}_r(\delta\mathbf{u}).\end{aligned} \tag{B.9}$$

Here, $\mathbf{s}_r(\mathbf{u})$ is the deviatoric stress tensor of sample point r. Substituting Equation (B.7)-(B.9) in (B.6),

$$\frac{\partial h_r(\mathbf{u},\phi)}{\partial \mathbf{u}}[\delta\mathbf{u}] = \mathbf{C}_r\mathbf{A}_r(\mathbf{u},\phi)\cdot\boldsymbol{\varepsilon}_r(\delta\mathbf{u}), \tag{B.10}$$

where

$$\mathbf{A}_r(\mathbf{u},\phi) = \frac{\partial h_r(\mathbf{u},\phi)}{\partial I_1}\mathbf{I} + \frac{\partial h_r(\mathbf{u},\phi)}{\partial J_2}\mathbf{P}^T\mathbf{s}_r(\mathbf{u}) + \frac{\partial h_r(\mathbf{u},\phi)}{\partial J_3}\mathbf{P}^T\mathbf{s}_r(\mathbf{u})\mathbf{s}_r(\mathbf{u}), \tag{B.11}$$

is a tensor containing the derivatives from the failure funtion in relation to the stress invariants.

As $h_r(\mathbf{u},\phi) = \max\left\{g_r(\mathbf{u},\phi); -\frac{\alpha_r}{c}\right\}$ where $g_r(\mathbf{u},\phi)$ is given by Equation (3.21), then if $h_r(\mathbf{u},\phi) = g_r(\mathbf{u},\phi)$

$$\begin{aligned}\frac{\partial g_r(\mathbf{u},\phi)}{\partial I_1} &= \frac{\partial g_r(\mathbf{u},\phi)}{\partial J_3} = 0,\\ \frac{\partial g_r(\mathbf{u},\phi)}{\partial J_2} &= \frac{3}{2\sigma_{adm}\sigma_r^{vM}}\Psi(H_r(\phi)),\end{aligned}$$

and the tensor $\mathbf{A}_r(\mathbf{u},\phi)$ is given by

$$\mathbf{A}_r(\mathbf{u},\phi) = \frac{3}{2\sigma_{adm}\sigma_r^{vM}}\Psi(H_r(\phi))\mathbf{P}^T\mathbf{s}_r(\mathbf{u}).$$

In the case that $h_r(\mathbf{u},\phi) = -\dfrac{\alpha_r}{c}$, then

$$\frac{\partial h_r(\mathbf{u},\phi)}{\partial I_1} = \frac{\partial h_r(\mathbf{u},\phi)}{\partial J_2} = \frac{\partial h_r(\mathbf{u},\phi)}{\partial J_3} = 0,$$

and the tensor $\mathbf{A}_r(\mathbf{u},\phi)$ is zero.

APPENDIX C – DERIVATIVE OF THE REGULARIZED OBJECTIVE FUNCTION

Let $\delta\phi$ be a direction of the admissible variations of ϕ. The derivative of $J_R(\phi)$ (expression 5.1) in the direction $\delta\phi$ can be written as

$$\frac{dJ_R(\phi)}{d\phi}[\delta\phi] = \frac{dJ(\phi)}{d\phi}[\delta\phi] + \frac{d}{d\phi}\left(\int_D \frac{1}{2}\tau\,|\nabla\phi|^2\,dD\right)[\delta\phi]. \tag{C.1}$$

The derivative $dJ(\phi)/d\phi\ [\delta\phi]$ is calculated in Section 3.7 and it is given by Eq. (3.40). Since $|\nabla\phi|^2 = \nabla\phi\cdot\nabla\phi$, the derivative of the regularization term can be rewritten as

$$\frac{d}{d\phi}\left(\int_D \frac{1}{2}\tau\,|\nabla\phi|^2\,dD\right)[\delta\phi] = \int_D \tau\nabla\phi\cdot\nabla\left(\delta\phi\right)dD. \tag{C.2}$$

Using the equality

$$\nabla\phi\cdot\nabla\left(\delta\phi\right) = \mathrm{div}(\nabla\phi\ \delta\phi) - \nabla^2\phi\ \delta\phi, \tag{C.3}$$

and Divergence Theorem, it follows that

$$\frac{d}{d\phi}\left(\int_D \frac{1}{2}\tau\,|\nabla\phi|^2\,dD\right)[\delta\phi] =$$
$$\int_{\partial D\backslash\partial D_N} \tau\delta\phi\ \nabla\phi\cdot\mathbf{n}d\partial D + \int_{\partial D_N} \tau\delta\phi\ \nabla\phi\cdot\mathbf{n}d\partial D - \int_D \tau\nabla^2\phi\ \delta\phi dD. \tag{C.4}$$

Assuming the boundary conditions

$$\begin{cases} \nabla\phi\cdot\mathbf{n} = \dfrac{\partial\phi}{\partial\mathbf{n}} = 0 & \text{on } \partial D\backslash\partial D_N\ , \\ \delta\phi = 0 & \text{on } \partial D_N\ , \end{cases} \tag{C.5}$$

Eq. (C.4) can be simply written as

$$\frac{d}{d\phi}\left(\int_D \frac{1}{2}\tau\,|\nabla\phi|^2\,dD\right)[\delta\phi] = -\int_D \tau\nabla^2\phi\ \delta\phi dD. \tag{C.6}$$

Substituting (3.40) and (C.6) into (C.1), the formal variation is given by

$$\frac{dJ_R(\phi)}{d\phi}[\delta\phi] = \int_D \left(V(\phi)\delta(\phi) - \tau\nabla^2\phi\right)\delta\phi \; dD, \tag{C.7}$$

and yields the expression

$$\frac{dJ_R(\phi)}{d\phi} = V(\phi)\delta(\phi) - \tau\nabla^2\phi = \frac{dJ(\phi)}{d\phi} - \tau\nabla^2\phi, \tag{C.8}$$

for the variational derivative (the coefficient of $\delta\phi$) (see, for example, [76]).

APPENDIX D – WACHSPRESS SHAPE FUNCTION GRADIENT

Based on Fig. 6.1, the area of the triangles formed by $\boldsymbol{\xi}$ and the vertices as well as their gradient with respect to it are computed using expressions:

$$A_i(\boldsymbol{\xi}) = \frac{1}{2}\begin{vmatrix} \xi_1 & \xi_2 & 1 \\ p_{1,i-1} & p_{2,i-1} & 1 \\ p_{1,i} & p_{2,i} & 1 \end{vmatrix},$$

$$\frac{\partial A_i}{\partial \xi_1} = \frac{1}{2}\left(p_{2,i-1} - p_{2,i}\right), \quad \frac{\partial A_i}{\partial \xi_2} = \frac{1}{2}\left(p_{1,i} - p_{1,i-1}\right)$$

The derivatives of the interpolant are simply given by

$$\frac{\partial w_i}{\partial \xi_m} = -w_i\left(\frac{1}{A_i}\frac{\partial A_i}{\partial \xi_m} + \frac{1}{A_{i+1}}\frac{\partial A_{i+1}}{\partial \xi_m}\right), \quad m = 1,2$$

and from (6.1) we have the following expression for the shape function gradients:

$$\frac{\partial N_i}{\partial \xi_m} = \frac{1}{\sum_{j=1}^{n} w_j}\left(\frac{\partial w_i}{\partial \xi_m} - N_i \sum_{j=1}^{n} \frac{\partial w_j}{\partial \xi_m}\right), \quad m = 1,2$$

For more information see [73].